Imperial College London
Department of Physics
Photonics Group

Laser scanning confocal microscope with direct wavefront sensing of volumetric backscattered light

By
Noemi Patricia Correa Poblete

This thesis is submitted in partial fulfilment of the requirements
for the degree of *Doctor of Philosophy* (Ph.D)
Imperial College of Science, Technology and Medicine

May, 2016.

Abstract

Fluorescent labelling combined with confocal microscopy is a powerful tool employed in several laboratories around the world. This is based in the ability to image well only detail that arises from the region of the specimen close to the focal plane. In confocal microscopes, a pinhole situated in front of the detector leads to optical sectioning, at the cost of rejecting some signal photons together with the out-of-focus ones. The problem in this case is that photons generated in the focal volume are susceptible to scattering, changing their direction and not passing through the pinhole, thus losing information. Natural specimen composition, such as structures sizes and their refractive indices will degrade the intensity and the shape of the focus, but they also affect the imaging of the generated fluorescence onto the pinhole. This loss becomes more significant when we want to image deeper in the specimen.

In this work a laser scanning confocal microscope with direct wavefront sensing of volumetric backscattered light was developed and built. It is shown for a couple of specimens, that the signal levels can be improved by correcting in real time the aberrations introduced by these samples at different depths. The advantage of this method relies on the fact that wavefront distortions are sensed by backscattered light instead of fluorescent light from the sample. Problems such as photo-bleaching and photo-toxicity in the specimen can be minimized with this approach.

The problem associated with centroid estimation position when out-of-focus light forms part of the light gathered by the sensor was addressed. A centroid algorithm capable of rejecting this signal in order to get an accurate and meaningful centroid detection is proposed. The hybrid centroid algorithm that we propose is based on the optimisation of the product between the data and a spot model, was compared with one of the traditional methods employed with Shack-Hartmann sensors. Computer generated and also experimental data obtained from the system that we built was employed to test the centroid algorithm. Good centroid estimation values were obtained in both cases.

Additionally, to improve the system, the implementation of an optimal reconstructor is approached. The problem associated with the lack of prior knowledge for biological and non-biological samples to be used for wavefront reconstruction is addressed. This was done by generating different wavefront statistics as input wavefronts, and reconstructing these by using the same or different priors, at different signal-to-noise ratios. From the results, it was possible to find a range of values where the wavefront reconstruction error was small and gave reasonable error values along the whole range of possible input wavefront.

Finally, successful wavefront corrections using samples made of leaves in agarose, leaves in agarose with glucose and cell spheroids were obtained at different depths. Even though improvements in image resolution were negligible, we did obtain an increase in the intensity of the confocal images that we recorded. Also, smaller values for the wavefront Zernike coefficients and root-mean-square were obtained, demonstrating that the system is able to perform wavefront corrections using just backscattered light.

Author Declaration

All the work presented within this thesis is my own with the exception of the following:

- Home-written Python/Cython software.
- Icy: a software that provides resources to visualize, annotate and quantify bioimaging data. It has been created by the Quantitative Image Analysis Unit at Institut Pasteur (http://www.bioimageanalysis.org/). Icy is free and open source.

Copyright Declaration

The copyright of this thesis rests with the author and is made available under a Creative Commons Attribution Non-Commercial No Derivative licence. Researchers are free to copy, distribute or transmit the thesis on the condition that they attribute it, that they do not use it for commercial purpose and that they do not alter, transform or build upon it. For any reuse or redistribution, researchers must clear to others the licence terms of this work.

Acknowledgments

I will like to thank to Dr. Carl Paterson, for allowing me to embark on this new adventure at the other side of the world, four years ago. Carl, thank you for all your advices, for every single cup of coffee that we shared every Friday to discuss about work, sport, food, English grammar, humour and culture. Thank you for allowing me to know you not just as a supervisor but also as a friend. Thank you for supported me in the difficult times that I encountered during the last four years, that sadly were more than a couple.

I will like to start on this hemisphere... So, from the north, thanks to all the people that I have met randomly in Blackett: Dr Mark Neil, Dr Paul French and Dr Chris Dunsby. To Alice, Malcolm, Meilin, Brian, Loli and Andrew. To the people in the Photonics Group. Sanja, Marcia and Judith, I really had a great time with all of you, thanks for all the good memories that you created with me. To Simon, somehow we are going to collect some money so you can have a great holidays all included far away from Martin. To my dear Martin, thank you for fighting with me all the time and teach me about UK candies (flying saucers, fudge of different flavours, sugar mice and obviously... pe, pe, pe, pe... penguins). I will never forget the Monty python videos, especially when you and Carl were almost crying with "two ronnies, four candles" sketch. Thank you for all the wonderful work that all of you do everyday.

To all the friends that I have been collecting along these years, in these super sunny island. To Nick , Teng, Andy, Ian , David, Jack, Moritz, Emilio, Hugh , Hugo , Elizabeth, Vincent, Javier, Marion, Ian Munro and many more. Thank you so much for the friendship and extra professional advice to Edwin, Stina, Kwasi and sunilcito. Guys... Thank you for the awesome weight lifting gym seasons. Dear Sunil, one day you will conquer the world and exterminate all the evil rats with fluffy tails!

Thanks to all the wonderful people that I met thanks to my lovely hubby. To Federico, Roberto, Kieran, Silvia, Hywel, Neal, Nanda, Andres and Dr Phil Lucas. Thank you for being so nice to Carlos when he was alone, for playing football with him, drinking beers and talk about silly things. I will never forget those epic parties at Horsa Garden. Thanks to the University of Hertfordshire for the internet while I was at work with Carlos. To my girls and my dear Helena.

Now flying south... I want to thanks to all the people that for so many years taught me

about physics, hard work and passion. To all the people at Pontificia Universidad Catolica de Chile, Mario Favre, Edmund Wyndham, Marcelo Loewe, Rafael Benguria, Ulrich Volkmann, Alejandro Cabrera. To my dear university friends: Felipe, Julito, Alvin, Tati, Fefi, Joyce, Dani, Pilu, Favi, Carlanga, Sr. godito, Alicia y Jacuna. No crean que me olvide de ustedes: Mi queridisimo don don dirk, daaaavid!, Sra Cecilia, Sra Liliana, Jose y el Sr. Vargas. To my life friends, mi coquita, mi mapuche y el kotetin! The biggest hug across the ocean to all of you!

To my family, the acquired one (Contreras-Peña), thank you for the support during all the years and for having the most wonderful son that makes my days brighter, exciting and different. To the original family (Poblete-Morizot and Correa-Poblete). Gracias por estos años de apoyo mientras yo estudiaba, gracias por ayudarme a levantarme cada vez que me cai en el camino. Gracias papá y mamá por apoyarme siempre y dejarme haber sido lo que quise ser. A mi brocito, cada dia te quiero más hermano del alma, lo mismo a la Patricia y al Tata (Grandpa, soon to be Great grandpa!) y mis Tios. Se que la distancia es buena, ayuda a extrañar a la gente y volvernos más unidos. Siempre los tengo y he tenido en mi corazón.

To the love of my life, my hubby, my partner of adventures!. Thank you Carlos for all these years, with you, life is better everyday. We might be just two poor kids, with lot of dreams and new exciting things to come, but nothing matters if we are together. Can you see? Here we are again, ending another adventure at the other side of the world and we already started a new one! and this one, is bigger and better, much much better. Tamito mi Charly.

Some words for the missing, the love that remains. This work is also dedicated to my dear friend Luis Hermosilla (Luis! vamos por la tercera). To my Grandma Clara, we miss you a lot. To my former supervisor, friend and scientific father: Dr Hernán Chuaqui K. and to my weli, mi abuela. Weli, me hubiese encantado ver tu carita al saber que estoy terminando esto que ha costado harto y me ha traido tan lejos, ahora aún mas lejos de ti. Pero más feliz te haria saber que vas a ser bisabuela! y con el Carlos estamos muy felices por nuesto piri. No sabes cuanto te extraño y cuanta falta me haces. Te quiero. I miss you and you are missing all the time.

Finally, I want to thanks to Becas Chile for the grant that allowed me to do this PhD.

Every time I see it clearly
It's a time that you are near me
I just don't see the world without you
Where ever I go
You're along
Sometimes not actually, but in my mind
We cheers another day ...

... to Carlos and our bundle of joy.

Contents

1 Introduction **1**

1.1 Motivation 1

1.2 Laser Scanning Confocal Microscopy 10

1.2.1 Historical perspective 10

1.2.2 Principles of Confocal Microscopy 12

1.3 Shack-Hartmann wavefront sensor 15

1.3.1 Principle of operation 15

2 Wavefront sensing **20**

2.1 The principle of centroid estimation 21

2.1.1 Type of centroid algorithms 22

2.2 Quadratic program for centroid estimation 26

2.3 Conclusions 44

3 Wavefront reconstruction **45**

3.1 The principle of wavefront reconstruction 45

3.2 Optimal reconstructor and Prior knowledge 50

3.3 Prior knowledge testing 59

3.4 Conclusions 71

4 Adaptive Optics system using backscattered light **73**

4.1 Experimental setup 73

4.2 Principle of wavefront correction 77

4.3 Correction of Red-edged Dracaena and agarose samples 78

4.4 Correction of cell spheroid samples 88

5 Summary **95**

6 Conclusions **99**

A Appendix: Pinhole size diameter for wavefront sensing **110**

List of Figures

1.1 Confocal and multi-photon sample illumination. In confocal microscopes, fluorescent signal (emission) will be generated at the focal plane and also from planes above and below it. Thus, to provide optical sectioning, an aperture must be located in front of the detector. In multi-photon microscopes, fluorescent light is only generated at the focal spot and out-of-focus photons are rarely generated, which provides optical sectioning without a pinhole. 2

1.2 Simple schematic diagram of the optical pathways and basic components in a widefield and a confocal microscope, the main difference corresponds to the use of a confocal pinhole. **(A) Wide-field microscope:** the light source employed is generally a Mercury lamp (Hg lamp). Fluorescent emitted by the specimen occurs through the whole excited volume and obscure resolution of features that lie in the focal plane. **(B) Confocal microscope:** A point light source is employed and generally obtained from the output of a laser coupled to an optical fibre or a laser passing through a pinhole aperture that is located in a conjugate plane with the focal point in the specimen. A confocal pinhole removes unwanted light coming from planes located above and below the focal plane. 12

1.3 Shack-Hartmann wavefront sensor spot positions based on the nature of the incoming wavefront. (A) Plane wavefront: the spot are located at the centre of each sub-aperture. (B) aberrated wavefront: the spot are displaced from the centre. 16

1.4 Spot displacement determination $d_{x,y}$, considering a single lenslet from the array. 18

2.1 Gaussian spot formed by the flat wavefront reference (blue dashed line) and the data (with amplitude A_d and width σ_d, shown in green) in a search block of a size n pixels. The displacement between the two spots is given by $\delta_x = x_r - x_d$. 28

2.2 Plots to understand how the gradient (Jacobian) and Hessian are involved in the determination of the next value in our iterative process. The objective is to find $p*$ that maximizes the cost function $I(p)$. Basically this can be done moving upwards the function surface until no more additional increments are needed (A). Plots (B) and (C) are related to the Hessian or direction to follow in the next iteration. Plots (D) and (E) are related to the gradient or size of the step in the next iteration. Small steps are required in order to converge to an optimum value without overshooting, on the other hand, big values are required to achieve convergence in short time, particularly when the initial values are not too close to the optimum value. 31

2.3 Following a Gaussian model $f(x, y, \sigma)$, masks are generated for the first and second derivatives of x, y and σ. 32

2.4 Graphical representation of how the centroid algorithm that we present is carried out. Using a data image, the CoG centroid coordinates are obtained and from this, we generate a Gaussian masks using $(x_{\mathrm{CoG}}, y_{\mathrm{CoG}})$ as initial parameters. The whole process will stop once the optimal value has been achieved. 33

2.5 Results obtained when one spot with a known coordinate position was modelled under different SNR. Centroid 1 ("$\star$") represents the simple centroid algorithm (CoG) and centroid 2 ("$\times$") is the algorithm that we proposed. The original coordinate values are represented by "+". Important to notice that at low SNR, the values obtained with our method are closer to the original values compared with those obtained using the CoG method. 35

2.6 Results obtained when 30 realisations for a spot with known coordinates position were modelled under a SNR = 10. In both cases, the values obtained using the method that we proposed are closer to the original values. Gaussian and original coordinates values are almost overlapped along the 30 iterations compared with the traditional centre of gravity method, where an offset or bias can be observed. **Left-hand side:** X coordinates. **Right-hand side:** Y coordinates. 36

2.7 Spot position (x, y) obtained using the CoG and the proposed hybrid method for cases of low SNR values. Original spot position is represented by the dashed black line. A considerable amount of bias can be observed in the centroid values obtained with the CoG method. 39
2.8 Different spots with different SNR values. Over each spot, the CoG (centroid 1) coordinate values and the Gaussian values were calculated. The Gaussian process was repeated 8 times in order to test the method convergence. The initial guess used to generate the Gaussian masks were the coordinates obtained with the CoG. After the first iteration, the values calculated by the Gaussian method were employed to generate the subsequent masks. 40
2.9 Spot coordinate values versus the number of iteration carried out are presented for a SNR approximated of 4. 41
2.10 Results obtained when real data obtained with the SHWFS. Spot coordinates obtained using the CoG method and the Gaussian method are plotted. . . . 42
2.11 Graphical representation of how the centroid algorithm that we present is carried out when using images obtained from the SHWFS. The masks to be employed are generated only one time, with initial values $(0.0, 0.0, \sigma)$ and are applied to every single spot. 43

3.1 Three different slope measurement sampling geometries and phase points employed in zonal reconstruction. **Left-hand side:** configuration presented by Fried. **Centre:** configuration presented by Hudgin. Right-hand side: configuration presented by Southwell. 47
3.2 Covariance matrices of Zernike modes generated using different values for the Wiener spectrum. Each one represents different normalized wavefront statistics that will be employed to test the reconstruction performance. The first matrix, however, corresponds to the particular case where no prior is considered. In this case, all the Zernike coeficients are equally weighted. . . . 61
3.3 Error values obtained when reconstructing the wavefront with various Wiener spectrum exponents α_0, using a non-informative prior statistics ($\alpha_{\mathrm{R}} = \mathbb{I}$), at different SNR. 62

3.4 Error values obtained when an input wavefront with fix statistics is reconstructed with a matching informative prior $\alpha_R = \alpha_0$ and using a non-informative prior $\alpha_R = \mathbb{\nVdash}$ for different SNR. **Top:** α_0=1.67, **Bottom:** α_0=2.33. In both panels the inset shows the normalised difference obtained for the MSE considering $\alpha_R = \alpha_0$ and $\alpha_R = \mathbb{I}$. The difference between MSE is bigger at lower values for SNR ($\leq$ 20), while for high SNR, whether we use a prior or not does not make a big difference, as MSE reaches zero. 63

3.5 Error values obtained when an input wavefront with fix statistics is reconstructed with a matching informative prior $\alpha_R = \alpha_0$ and using a non-informative prior $\alpha_R = \mathbb{\nVdash}$ for different SNR. **Top:** α_0=3.0, **Bottom:** α_0=3.67. In both panels the inset shows the normalised difference obtained for the MSE considering $\alpha_R = \alpha_0$ and $\alpha_R = \mathbb{I}$. The difference between MSE is bigger at lower values for SNR ($\leq$ 20), while for high SNR, whether we use a prior or not does not make a big difference, as MSE reaches zero. 64

3.6 Error values obtained when reconstructing wavefronts with various Wiener spectrum exponents α_0 using different prior statistics (α_{R}). **Top:** SNR=1, **Bottom:** SNR=10. 66

3.7 Different values of α_{R} were used to reconstruct different input wavefronts. From here a better understanding of the possible values that need to be avoided to build the reconstructor can be inferred. **Top:** SNR=1, **Bottom:** SNR=10. 68

3.8 MSE values when different input wavefronts are reconstructed using α_{R} = 2.33 and 3.0, for different SNR values. **Top:** α_{R}=2.33, **Bottom:** α_{R}=3.0. . . 69

3.9 MSE values when different input wavefronts are reconstructed using α_{R} = 3.67, for different SNR values. 70

4.1 Experimental setup. All of the lenses are achromatic doublets, Linos: f_1=50 mm, f_2=100 mm, f_3=200 mm, f_4=60 mm, f_5=50 mm, f_6=50 mm, f_7=140 mm, f_8=300 mm, f_9=140 mm, f_{10}=100 mm, f_{11}=80 mm, PH1=50 μm, PH2 = 150 μm, RM: reference mirror, DIA: diaphragm, CBS: cube beam splitter, PCBS: polariser cube beam splitter, P:polariser, DM: deformable mirror, SMX-SMY: scanning mirror X-Y,M2-M3: mirrors, PBS: plate beam splitter 74

4.2 Sample made of agarose at 3% and a piece of leaf. **Top image:** confocal images without and with correction. The focal plane was at a depth of 206±0.5 μm. Light was reflected from chlorophyll cells that are found on the leaf surface. **Middle image:** image of reconstructed wavefronts surface (removed piston, tip, tilt and defocus terms). middle left-hand side: wavefront surface without correction. middle right-hand side: when the aberrations were corrected. **Bottom image:** Estimated Zernike coefficients amplitudes with and without correction, from term fifth up to 7^{th} order. 80
4.3 Shack-Hartmann spots when a sample of agarose 3% and a piece of Red-edged Dracaena was employed. The focal plane was situated 206±0.5 μm deep into the sample. When the system was correcting aberration, the intensity of the spots was higher for the corrected wavefront compared with the aberrated one. The distribution of the spots are similar, and only changes in the intensity of the spots are observed. 83
4.4 Values obtained for wavefront root-mean square, visibility and total image intensity when confocal images were obtained at four different focal planes in samples made of 3% agarose and a piece of leaf. 84
4.5 Three dimensional images for samples made of agarose at 3% and Red-edged Dracaena leaf. These images were generated using the software Icy. 85
4.6 Brightfield image of a sample made of agarose at 1% mixed with glucose at 4% (3:1) 86
4.7 Sample made of agarose at 1% mixed with glucose at 4% (3:1). **Top image:** confocal images without and with correction. The focal plane was at a depth of 63±0.5 μm. Light was reflected by the cellular wall, which main component is cellulose. **Middle image:** image of reconstructed wavefront surfaces (removed piston, tip, tilt and defocus terms),left-hand side: without correction and on right-hand side when the aberrations were corrected. **Bottom image:** Estimated Zernike coefficients amplitudes with and without correction for high-order modes. 87
4.8 Shack-Hartmann sensor images obtained when a sample of agarose 1%, glucose 4% (3:1) and Red-edged Dracaena was employed. The distribution of the spots are similar, however, the maximum spot intensity is bigger when aberrations were corrected. 88

4.9 Values obtained for wavefront root-mean square, visibility and total image intensity when confocal images were obtained at four different focal planes in samples made of 1% agarose, 4% glucose (3:1) and a piece of leaf 89
4.10 Three dimensional images for a sample made of agarose at 1%, glucose 4% (3:1) and Red-edged Dracaena leaf. 90
4.11 Brightfield images: (A) image of the whole spheroid. (B) Zoom to the area where we selected a region of interest to be imaged. 91
4.12 Spheroids made of human embrionic kidney cells. **Top image:** confocal images without and with correction. The focal plane was at a depth of 15±0.5 μm. **Middle image:** image of reconstructed wavefront surface (removed piston, tip, tilt and defocus terms), at right hand side when the aberrations were corrected. **Bottom image:** Estimated Zernike coefficients amplitudes with and without correction, from term fifth up to 7^{th} order. 92

List of Tables

1.1 Effective refractive index values for various tissues. The refractive indices of tissues and organs are unique. Organs and tissues like lung or bladder have refractive indices ranging from 1.33-1.35. Other organs like liver, kidney or clotted blood have refractive index around 1.4. Organs where fat is a predominant component have a refractive index bigger than 1.46. 4

1.2 Refractive indices of common mounting media. 6

1.3 Refractive indices of common immersion media. 6

2.1 100 realisations at different SNR. $\Delta\%$ corresponds to the difference in percentage between the original value and the value obtained with the CoG or the Gaussian method. The difference between values is smaller for the Gaussian method compared to the CoG, where a difference up to $\sim$9.8% can be achieved at low SNR. As the SNR starts to decrease, the values obtained for the X-Y coordinates start to increase when the CoG method is employed. . . 37

2.2 500 realisations at different SNR. $\Delta\%$ corresponds to the difference in percentage between the original value and the value obtained with the CoG or the Gaussian method. The difference between values is smaller for the Gaussian method compared to the CoG, especially at high SNR. A big difference, up to a $\sim$9.6% can be achieved at low SNR, when the coordinates are obtained using the CoG method. 38

3.1 Expressions that relate the slope measurements s_{ij}^{x} and s_{ij}^{y} for a subperture (i, j) of side d with the phase points for: Fried, Hudgin and Southwell grid patterns. 48

4.1 Values obtained for wavefront root-mean square, visibility and total image intensity when confocal images were recorded with and without corrections at a depth of 206±0.5 μm,for samples made of agarose at 3% and Red-edged Dracaena leaf. 82
4.2 Values obtained for wavefront root-mean square, visibility and total image intensity when confocal images were obtained with and without corrections at a depth of 63±0.5 μm, for a sample made of agarose at 1%, glucose 4% (3:1) and Red-edged Dracaena leaf. 83
4.3 Values obtained for wavefront root-mean square, visibility and total image intensity when confocal images were obtained with and without corrections at a depth of 15±0.5 μm, for the HEKS spheroid. 93

Chapter 1

Introduction

1.1 Motivation

Adaptive Optics is a method that has been widely used in astronomy to correct aberrations caused by the Earth's dynamic atmosphere (Tyson (2010)). Based on its great potential, it has been used more recently for many other optical scenarios, such as aberration compensation in high energy lasers (Bueno et al. (2009)), turbulence compensation for free-space laser communications (Li et al. (2016)), high resolution retinal imaging (Lombardo et al. (2013); Artal et al. (1995)) and microscopy. Significant effort has been carried out in the past ten years in optical microscopy to deal with aberrations arising from sources such as planar refractive index mismatch and specimen structures (Booth (2007a)).

Biological specimens with refractive index variations often degrade the resolution, signal strength and contrast of optical microscopes, in particular for widefield, confocal and multi-photon microscopy. The principal characteristic of a confocal microscope is its ability to image only features in a region of the specimen close to the focal plane. This characteristic is known as optical sectioning or depth discrimination.

In a confocal imaging system a single point of excitation light (or sometimes a group of points or a slit) is scanned across the specimen. The point is a diffraction limited spot on the specimen and is produced either by imaging an illuminated aperture situated in a conjugate focal plane to the specimen or, more usually, by focusing a collimated laser beam. With only a single point illuminated, the illumination intensity rapidly falls off above and below the plane of focus as the beam converges and diverges. However, due to the cone of illuminating

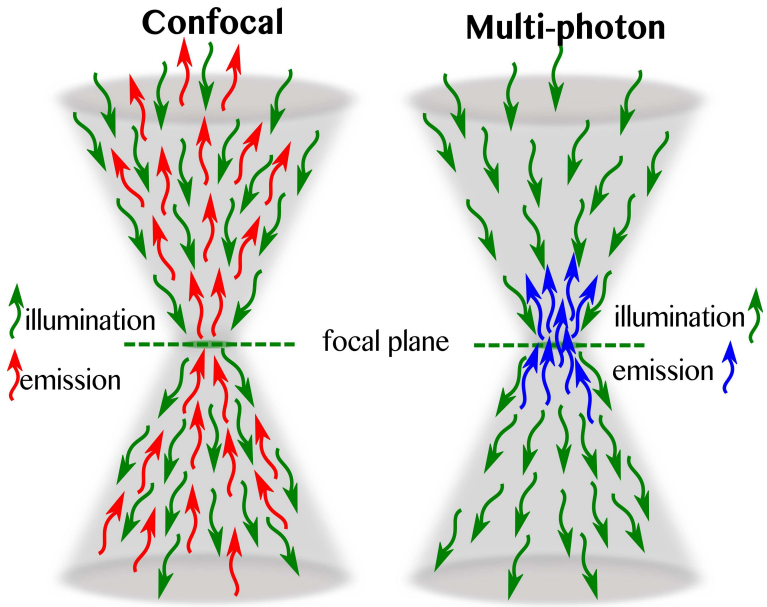


Figure 1.1: Confocal and multi-photon sample illumination. In confocal microscopes, fluorescent signal (emission) will be generated at the focal plane and also from planes above and below it. Thus, to provide optical sectioning, an aperture must be located in front of the detector. In multi-photon microscopes, fluorescent light is only generated at the focal spot and out-of-focus photons are rarely generated, which provides optical sectioning without a pinhole.

light and detected light, excitation of fluorescence situated out of the focal plane (above and below) will also be produced (Figure 1.1, left-hand side).

To achieve out-of-focus light rejection, a pinhole situated in front of the detector leads to optical sectioning at the cost of rejecting some signal photons (excited fluorescent light) coming from the focal plane together with the out-of-focus ones (Pawley (2006); Ustione & Piston (2011); Wilson (2011b,a)). The problem in this case is that photons or fluorescent signal generated in the focal volume are susceptible to scattering, changing their direction and not passing through the pinhole, reducing the detected signal. This becomes more significant when planes deeper inside the sample are imaged. In multi-photon microscopes, optical sectioning is achieved because the fluorescent signal is generated only at the focal spot, therefore does not require a pinhole on the detector (Figure 1.1, right-hand side). However, both types of microscopes are affected by aberrations in different ways. In confocal microscopes, aberrations degrade the intensity and the shape of the focus, but they also affect the amount of generated photons that will be detected for imaging purposes. For multi-photon, only aberrations in the illumination path are relevant, because the image resolution is determined in this case only by the focal spot.

Aberrations that affect an optical system can be mainly divided into two categories: those that do not affect the image or that cause only a displacement of the image and those that strongly affect the image quality. It is the latter kind of aberrations that are more important, and in microscopy these can mainly be divided into two categories: planar-refractive index mismatch and sample induced aberrations.

Planar refractive index mismatch corresponds to the most studied source of aberrations. As light is focused through a planar interface between two media with different refractive indices, aberrations are introduced by mismatches between the immersion medium, the cover glass and the specimen (Booth et al. (1998); Booth & Wilson (2000); Egner & Hell (1999)). Generally these type of aberrations are introduced by the use of a coverglass of incorrect thickness or a mismatch between the sample embedding medium and the objective immersion medium. When images are obtained using a confocal or a multi-photon microscope and these aberrations are present, the images obtained are dimmer and suffer from lateral and axial resolution degradation. The most crucial image degradation process is related to the axial resolution as it reduces the ability of the system to image deeper into the sample, decreasing the sample imaging depth. The primary aberration introduced is spherical aberration, which

R. I. of Different Tissue and Organs	
Organ/tissue	**R.I**
Spleen	1.443±0.002
Liver	1.448±0.002
Kidney Cortex	1.444±0.002
Medulla	1.438±0.002
Pancreas	1.435±0.002
Intestinal wall	1.436±0.002
Fat	1.472±0.002
Bone	1.556±0.002
Cartilage	1.492±0.002
Muscle	1.431±0.002
Lung	1.342±0.002
Bladder wall	1.350±0.002
Uncoagulated Blood (serum)	1.33± 0.002
Coagulated Blood	1.465±0.003
Grey matter	1.395±0.002
White matter	1.467±0.002
Cerebellum	1.470±0.002

Table 1.1: Effective refractive index values for various tissues. The refractive indices of tissues and organs are unique. Organs and tissues like lung or bladder have refractive indices ranging from 1.33-1.35. Other organs like liver, kidney or clotted blood have refractive index around 1.4. Organs where fat is a predominant component have a refractive index bigger than 1.46.

can be compensated by introducing a finite amount of spherical aberration in the opposite direction by means of changing the length of the objective (often via an adjustable collar) or employing adaptive optics.

Different investigations have already been performed on this topic, including both research about the limitations of altering the effective length at which the objective is operated (Sheppard & Gu (1991)) and into a quantitative quality criterion to set the correction collar on an objective (Schwertner et al. (2004)). To find the optimal setting for a collar, cover glasses of different thickness were employed, varying the interface microscope-slide-medium. This was done because objective lenses are designed for a particular coverglass thickness and any deviation from the nominal cover glass thickness value or refractive index will introduce spherical aberration. Dynamic correction of these aberrations had been achieved with adaptive optics, restoring diffraction-limited resolution (Kam et al. (2006); Neil et al. (2000)). A new approach has been proposed and tested in regular objectives, where spherical aberrations was corrected by means of a transmissive liquid crystal element (Tanabe et al. (2015)), obtaining good results.

Tissues behave similarly to any other bulk material in which the light propagation is subject to absorption, scattering, refraction and reflection. In heterogeneous materials, such as biological samples, there is not a unique value for the refractive index (n) and the effective refractive index is employed. It represents the average value of the refractive indices of its constituents (table 1.1, (Biwas & Gupta (2002))). As the refractive index determines the speed of light in the tissue, then, any change on its value introduces variations in refraction, reflection and scattering. The main constituent of any tissue is water with refractive index n=1.33 and this can be employed as the minimum sensitive value to characterise a sample. However, as presented in table 1.1, even when the effective refractive index is employed, various tissue components will have an index value larger than water. If we now consider basic tissue constituents, some possible examples of index values are: melanin, a pigment that can be found in most organisms has a refractive index between 1.6-1.7, extracellular fluids with n of 1.35-1.36 and for mitochondria, organelles and other cell components 1.38-1.41.

Imaging through biological specimens containing clusters of cells or blood vessels can be slightly improved if extra care is taken during the sample preparation stage. This usually is done by selecting appropriate mounting and immersion media whose refractive index values will be as close as possible to the refractive index of the sample to be observed. Tables 1.2

Mounting medium	Refractive index
ProLong Gold (Invitrogen)	1.39-1.46
Vectashield Medium	1.457
Permount (Fisher Sci.)	1.518-1.521
50% Glycerine	1.416
90% Glycerine	1.46
Water	1.338
Ethanol	1.36
Polyvinyl Alcohol	1.52-1.55
Acetone	1.36
Gel Mount (Biomeda)	1.3641

Table 1.2: Refractive indices of common mounting media.

Immersion media	Refractive index
Water	1.338
Air	1.0003
Cedar oil	1.516
Canada Balm	1.52
Glycerol	1.45- 1.46
Mowiol	1.46
100% PBS pH 8,9	1.34
Zeiss Immersol	1.518
Olympus silicon oil	1.40
Nikon NF oil	1.515

Table 1.3: Refractive indices of common immersion media.

and 1.3 contain some values of mounting and immersion media refractive indices that are traditionally employed in sample preparation. Other techniques that are often employed to overcome refractive index inhomogeneities include surgical removal of large structures (e.g. part of a skull for brain imaging, (Kong & Cui (2015))) or the use of optical clearing agents (Tanabe et al. (2015); Zhu et al. (2013)). Both techniques are employed, nonetheless these are not completely innocuous for living animals.

It is for these reasons that in the past decade, adaptive optics has been used to try to correct the aberrations introduced by the samples and the optical components that form part of the setup of confocal and multi-photon microscopes. The ability to achieve diffraction limited resolution in these type of microscopes is ultimately determined by the ability to overcome aberrations when the beam is focused deep into the sample. Considerably better resolution and signal levels are achieved in confocal and multi-photon microscopes when the excitation and emission paths are both diffraction limited, compared with those where no corrections were performed. Based on the imaging modality of the microscope employed, confocal or multi-photon, this will require the correction of either both or only one path respectively. In confocal microscopes, light passes through the sample twice, thus correction must be performed for both paths. In multi-photon microscopy, fluorescent light is only originated from the focal plane/focal spot, so correction of aberrations in the emission path is not required. In this case, aberration corrections are only performed in the illumination/excitation path. Wavefront correction can be implemented using active elements such as deformable mirrors (DM) or liquid crystal spatial light modulators (LC-SLM).

A conventional adaptive optics system, such as those implemented in astronomy, comprise a wavefront sensor, a control system and a correction element (Hardy (1978); Tyson (2010)). The wavefront sensor's task is to measure the aberrations that need to be corrected. In the literature, many types of sensors have been implemented, the most widely used being the Shack-Hartmann sensor (Hardy (1978); Tyson (2000, 2010)). The control system is in charge of processing the data obtained during the wavefront sensing stage and computing signals that will be employed to remove the aberrations. The correction element is driven by the signals computed by the control system.

A different approach permits the design of an adaptive optics system without the use of a wavefront sensor. Wavefront sensorless AO attempts to correct aberrations based on optimisation of parameters in the image, rather than through measuring the wavefront with a wavefront sensor. This type of scheme has already been implemented and tested in confocal and multi-photon microscopes (Booth (2007a)). Its implementation is based on the fact that minimal modifications are needed to the microscope setup, compared with the implementation of a Shack-Hartmann wavefront sensor system.

Different optimisation schemes can be used, such as genetic algorithms (GA), hill climbing (HC), random search and adaptive random search (RS & ARS) (Wright et al. (2005); Albert et al. (2000)). When non-biological samples are employed, good results have been achieved in confocal and multi-photon microscopes. In this case, as the nature of the aberrations introduced by the sample are static, the algorithm chosen is typically one that will achieve the best resolution (Wright et al. (2005); Sherman et al. (2002)) as the amount of time required to obtain the best resolution does not play an important role. In more complex scenarios as when biological samples are studied, the algorithm employed must balance speed and resolution. For cases where the sample persistence time is short, high speed is required. Even in cases where the algorithm employed is fast enough, there might be issues concerning the ability of the algorithm to find a global maximum/minimum value. Sometimes algorithms will instead find just a local maximum/minimum, then the correction implemented with these values will not be completely effective. Methods based on modal wavefront sensing (Booth et al. (2002); Booth (2006, 2007b); Thayil & Booth (2011); Facomprez et al. (2012); Débarre et al. (2009)) do not have problems converging to a global maximum and also required lower number of iterations. In this case the correction is optimised by applying a set of trial aberrations, generally described using Zernike polynomials, and measuring

an image quality metric M for each of them until enough information about the wavefront aberration is obtained. Generally *a priori knowledge* about the function to be optimised is required. With the information recorded in these cases, a new set of modes is built and these are applied to the corrector element. The sample exposure time critically depends on how efficiently the information is gathered on each trial. Longer exposure time may lead to photo-toxicity and photo-bleaching, affecting the sample structure.

Other techniques such as that implemented by (Ji et al. (2010)), in a two-photon microscope, involve the correction of aberrations based on the division of the objective rear pupil into N segments. The corrector device, in this case a SLM, delivers bundles of light to the different segments while an image of the point-spread function (PSF) is obtained using a photo-detector. With these images, it is possible to isolate those segments that introduce particular changes to the PSF. From here it is possible to avoid the use of some segments or to correct them.

All these wavefront correction schemes rely on the use of fluorescence excitation. Samples might contain fluorescent beads, be strongly and widely stained or correspond to genetically modified specimens. The sample preparation method will depend mainly on the reason why the sample is being investigated. As an example, in histology where the microscopic anatomy of cells and tissues of plants and animals is studied, sample preparation is commonly performed by sectioning, staining and mounting cells and/or tissue on a microscope slide. The consequences for the tissue after being passed through these different stages will be variations in the tissue structures. Furthermore, there might be cases where samples might not be uniformly stained or micro-spheres might not be evenly distributed throughout the whole sample. When samples are translation invariant and the aberrations are static, this does not represent a major problem, as the same correction can be employed for different areas based on the use of *memory effect* (Freund et al. (1988)). Briefly, the *memory effect* describes an intrinsic isoplanatism of the scattering process for small angles even in strongly scattering media. By tilting the wavefront incident on a scattering medium, the emerging speckle patterns shifts accordingly and does not immediately decorrelate. Thus this isoplanatism can be exploited in different imaging techniques. However, when the sample persistence time is shorter than the time required to measure and correct the aberrations for wavefront sensorless adaptive optics, image enhancement might not be obtained. Numerous iterations during this time will lead to fluorophores photo-bleaching and the tissue may undergo changes due to photo-dynamic changes (photo-toxicity).

Following the same approach of the use of fluorescent probes but based on direct wavefront sensing, different procedures can be encountered in the literature. Good results using these direct wavefront sensing implementations have already been obtained in biological and non-biological samples, based on the use of a Shack-Hartmann wavefront sensor (Tao et al. (2011a,b); Cha et al. (2010); Bueno et al. (2010); Gualda et al. (2010)). The signal employed to measure the aberrations corresponds to the fluorescence from micro-spheres that have been embedded in the sample as reference beacons.

A completely different approach already implemented in confocal and two-photon microscopes is based on the use of backscattered light and is called Coherent Gated Wave front Sensing (CGWFS) (Feierabend (2004), PhD thesis). Implementation of this approach falls under the umbrella of direct wavefront sensing, as two fundamental principles form the basis for CGWFS, phase measurement and depth discrimination with the help of phase shifting interferometry. It is important to highlight that not all the reflected light can be used indiscriminately for wavefront sensing, because most of the backscattered light does not carry information about the focal region. Only singly-scattered light can be employed to determine the wavefront distortion and it represents just a small fraction of the total backscattered light. (Feierabend et al. (2004); Rueckel & Denk (2006, 2007)) . Singly- and multiply-scattered light, together with out-of-focus light, can be discriminated by means of light arrival time. This selection is done using a coherence gate, a similar approach to optical coherence tomography. In this case, coherence gating is achieved by phase-shifting interferometry, rejecting the optical path length that does not match the reference arm length and extracting the phase and thus the wavefront aberration information. In this way the phase of the in-focus scattered light is determined but needs to be unwrapped. Speckle and granular intensity pattern are present in CGWS due to coherence effects. The implementation of a virtual Shack-Hartmann has been employed to overcome these problems (Feierabend et al. (2004)).

We propose a new wavefront correction based on direct wavefront sensing of backscattered light coming from the focal plane for a laser scanning confocal microscope. Direct wavefront sensing is achieved by the use of a Shack-Hartman sensor. To constrain the amount of out-of-focus light coming from the sample and taking part of the centroid estimations, a pinhole is utilised to control this problem.

This work is subdivided into two main parts: In the first part, theoretical problems associated with the use of a direct wavefront sensor are addressed. Problems arise at the wavefront sensing stage, particularly in spot detection and spot displacement for the Shack-Hartmann due to noise corrupting the measurements, together with discriminating singly- from multiply backscattered light (Chapter 2). The emphasis lies on the investigation of a more robust, efficient and accurate centroid algorithm for spot detection in a noisy environment. Another problem related to direct wavefront sensing arises within wavefront reconstruction, a process that can be included in the control stage. In order to obtain the signals to drive the corrector element based on the finite amount of data that is acquired with the SHWFS, it is necessary to reconstruct the wavefront phase of the aberrations being measured. To achieve this, different approaches are presented and compared with the method implemented in this work (Chapter 3). In the second part, the experimental system that was built is presented (Chapter 4). The solutions presented in these chapters are implemented in the system control stage. Results from corrections in samples made of agarose and leaves, together with cell spheroids are presented. This thesis closes with a summary (Chapter 5) and an conclusions (Chapter 6).

1.2 Laser Scanning Confocal Microscopy

1.2.1 Historical perspective

The concept of confocal microscopy was first developed by Marvin Minsky around the 1950s (Minsky (1961)). He developed the confocal microscope while he was a post-doctoral student at Harvard University, with the idea of imaging unstained brain tissue samples. The first completely mechanical scanned confocal microscope was developed years after Minsky by Egger, who published the first recognizable images of cells in 1973 (Egger & Davidovits (1973)). It was around the late 1980s that the utility of confocal imaging in the examination of fluorescent biological specimens was implemented. Later, advances in computers and laser technology lead to a growing interest in the construction and development of confocal microscopes for biological applications. Substantial advances in optics and electronics allowed for more stable and powerful lasers, better scanning mirror units, better thin film dielectric coatings and detectors. Nowadays confocal microscopes can be considered as completely integrated electronic systems, with the optical microscope playing an essential part in the whole configuration. Together with the optical setup, the whole system might consist of one or more detectors, a computer, a beam scanning arrangement, along with different laser

systems in order to allow multiple fluorophores to be excited. These confocal microscopes are employed for routine investigations on molecules, cells, and living tissues that were not possible previously.

Confocal microscopes offer several advantages over conventional wide-field optical microscopy. These advantages include the ability to control depth of field, reduction/elimination of background information coming from planes above or below the focal plane (which leads to image degradation), and the ability to collect multiple optical sections from thick specimens. The principal concept around the confocal approach is the use of spatial filtering techniques to eliminate out-of-focus light in specimens thicker than the immediate plane of focus. The reason behind its popularity is due to the relative ease with which high quality images can be obtained from specimens that have been prepared for conventional fluorescence microscopy. At the same time, it is well suited for a number of applications in cell biology, regardless if fixed or live cells and tissues are used.

Compared with a conventional wide-field microscope, confocal microscopy provides an improvement in both axial and lateral optical resolution. In wide-field microscopy, secondary fluorescence is emitted by the whole excited volume, particularly for specimens thicker than 2 μm, obscuring features that lie in the focal plane, and losing the majority of fine details.

Typical confocal fluorescence microscopy is based on a linear effect, one photon is absorbed by the fluorescent molecule and this molecule will emit a single fluorescent photon. The amount of fluorescence generated scales linearly with the excitation power, this means that if excitation is increased by a factor of two, then twice as much fluorescence will be generated, assuming that there are sufficient fluorescent molecules to avoid saturation. In comparison multi-photon microscopes rely on a non-linear interaction between the light and the matter. In this case, in multi-photon microscopy, the fluorescence is generated only at the focal spot, and a pinhole is thus not necessary at the detector to reject out-of-focus light. However, in addition to the high cost associated with appropriate light source for multi-photon microscopy, photo-bleaching rates are increased (in comparison to confocal microscopes), as a higher flux of photons at the focal spot will activate more photo-bleaching pathways (Brovko (2010)).

1.2.2 Principles of Confocal Microscopy

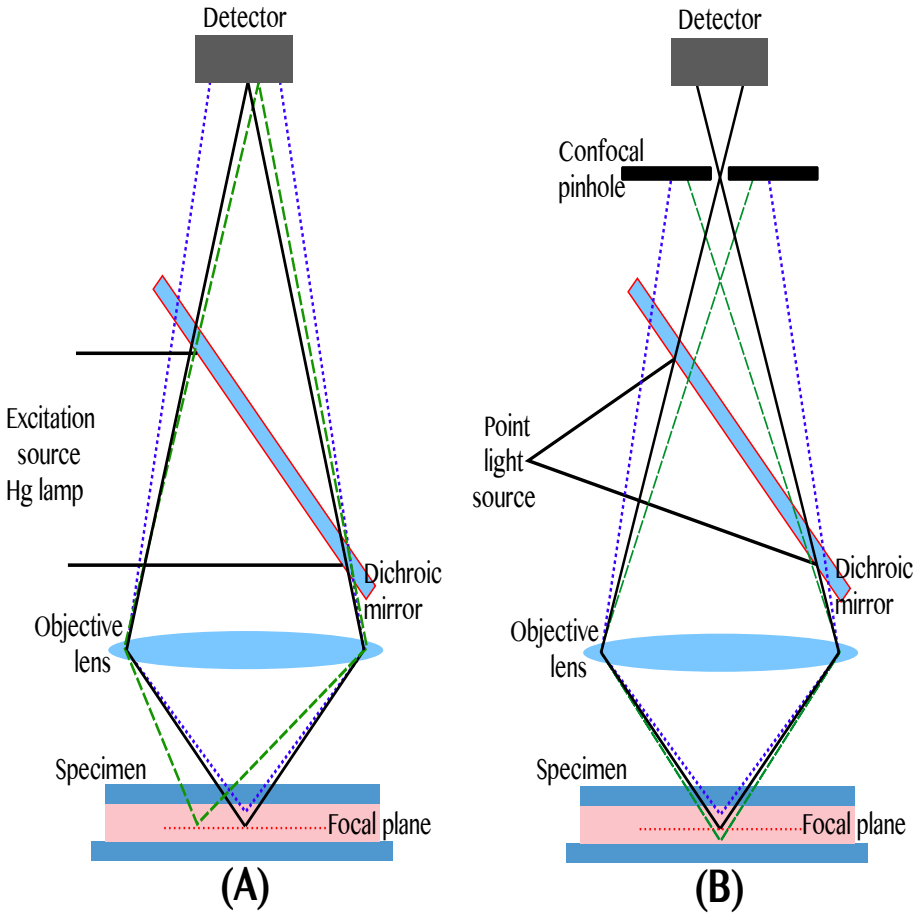


Figure 1.2: Simple schematic diagram of the optical pathways and basic components in a wide-field and a confocal microscope, the main difference corresponds to the use of a confocal pinhole. **(A) Wide-field microscope:** the light source employed is generally a Mercury lamp (Hg lamp). Fluorescent emitted by the specimen occurs through the whole excited volume and obscure resolution of features that lie in the focal plane. **(B) Confocal microscope:** A point light source is employed and generally obtained from the output of a laser coupled to an optical fibre or a laser passing through a pinhole aperture that is located in a conjugate plane with the focal point in the specimen. A confocal pinhole removes unwanted light coming from planes located above and below the focal plane.

A conventional wide-field microscope is depicted in Figure 1.2 (A), together with the confocal principle in an epi-fluorescence laser scanning microscope, Figure 1.2 (B). Coherent light emitted by a point light source (e.g. laser coupled to an optical fibre) is reflected by a dichroic mirror and scanned across the sample at a defined focal plane.

Light emitted from the specimen is redirected towards a detector (e.g. a photo-multiplier tube). To separate excitation light from emitted light a dichroic mirror and an emission filter are generally employed. To reject out-of-focus light coming from the sample a pinhole is positioned in front of the detector. Fluorescence emitted from points on the specimen (at the same focal plane) will pass back through the dichroic mirror and will be focused to a point at the detector pinhole aperture. Fluorescence emitted from points located above and below the objective focal plane are not confocal with the pinhole (out-of-focus light in Figure 1.2 is represented by dashed green and dashed blue lines) and these will form enlarged defocused Airy disks in the aperture plane. As only a small amount of the out-of-focus light will pass through the pinhole, most of this out-of-focus light will not be detected by the detector and will not contribute to the final image. These new planes will then be confocal with the pinhole at the detector and the light point source. Thus, to obtain a three-dimensional image, it is necessary to scan the excitation spot, usually by using galvanometer mirrors in a raster pattern across the specimen plane (also referred to as point scanning, 2D imaging, XY-scanning) and move the objective along the optical axis (Z-scan). This can also be achieved by moving the stage where the specimen is mounted along the optical axis or employing precision stages that allow movements in all 3 directions (XYZ). It is important to note that the confocal image of a specimen is reconstructed, point by point, from emission photon signals by the detector and the respective electronics, and a real confocal image cannot be directly observed through the microscope eyepieces.

The most important component of the microscope is the pinhole aperture, which acts as a spatial filter at the conjugate image plane positioned directly in front of the detector. Several apertures of varying diameter can be implemented on a rotating turret enabling the user to adjust the pinhole size (and optical section thickness). By reducing the pinhole diameter, higher diffraction orders of the Airy disc pattern can be eliminated. The size of this diffraction pattern and thus the focal volume in the sample is controlled by the numerical aperture (NA) of the system's objective lens and the wavelength of the light source used (λ). These parameters are directly related to the system's resolution. If we assume a complete and uniform illumination of the back aperture of the objective lens, the maximum lateral

and axial resolution of a confocal microscope can be defined as

$$r_{\text{lateral}} = \frac{0.37\lambda}{NA} \tag{1.1}$$

$$r_{\text{axial}} = \frac{1.4\lambda\eta}{NA^2} \tag{1.2}$$

where η corresponds to the refractive index of the immersion medium.

For example, if the pinhole diameter is set to 1 Airy unit then only the first order of the diffraction pattern makes it through the aperture to the detector while the other higher diffraction orders are blocked, all this at the cost of a slight decrease in brightness. Variations in the degree and uniformity of illumination of the objective can lead to lower resolution, as not the whole numerical aperture is employed.

Some disadvantages of this type of microscope are related to their cost, which can range up to an order of magnitude higher than wide-field microscopes. Their increased price are related to the limited number of excitation wavelengths available with common lasers as light sources. In contrast, wide-field microscopes use mercury or xenon based arc-discharge lamps to provide a full range of excitation wavelengths in the ultraviolet, visible, and near-infrared spectral regions. Similarly, another downside is related to the use of lasers to image living cells and tissues, as problems associated to photo-toxicity and photo-bleaching might occur.

Nevertheless, the principal advantage of laser scanning confocal microscopy is the ability to produce thin optical sections (ranging between 0.5 to 1.5 μm) in specimens in which thicknesses can have up to 50 μm or thicker. Image information is restricted to a well-defined plane inside the sample, rejecting signals arising from other planes in the specimen. Contrast is dramatically improved over wide-field techniques due to a reduction in background fluorescence with a subsequent increase in signal-to-noise ratio. In addition, optical sectioning eliminates problems that can occur during sample sectioning, as a thicker sample can be employed. Confocal optical sectioning enables the investigation of both in-vivo and ex-vivo samples under a variety of conditions with enhanced clarity. The ability to acquire optical sections sequentially through the volume of a specimen, allows to elucidate the numerous interrelationships between structure and function of cells and tissues in different biological investigations (Conn (2010)).

Additional advantages include the ability to adjust magnification electronically by varying the area scanned by the light source without having to change objectives. This feature is termed the zoom factor.

1.3 Shack-Hartmann wavefront sensor

The components of a conventional adaptive optics system, are a wavefront sensor, a control system and a correction element. Some of the more widely-employed type of wavefront sensors are the Shack-Hartmann sensor, the curvature sensor (Hardy (1978); Tyson (2000, 2010)) and the pyramidal wavefront sensor (Tyson (2010); Chew et al. (2006); Verinaud (2004)).

The Shack-Hartmann wavefront sensor is simple, compact, relatively vibration insensitive and is wavelength independent. These advantages make it easy to use in a large number of applications, from astronomy to high energy lasers, along with ophthalmology, optical testing and microscopy. The Shack-Hartmann wavefront sensor provides a simultaneous phase and irradiance distribution measurement that does not rely on an external source.

1.3.1 Principle of operation

The Shack-Hartmann wavefront sensor (SHWFS) is a variant of the original Hartmann sensor, where a grid of holes was employed to sample the wavefront (Malacara (2007)). The introduction of lenses rather than a grid provides better light efficiency, because all the light is collected by the lenses (Platt & Shack (2001)). This is important especially in those cases where faint objects are to be studied.

The sensor consists of two parts: a lenslet array and a detector. The incoming wavefront is dissected into a number of small samples, determined by the number of lenslets in the array. The lenslet array is placed in a conjugate pupil plane. If the wavefront is planar, each lenslet forms an image of the source at its focus, Figure 1.3 (A). If the wavefront is aberrated or disturbed, each lenslet will receive a small portion of the aberrated wavefront and will form an off-axis image in its focal plane, Figure 1.3 (B). The position of these focal spots will be directly related to the average wavefront slope across the lenslet. Thus a map of wavefront slopes is obtained. It is important to highlight that the SHWFS usually requires a reference plane wave that might be generated from a source in the instrument, in order to

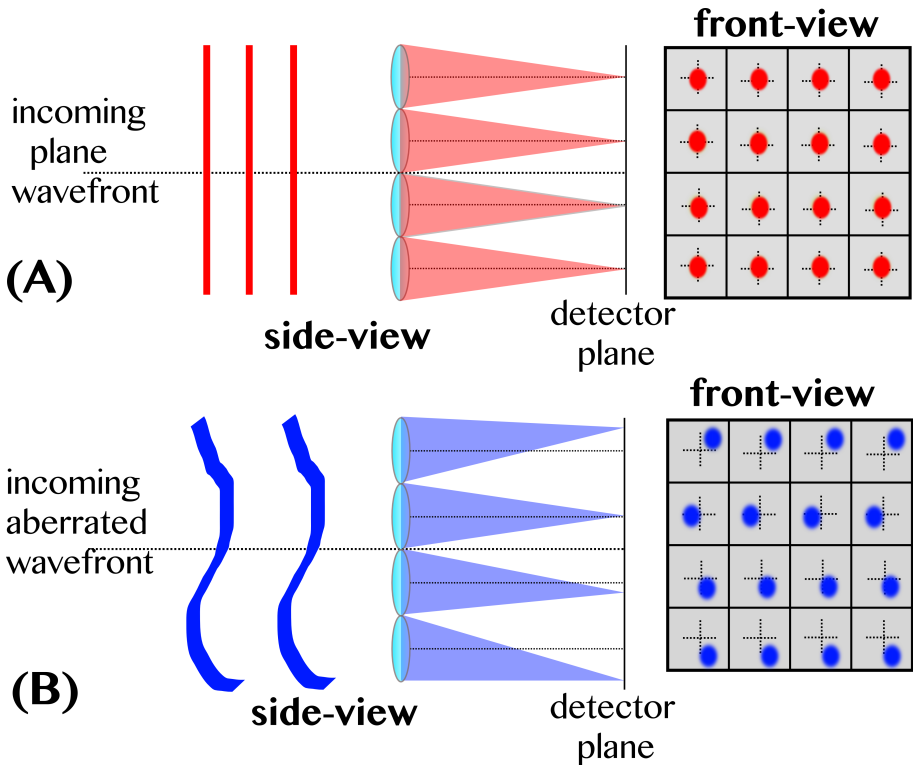


Figure 1.3: Shack-Hartmann wavefront sensor spot positions based on the nature of the incoming wavefront. (A) Plane wavefront: the spot are located at the centre of each sub-aperture. (B) aberrated wavefront: the spot are displaced from the centre.

calibrate the focus positions of the lenslet array.

The detector is utilised for position sensing, in order to determine the focal spot position. For a pixelated sensor, such as a CCD, the location of the focal spot is determined from the light distribution on the detector array. A number of position estimators have been studied in the literature (Thomas (2004)) for tracking systems such as: simple centroid (CoG), thresholding (TCoG) and weighted centre of gravity (WCoG). The simplest and most direct way to calculate the position of a symmetric spot is by centre of gravity position $(x_{\mathrm{CoG}}, y_{\mathrm{CoG}})$ or CoG,

$$x_c = \frac{\sum_{i,j} x_{i,j} I_{i,j}}{\sum_{i,j} I_{i,j}} \quad y_c = \frac{\sum_{i,j} y_{i,j} I_{i,j}}{\sum_{i,j} I_{i,j}} \tag{1.3}$$

where $I_{i,j}$ and $(x_{i,j}, y_{i,j})$ are the signal and the position coordinates of the CCD pixel (i, j). The sum is made over all the pixels associated with a lenslet field. The normalization factor $\sum_{i,j} I_{i,j}$ makes the sensor relatively insensitive to scintillations (Tyson (2000)). This formula is widely used, however it has some limitations, especially when real spots are used and noise is present in the measurements.

The wavefront slope θ is determined by comparison between the measured centroid and the reference centroid, determining the spot displacement $d_{x,y}$ (Figure1.4). For a measurement with reference centroids $(x_{\mathrm{ref}}, y_{\mathrm{ref}})$, and one lenslet with a focal distance f, the wavefront slope is given by

$$d = f \bullet \tan(\theta), \;\; \rightarrow d = f \bullet \theta \;, for\, small\, \theta$$

where d is given by,

$$d_x = x_c - x_{\mathrm{ref}} \quad , \quad d_y = y_c - y_{\mathrm{ref}} \tag{1.4}$$

then,

$$\frac{\partial W}{\partial x} = \theta_x = \frac{d_x}{f} \quad , \quad \frac{\partial W}{\partial y} = \theta_y = \frac{d_y}{f} \tag{1.5}$$

Finally the wavefront is related to the slope through the definition of the gradient:

$$\nabla W = \frac{\partial W}{\partial x}\hat{\imath} + \frac{\partial W}{\partial y}\hat{\jmath} \tag{1.6}$$

Once a gradient map is known, the wavefront must be determined through some form of spa-

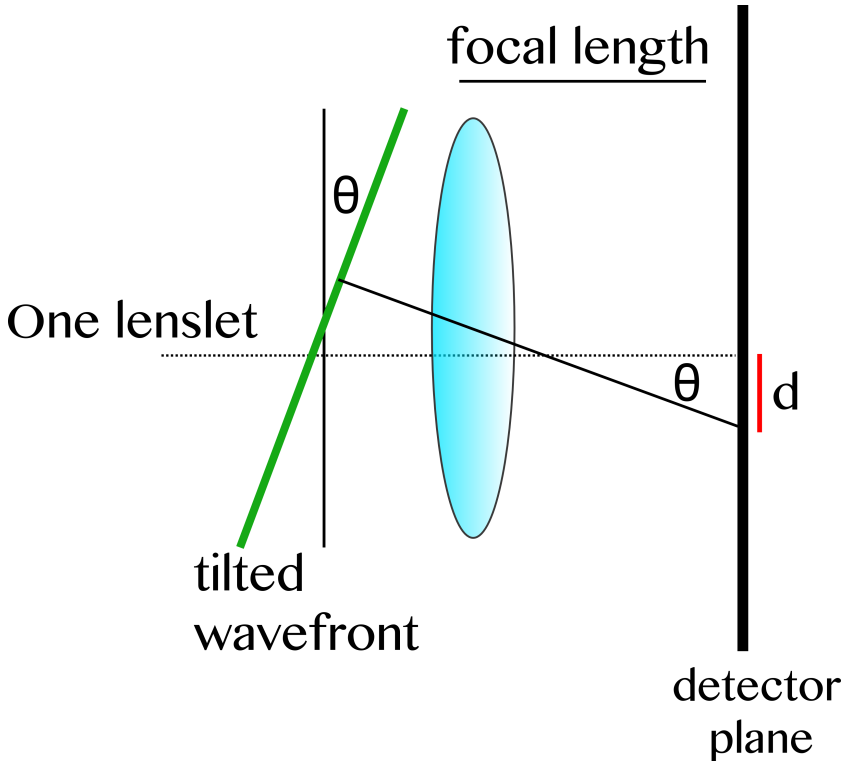


Figure 1.4: Spot displacement determination $d_{x,y}$, considering a single lenslet from the array.

tial integration. This step is called wavefront reconstruction. This topic will be presented in deeper detail in Chapter 3.

Chapter 2

Wavefront sensing

Many wavefront sensing techniques have previously been implemented to measure the aberrations introduced by the sample in microscopy. As we have seen in the previous chapter, good results have been obtained when using both direct and indirect wavefront sensing. Even though direct wavefront sensing techniques are faster compared with the indirect ones, the main problems with these approaches resides in the reconstruction of the wavefront based on the measured data. The Shack-Hartmann sensor is the most popular choice and it is employed in different AO systems, mainly due to its simplicity. Its accuracy, which largely determines its performance, depends on having a robust centroid algorithm. Any source of error in the determination of the centroid position will propagate to the wavefront reconstruction stage, reducing the performance of the system. Then, centroid positions is at the core of the Shack-Hartmann sensor. Any improvement to determine the centroid positions in a more accurate way, will lead to an improvement in the system performance.

Optimization of SHWFS centroid computation has been given considerable attention in the literature. In this Chapter, we first present a brief summary of the algorithms generally implemented for centroid estimation when a Shack-Hartmann sensor is employed. After that, we present a new algorithm that we implemented for centroid estimation in confocal microscopy. Computer generated data and real data obtained from a working AO system were employed to compare the proposed algorithm performance versus a traditional centroid algorithm. The other centroiding algorithm employed corresponded to the Centre of Gravity method (CoG). Discussion about the difference in performance between the two methods are addressed at the end of this Chapter.

2.1 The principle of centroid estimation

The Shack-Hartmann sensor samples the incident wavefront reaching the system aperture by means of a lenslet array, which produces an array of spots at the detector. The measured wavefront is analysed by means of the displacements of the centroids of these spots. As mentioned in the previous chapter, the spot displacement is directly proportional to the local wavefront slope averaged over each subaperture. Then, a good estimation of the wavefront distortion is obtained if good measurements of the spot displacements are achieved. The accuracy of these measurements depend on different factors. These factors generally are the noise strength, the size of the detector, the sampling factor and the size of the field-of-view.

In this section we briefly present three main classes of algorithms employed for centroid detection in Shack-Hartmann sensors. The considered algorithms: centre of gravity approaches (CoG), correlation methods (Corr) and the quad-cell estimator (QC).

Coarse sampling of the CCD camera employed to record the spots usually corrupts the measurements. The photon noise from the light source employed (in astronomy a guide star), the CCD readout noise (RON) and the earth's atmosphere, by introducing speckle noise in the data, also corrupts the measurements. It is important to highlight that in the presence of high readout noise, the spot can be completely lost in the detector noise. In this case, it is important to use a centroid algorithm capable of dealing with this situation, otherwise the centroid calculation can be completely wrong. This has a big impact on the system's performance.

In the literature, particularly when CoG approaches have been considered, different types of algorithms have been developed in order to improve the most basic CoG calculation. The use of the mean-square error estimator (van Dam & Lane (2000)) or maximum a posteriori (Sallberg et al. (1997)) are some examples.

As many parameters are involved in the estimation of the centroid calculation accuracy, different ways to approach these problems can also be found. Error associated to the size of the CCD and the truncation problem that arise from it have been studied by (Irwan & Lane (1999)). The truncation error occurs simply because the spot has a certain width on a detector, and limiting the region of integration involves truncating part of the spot. In order to simplify the analysis (Irwan & Lane (1999)), omitted readout noise in the data.

An important variable that needs to be considered in the centroid estimation is related to linearity. It is generally assumed that in an AO system working in a closed loop scheme, the spot centroids do not change their position considerably from one frame to the next, in this case, linearity is not essential. However, in other applications, when it is necessary to introduce an intentional offset to the spots in order to compensate for non-common path aberrations (Sauvage et al. (2007); Yusufu & Dubra (2014)) linearity becomes an important factor. Finally, when faint sources are employed, a more sensitive centroid algorithm is required. Generally the algorithm employed on these cases are variations of the CoG, where some threshold function or weight function are used. These algorithms will be explained later in this section.

Throughout this section we consider only one spot in one subaperture of the Shack-Hartmann sensor. Generally the spot will be sampled by a detector with a field-of-view (FoV) of width W_p pixels. The spot intensity distribution $P(x, y)$ is transformed into an array of pixel intensity values $I_{i,j}$, which is corrupted by photon and detector noise. We define the estimated spot centroid by (x, y).

2.1.1 Type of centroid algorithms

1.- **Simple Centroid**: The centre of gravity is the simplest and direct option to calculate the position of a symmetric spot. Its formula is given by

$$x_{\mathrm{CoG}} = \frac{\sum x_{i,j} I_{i,j}}{\sum I_{i,j}} \tag{2.1}$$

where $x_{i,j}$ is the abscissa of the i, j pixel and $I_{i,j}$ is its intensity. It corresponds to the most widely used formula in AO systems (Thomas et al. (2006)). However, some drawbacks are associated to the use of spots in the presence of noise. A real spot is a diffraction spot formed by the subaperture that has been distorted by the earth's atmosphere in the astronomical case.

When working at low light levels, the readout noise contribution is dominant. In order to reduce the noise effect in CoG, it can be implemented by using the smallest number of pixels possible. When this modification is made, a smaller number of pixels are employed in the calculation, we can pass from the CoG method to the quad-cell method

or to other modification of the CoG method.

2.- **Improved CoG algorithms:** As mentioned before, error due to detector noise can be reduced if we take into account a smaller number of pixels to make the calculation. Generally two approaches are the most common to be followed: *Thresholding centre of gravity* (TCoG) or *Weighted centre of gravity* (WCoG) (Nicolle et al. (2004); Prieto et al. (2000); Baker & Moallem (2007)).

The thresholding method is based on the use of only some selected pixels from the whole field-of-view. This can be done by selecting a fixed number of the brightest pixels or by choosing pixels with values above some threshold. Considering the latter case, we begin by determining the pixel with the maximum intensity $I_{\max}$, then a threshold I_t is generally selected. The threshold is given by $I_t = tI_{\max}$, where t is a parameter to be optimised. Once the threshold is calculated it is necessary to substract this amount from the spot image before the CoG calculation, otherwise the measured centroid will be erroneous. The centroid is computed using

$$x_{\mathrm{TCoG}} = \frac{\sum_{I>I_t} x_{i,j}(I_{i,j} - I_t)}{\sum_{I>I_t}(I_{i,j} - I_t)} \tag{2.2}$$

where $x_{i,j}$ refers to i, j pixel and $I_{i,j}$ is its intensity.

For those cases when we work at low light levels, it can be difficult to detect the brightest pixel against the readout noise (Vyas et al. (2009); Roopashree et al. (2011b)). In those cases, it is possible to add an extra condition for the threshold selection that takes into account the detector readout noise. Thus, the threshold selection is defined by $I_t = \max(tI_{\max}, mN_r)$, where N_r is the detector readout noise and m is given by the amount of readout noise that we want to include in the measurements. For low signal-to-noise ratio, a value equal to $3N_r$ removes most of the noisy pixels without removing the signal. $3N_r$ has been found to be the optimum value, while $2N_r$ still admits noise and $4N_r$ cuts part of the signal (Thomas (2004)). Even though, this approach represents an improvement compared to the CoG and it is simple to implement, it has the drawback associated with the difficulty in choosing an optimum value for the threshold t. Thus, the weighted centre of gravity arises as a more efficient method (Roopashree et al. (2011b)).

The idea of the weighted centre of gravity is based on giving a weight to the different pixels that comprise the image based on their flux. In this case, the noisy pixels, that are located outside of the spot core, are attenuated but not eliminated.

In this case we define a weighting function $W_{x,y}$, that depends on the spot's FWHM. Here, the centroid is calculated using the expression

$$x_{\mathrm{WCoG}} = \frac{\sum x_{i,j} I_{i,j} W_{i,j}}{\sum I_{i,j} W_{i,j}} \tag{2.3}$$

where $x_{i,j}$ is the abscissa of the i, j pixel, W_{ij} is its weighting coefficient, and $I_{i,j}$ is its intensity. Depending on the shape of the lenslet aperture, a circular window of radius r can be employed, such that $W_{i,j} = 1$ when $\sqrt{x^2 + y2} < r$ or a square window. Based on the weight function, there are two versions of the WCoG, depending if the weight $W_{i,j}$ is a fixed quantity or not (Baker & Moallem (2007)). When this last method is employed, it requires to optimise the centroid algorithm performance (Nicolle et al. (2004)).

The behaviour with respect to photon noise or readout noise are different for the WCoG compared to the CoG and it depends on the weight function employed (Thomas (2004)).

3.- **Quad cell (QC)**: it corresponds to the specific case of the CoG when a 2×2 pixels array is used. In this case the field-of-view is determined by the pixel size and it has the characteristic that the spot is generally under-sampled. This centroid method is widely used in astronomical AO, where weak signal detection from a guide star is detected (Herriot et al. (2000)). Based on the small number of pixels employed, the weak signal is better detected against the readout noise and it can be reduced even further if slow CCD readout is carried out. In this case, the centroid is divided into two halves and the difference in intensity between one half and the other determines the centroid. This is given by

$$x_{\mathrm{QC}} = \frac{I_{\mathrm{left}} - I_{\mathrm{right}}}{I_{\mathrm{left}} + I_{\mathrm{right}}} \tag{2.4}$$

where I_{left} and I_{right} are the intensities on the left and right halves of the detector.

The response of the QC algorithm is non-linear, so considerable effort is necessary to

calibrate it particularly for real-time measurements (Véran & Herriot (2000)). This centroid method is only efficient when a low flux and a noisy detector are employed. For more accurate measurements of wavefronts, the other centroid methods are better in all other circumstances.

4.- **Correlation algorithm (Corr)**: This method computes the correlation between an image obtained from the CCD and a reference spot (or template). The cross-correlation function (CCF) between the CCD image and the template is calculated by using Fourier transform, given by

$$cc(x, y) = I \otimes T_w = \sum_{i,j} I_{i,j} T_w(x_i + x, y_j + y) \tag{2.5}$$

where $cc(x, y)$ is the CCF, I is the image and T_w the reference spot or template.

Once the cross-correlation function is calculated $cc(x, y)$, the position of the spot centre is determined by the maximum of the resulting images in x and y direction. To determine the precise position of the maximum x_{corr} on the image, different approaches can be used. Centroid calculation with thresholding, fitting a parabola to three points around the maximum or Gaussian fitting can be employed (Roopashree et al. (2011a); Poyneer (2003)). Almost all methods of maximum position determination are identical and linear when images of Gaussian spots are imaged (Thomas et al. (2006)). If the imaged Shack-Hartmann spot is highly aberrated and non-symmetric, the different fitting methods will be affected as some information contained in the wings of the cross-correlation function can be neglected even though it is important.

The centroid method with thresholding represents a simple approach for peak location that works well under different scenarios. It can be optimised by adapting the threshold value as a function of the dominant noise. If readout noise is dominant, a high threshold value is selected, then only the sensitive information is contained in the peak. If photon noise is dominant, a low threshold is employed, allowing the information contained in the wings of the cross-correlation to be considered on the peak calculation (Thomas et al. (2006)).

2.2 Quadratic program for centroid estimation

The first centroid algorithm implemented in our system was the centre of gravity method (CoG). This algorithm was employed to find the position of the SH spots when the system was calibrated using a flat wavefront. This method works well under certain conditions, such as when we initialise the system or when a mirror is employed as the sample. As we move to more complex samples, it is necessary to use a different centroiding method. In the literature it is possible to find profiles of typical spots for aberrometric studies, based on real data and artificial eyes employed for calibrations (Prieto et al. (2000)). From this research, it possible to understand that some background light that forms part of the information obtained with a SHWFS corresponds to light scattered by deeper layers that form the retina. In confocal microscopy and particularly when using a Shack-Hartmann sensor, each SH spot is formed by light coming from the focal plane, carrying the necessary information to measure the aberrations. However, the total light gathered to form the spot also contains out-of-focus light from planes located above and below the focal plane. This light needs to be excluded from the spot coordinate calculations. Then, a delicate approach to background rejection and good performance under different SNR values is the desired goal.

First, the Shack-Hartmann spots were modelled by the use of random normal distributions with fixed amplitude but varying their widths and centre positions. A normal distribution was employed to simulate the noise added to the spots. Pre-defined functions provided in Python (scipy.optimize) were used to fit the generated data (*curve fit, leastq* and *fmin*). With these functions, good fitting results were obtained, however the major concern in these cases was the computational time involved. These functions are based on iterative processes and values were supplied as initial guesses to test them. More accurate values for initial parameters can decrease the number of iterations needed to perform the fit and therefore decrease the computational cost of the algorithm. Computation times ranged between 500µs and 6 sec (1 spot - 37 spots) which might be too slow for live correction, particularly in a sample with short persistence time. Changes to these predefined functions were not tried as these functions are already optimized to work in off-line data analysis.

The centroid algorithm that we present in this thesis can be understood as a hybrid between a matched filter (Baker & Moallem (2007); Akondi & Vohnsen (2013); Leroux & Dainty (2010)) and a quasi-newtonian optimization algorithm (Press et al. (1992)). The matched filter algorithm estimates the shift that maximizes the scalar product between a

reference image (in our case a Gaussian mask) with the actual data. The scalar product between the reference and the data can be considered as a cross correlation. The idea is to maximize the signal while decreasing the effect of noise, this is done in our case by using the Newton's method.

We modelled the spots from the SHWFS as Gaussian distributions. So the two-dimensional PSF can be represented by a general form of the elliptical Gaussian function

$$f(x,y) = A_d \exp\left(-(\alpha(x-x_d)^3 - 2\beta(x-x_d)(y-y_d) + \gamma(y-y_d)^2)\right) \tag{2.6}$$

where A_d represents the amplitude, x_d, y_d are the Gaussian centre coordinates. The coefficients α, β and γ are represented by

$$\alpha = \frac{\cos^2\theta}{2\sigma_x^2} + \frac{\sin^2\theta}{2\sigma_y^2} \tag{2.7}$$

$$\beta = -\frac{\sin 2\theta}{4\sigma_x^2} + \frac{\sin 2\theta}{4\sigma_y^2} \tag{2.8}$$

$$\gamma = \frac{\sin^2\theta}{2\sigma_x^2} + \frac{\cos^2\theta}{2\sigma_y^2} \tag{2.9}$$

$$\tag{2.10}$$

where θ is the angle, in degrees, that gives the direction of the largest FWHM, measured starting from x (vertical direction) in the clockwise direction. We simplify the expression for the general elliptical gaussian, we assume $\alpha = \gamma = \frac{1}{2}$ and $\beta = 0$, then

$$f(x,y) = A_d \exp\left(-\left(\frac{(x-x_d)^2}{2\sigma_x} + \frac{(y-y_d)^2}{2\sigma_y}\right)\right) \tag{2.11}$$

where σ_x, σ_y are the x and y standard deviations (the Gaussian RMS width). If we work over a symmetric spot, then $\sigma_x = \sigma_y = \sigma_d$.

First we need to find the centre of the Gaussian (x_d,y_d), and then the displacement of these coordinates with respect to the flat reference coordinates (Figure 2.1, x_r). To implement the method we first define a *cost* or *objective function*, $I(p) : \mathbb{R} \to \mathbb{R}$, and the aim is to find the values of the parameters p that maximizes the cost function: $p* = \arg\max_{p*} I(p)$. We start our optimisation routine by passing some initial parameters p_0 that are close to the global maximum.

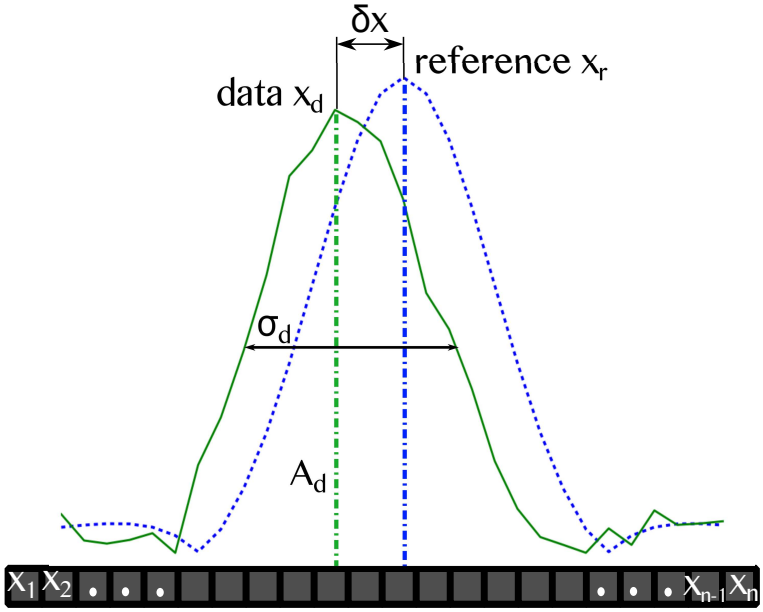


Figure 2.1: Gaussian spot formed by the flat wavefront reference (blue dashed line) and the data (with amplitude A_d and width σ_d, shown in green) in a search block of a size n pixels. The displacement between the two spots is given by $\delta_x = x_r - x_d$.

We defined our cost function as

$$I(A, x, y, \sigma_x, \sigma_y) = \iint f(A, x, y, \sigma_x, \sigma_y) g(x, y) dx dy \tag{2.12}$$

where $f(A, x, y, \sigma_x, \sigma_y)$ represents the system model and $g(x, y)$ corresponds to the data. Given two Gaussian p.d.f, this cost function represents the overlap between both, and we want to maximize this quantity. In this case the parameters to optimise are $\mathbf{p} = [A, x, y, \sigma_x, \sigma_y]$.

In our case the data is an image with finite dimensions that can be generated computationally or directly obtained from the SHWFS. We then define a search box around the flat reference coordinates, where the spot should be found. When working in closed-loop mode, the spot displacements are not large and should not be far away from the flat reference coordinates or the image centre. This represents a major advantage when passing an initial values for the parameters p_0 as these can be related to the coordinate values of the flat reference. It is important to pay attention when selecting the search box dimensions, as we must balance the amount of information and noise contained in the image. The bigger the area

employed, the larger the amount of noise that could be introduced or unwanted information from adjacent spots can be included in the calculations. However, if the area is too small, part of the required information could be lost, especially if the spot is bigger than the selected area. For the model, an image representing a noise-free 2D Gaussian distribution is employed.

To obtain the parameters that maximize this cost function, we employed the Newton's method (Press et al. (1992)), which allows us to fit a quadratic approximation to $I(p)$ using the gradient and the curvature. This is an iterative process that will return a value representing how far away the initial guess is from the optimal value. By using the gradient and the curvature values, the process moves in the right direction until convergence is reached.

The first step to implement this method is to expand the cost function $I(p)$ locally using a Taylor expansion, assuming that p_0 is close to the initial value, giving:

$$I(p) \approx I(p_0) + \frac{\partial I}{\partial p}\Big|_{p_0} (p - p_0) + \frac{\partial^2 I}{\partial p^2}\Big|_{p_0} \frac{(p - p_0)^2}{2} + \dots \tag{2.13}$$

Then we need to find the values that maximize this expression, these are obtained by calculating the derivative of the cost function $\frac{\partial}{\partial p} I(p)$,

$$\frac{\partial I(p)}{\partial p} \approx \frac{\partial I}{\partial p}\Big|_{p_0} \frac{\partial}{\partial p} (p - p_0) + \frac{\partial^2 I}{\partial p^2}\Big|_{p_0} \frac{\partial}{\partial p} \left(\frac{(p - p_0)^2}{2} \right) + \dots$$

$$\frac{\partial I(p)}{\partial p} \approx \frac{\partial I}{\partial p}\Big|_{p_0} + \frac{\partial^2 I}{\partial p^2}\Big|_{p_0} (p - p_0) + \dots \tag{2.14}$$

To find the maximum value

$$\frac{\partial I(p)}{\partial p} = 0 \quad \Longrightarrow \quad 0 \approx \frac{\partial I}{\partial p}\Big|_{p_0} + \frac{\partial^2 I}{\partial p^2}\Big|_{p_0} (p - p_0)$$
$$-\frac{\partial^2 I}{\partial p^2}\Big|_{p_0} (p - p_0) = \frac{\partial I(p)}{\partial p}$$

rearranging we have

$$(p - p_0) = \frac{-\frac{\partial I}{\partial p}\Big|_{p_0}}{\frac{\partial^2 I}{\partial p^2}\Big|_{p_0}}$$

$$\delta p = \frac{-\frac{\partial I}{\partial p}\Big|_{p_0}}{\frac{\partial^2 I}{\partial p^2}\Big|_{p_0}} \tag{2.15}$$

Where, $(\partial I/\partial p)$ is the gradient or Jacobian and $(\partial^2 I/\partial p^2)$ is the Hessian.
Considering just the x-coordinate, the iterative expression is given by

$$x_{m+1} = x_m - \delta p_x \tag{2.16}$$

Similar expressions are obtained for the other parameters: A_d, y, σ_x, σ_y.

The time consumed by the method will mainly depend on the number of fitting parameters employed. A better fitting is possible if a larger number of parameters are used. However, it might increase the time consumed by the method. In our case, we decided to use just four parameters. These corresponded to the (x_d, y_d) coordinates, one Gaussian width σ_d ($\sigma_x = \sigma_y$) and the amplitude A_d.

The values obtained for each element of δp, will give the step size and direction of movement. As the starting point in this case is given by (x_{COG}, y_{COG}), we will move away or towards these values depending on the sign obtained for δp_x, δp_y and how close or far away we need to locate the next centroid position will depends on its values. The method stops when δp values are zero, so no increment/decrement is necessary to move to the next centroid position or when δp takes a value that we define as the method accuracy (e.g. 0.5 pixels).

Figure 2.2 illustrates the roles that the gradient and curvature (Hessian) play in reaching the optimum value using this method in a more general manner. As stated before, the objective is to find the $p*$ that maximizes the cost function $I(p)$. This can be done moving upwards along the function surface until no more additional increments are needed. To begin, it is necessary to initialise the method using initial values for the parameters p_0. At each iteration or step, we will move towards a new value p that will be higher than the previous one. Then, the size of the step and direction will depend on the curvature and the slope value. In Figure 2.2 (B) the slope is positive, then, it is necessary to increase the step value. In plot (C) the slope is negative, but the curvature is concave, then in this case, we need to move back, reducing the value of p for the next iteration. The opposite will need to occur if the function is convex, moving forward if the slope is negative and backwards if it is positive. The size of the step is represented in (D) and (E). If the curvature is big, the step size

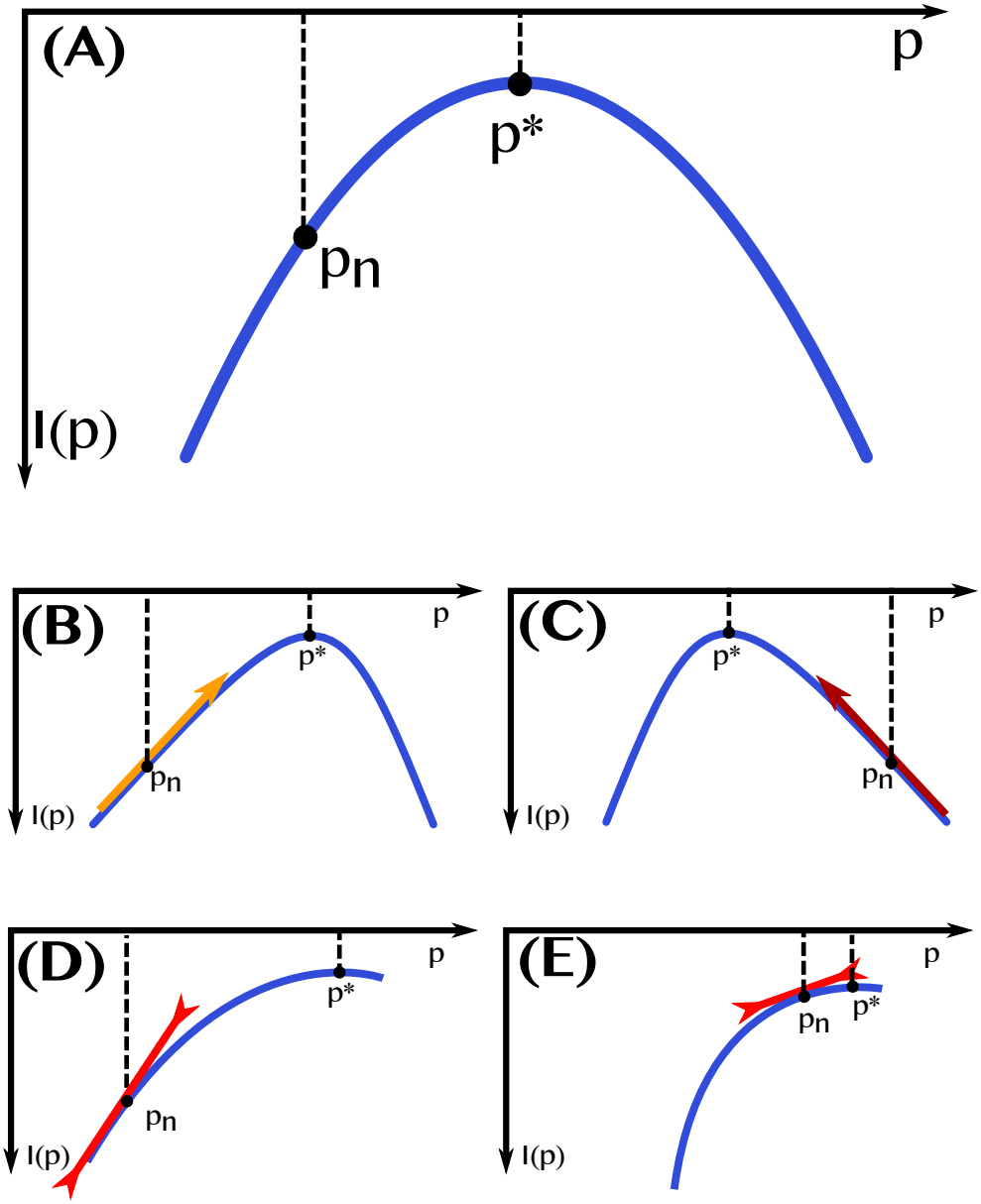


Figure 2.2: Plots to understand how the gradient (Jacobian) and Hessian are involved in the determination of the next value in our iterative process. The objective is to find $p*$ that maximizes the cost function $I(p)$. Basically this can be done moving upwards the function surface until no more additional increments are needed (A). Plots (B) and (C) are related to the Hessian or direction to follow in the next iteration. Plots (D) and (E) are related to the gradient or size of the step in the next iteration. Small steps are required in order to converge to an optimum value without overshooting, on the other hand, big values are required to achieve convergence in short time, particularly when the initial values are not too close to the optimum value.

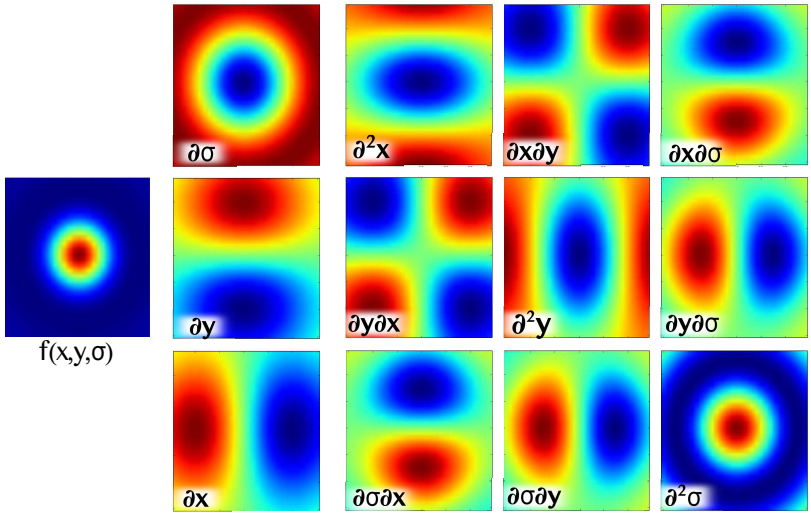


Figure 2.3: Following a Gaussian model $f(x, y, \sigma)$, masks are generated for the first and second derivatives of x, y and σ.

required should be small. The purpose of this is to converge to an optimum value without overshooting. The opposite will occurs if the curvature is small - then bigger steps will be required to minimize the number of steps (and hence time taken) to reach the optimum value.

From the expressions obtained above, it is necessary to calculate the gradient and second Hessian of the cost function with respect to all the parameters being employed. The derivatives were performed over the model function, as we kept the data parameters fixed. Images of the model mask and its derivatives are presented in Figure 2.3.

An important required parameter is the initial guess for each parameter. These values are employed to generate the model masks. For the method to work and converge to a solution, it is necessary to use values as close as possible to the expected ones. To test the method's ability to find the right coordinates, we first employed as initial guess the values obtained from the centre of gravity method $(x_{\mathrm{CoG}}, y_{\mathrm{CoG}})$.

The whole process is presented schematically in Figure 2.4. The process started with generating random datasets with different known positions and noise. These datasets were passed through the first centroid method (the centre of gravity) and an estimated value for the spot position is obtained. The gradient and the Hessian are computed using as initial parameters $p_0 = (x_{\mathrm{CoG}}, y_{\mathrm{CoG}}, \sigma)$ as the initial guesses. With these masks and the data image,

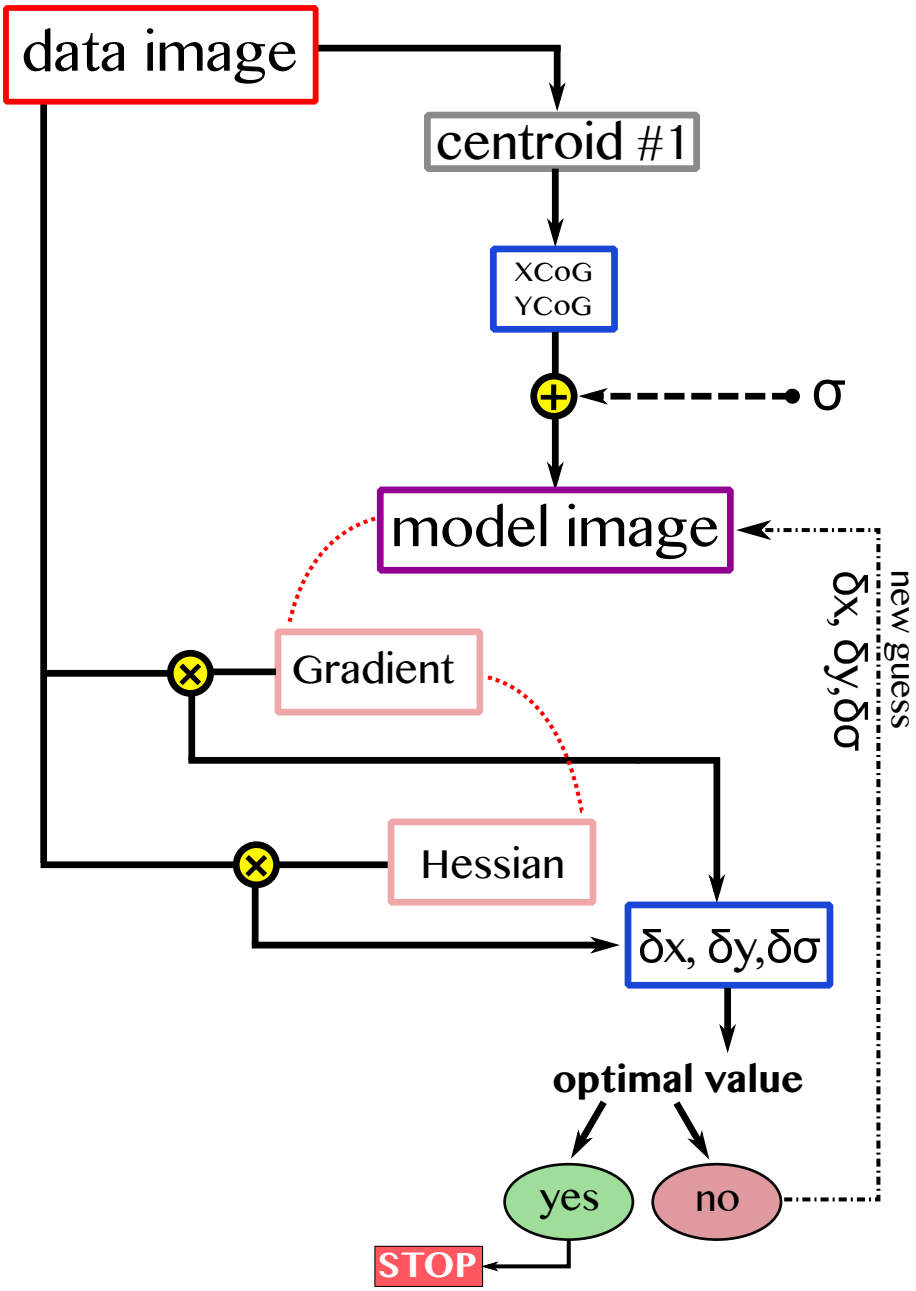


Figure 2.4: Graphical representation of how the centroid algorithm that we present is carried out. Using a data image, the CoG centroid coordinates are obtained and from this, we generate a Gaussian masks using $(x_{\mathrm{CoG}}, y_{\mathrm{CoG}})$ as initial parameters. The whole process will stop once the optimal value has been achieved.

values for δx, δy, $\delta\sigma$ are obtained and used to calculate the next value for the corresponding parameter (expression 2.16).

Figure 2.5, shows the results obtained when one spot with a known coordinate position was modelled using different SNRs. The signal-to-noise ratio in our case was defined as the ratio between the root-mean squared values of the amplitudes obtained for the signal and the noise that were generated. For this, a Gaussian spot was generated with fixed position (x, y) and width σ values. Noise was also modelled to be added to the Gaussian spot. The CoG was calculated for each case (10 different SNR values) and these values were employed as initial guesses for our model mask. From this Figure, we can notice that the higher the noise introduced to the image, the lower the performance of the CoG method.

Figure 2.6, shows the values obtained for the X-Y coordinates using both the CoG and Gaussian method when 30 realisations for a spot with known coordinates position were modelled under a SNR = 10. In both cases, the values obtained using Gaussian method are closer to the original values, both curves are almost overlapped along all the iterations. Something different occurs with the values obtained with the CoG method, where an offset or bias can be clearly observed.

To show the performances of the two methods, CoG and Gaussian, when averaged over many realisations, tables 2.1 and 2.2 are presented. The first table corresponds to 100 realisations and the second corresponds to 500 iterations. In both cases, different SNR were employed to test the performance of each method. From there, as the SNR decreases, the values obtained for the X-Y coordinates using the CoG method start to increase compared to the original values. At SNR = 10, the difference between the original values and the obtained with the CoG method can be as big as $\sim$10%. This increase in value is due to the noise present in the measurements that will introduce an offset or bias in the values obtained. On the other hand, the behaviour for the Gaussian method is different, as the values obtained for the coordinate are quite close to the actual values, no matter the SNR employed.

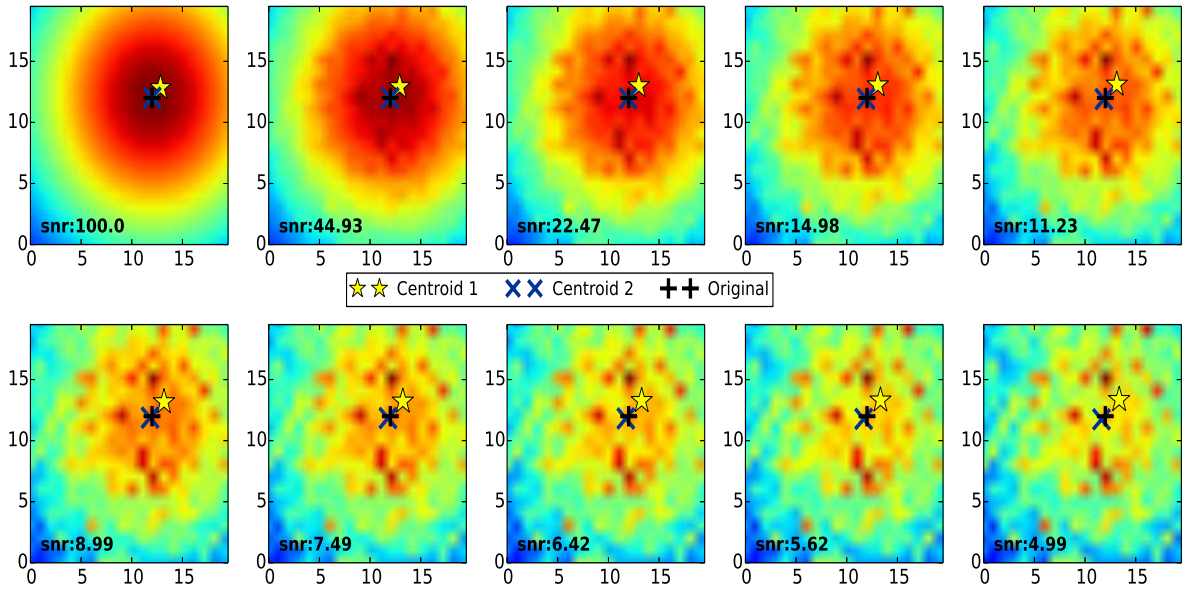


Figure 2.5: Results obtained when one spot with a known coordinate position was modelled under different SNR. Centroid 1 ("$\star$") represents the simple centroid algorithm (CoG) and centroid 2 ("$\times$") is the algorithm that we proposed. The original coordinate values are represented by "+". Important to notice that at low SNR, the values obtained with our method are closer to the original values compared with those obtained using the CoG method.

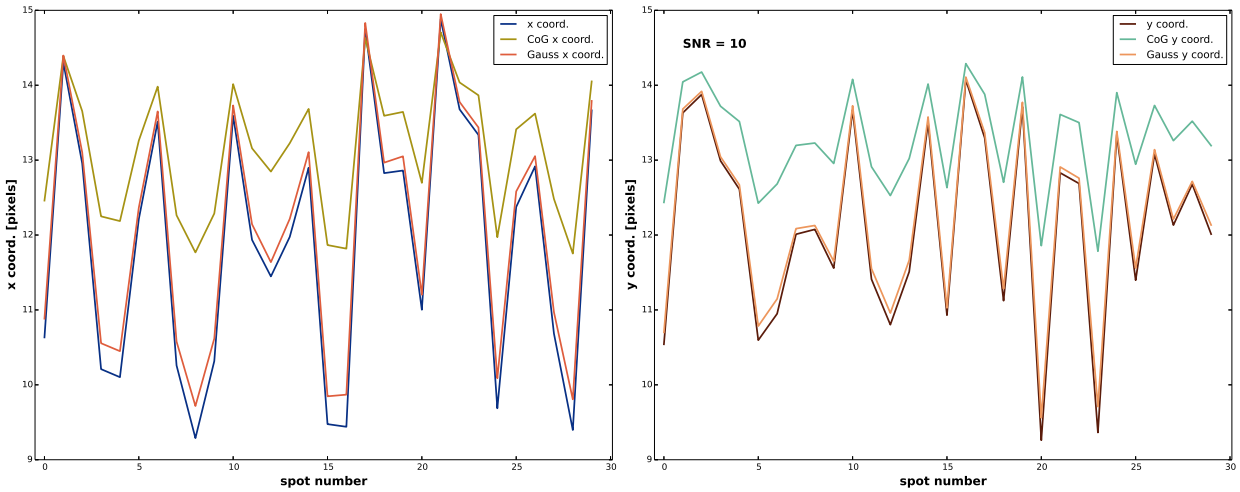


Figure 2.6: Results obtained when 30 realisations for a spot with known coordinates position were modelled under a SNR = 10. In both cases, the values obtained using the method that we proposed are closer to the original values. Gaussian and original coordinates values are almost overlapped along the 30 iterations compared with the traditional centre of gravity method, where an offset or bias can be observed. **Left-hand side:** X coordinates. **Right-hand side:** Y coordinates.

This is also shown in Figure 2.7. In this case, both x and y coordinates are plotted only for datasets with low SNR values. A small bias is seen in the centroid values obtained when the CoG centroid method is employed for cases with low SNR. On the other hand, the Gaussian mask method performs much better than CoG at lower SNR values.

The number of iterations required to reach an optimal solution was also considered. Figure 2.8, shows spots where some random jitter of the spot centre was introduced, this at different signal-to-noise ratio values. Over each spot, the CoG coordinate values were obtained and also the values obtained iteratively with the Gaussian process. In this case, the initial guess used to generate the Gaussian masks were the coordinates obtained with the CoG method. After the first iteration, the values obtained by the Gaussian method were employed as the initial parameters for the second set of Gaussian masks and so on.

From Figure 2.9, the spot coordinate values versus the number of iterations carried out are presented for a SNR of approximately 4. The original coordinate value is shown, along with the CoG and the Gaussian values. Once again, at low SNR, the value obtained with our method is closer to the actual value compared with the centre of gravity method. As the

100 realisations					
SNR	**variable**	**mean μ**	**var σ^2**	**std σ**	**Δ%**
100	X	12.16	2.33	1.53	-
	Y	11.97	2.21	1.49	-
	CoG X	12.95	1.02	1.01	6.45
	CoG Y	12.82	0.96	0.98	7.12
	Gauss X	12.22	2.11	1.45	0.46
	Gauss Y	12.03	1.93	1.39	0.55
40	CoG X	13.04	0.9	0.95	7.19
	CoG Y	12.91	0.84	0.92	7.90
	Gauss X	12.24	2.11	1.45	0.61
	Gauss Y	12.02	1.94	1.39	0.31
20	CoG X	13.12	0.8	0.9	7.85
	CoG Y	12.99	0.75	0.86	8.60
	Gauss X	12.25	2.11	1.45	0.77
	Gauss Y	11.97	1.94	1.39	0.06
10	CoG X	13.25	0.65	0.81	8.97
	CoG Y	13.14	0.6	0.77	9.77
	Gauss X	12.29	2.12	1.45	1.08
	Gauss Y	11.91	1.96	1.4	0.44

Table 2.1: 100 realisations at different SNR. Δ% corresponds to the difference in percentage between the original value and the value obtained with the CoG or the Gaussian method. The difference between values is smaller for the Gaussian method compared to the CoG, where a difference up to $\sim$9.8% can be achieved at low SNR. As the SNR starts to decrease, the values obtained for the X-Y coordinates start to increase when the CoG method is employed.

500 realisations					
SNR	**variable**	**mean μ**	**var σ^2**	**std σ**	**Δ%**
100	X	12.08	2.36	1.53	-
	Y	12.05	2.36	1.54	-
	CoG X	12.89	1.03	1.02	6.73
	CoG Y	12.87	1.03	1.01	6.82
	Gauss X	12.14	2.13	1.46	0.50
	Gauss Y	12.11	2.09	1.45	0.53
40	CoG X	12.99	0.9	0.95	7.56
	CoG Y	12.97	0.9	0.95	7.64
	Gauss X	12.16	2.11	1.45	0.67
	Gauss Y	12.08	2.08	1.44	0.26
20	CoG X	13.08	0.8	0.99	8.31
	CoG Y	13.06	0.8	0.89	8.25
	Gauss X	12.08	2.09	1.45	0.84
	Gauss Y	12.05	2.06	1.44	0.01
10	CoG X	13.23	0.64	0.8	9.57
	CoG Y	13.2	0.64	0.8	9.56
	Gauss X	12.22	2.06	1.44	1.16
	Gauss Y	11.98	2.04	1.43	0.59

Table 2.2: 500 realisations at different SNR. Δ% corresponds to the difference in percentage between the original value and the value obtained with the CoG or the Gaussian method. The difference between values is smaller for the Gaussian method compared to the CoG, especially at high SNR. A big difference, up to a $\sim$9.6% can be achieved at low SNR, when the coordinates are obtained using the CoG method.

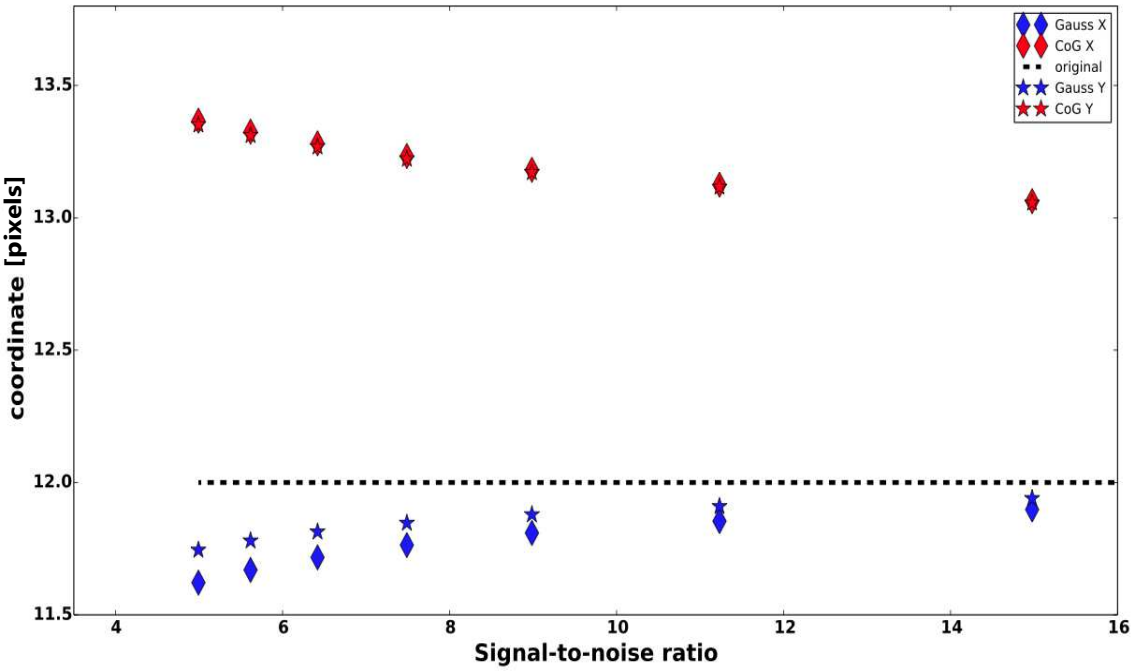


Figure 2.7: Spot position (x, y) obtained using the CoG and the proposed hybrid method for cases of low SNR values. Original spot position is represented by the dashed black line. A considerable amount of bias can be observed in the centroid values obtained with the CoG method.

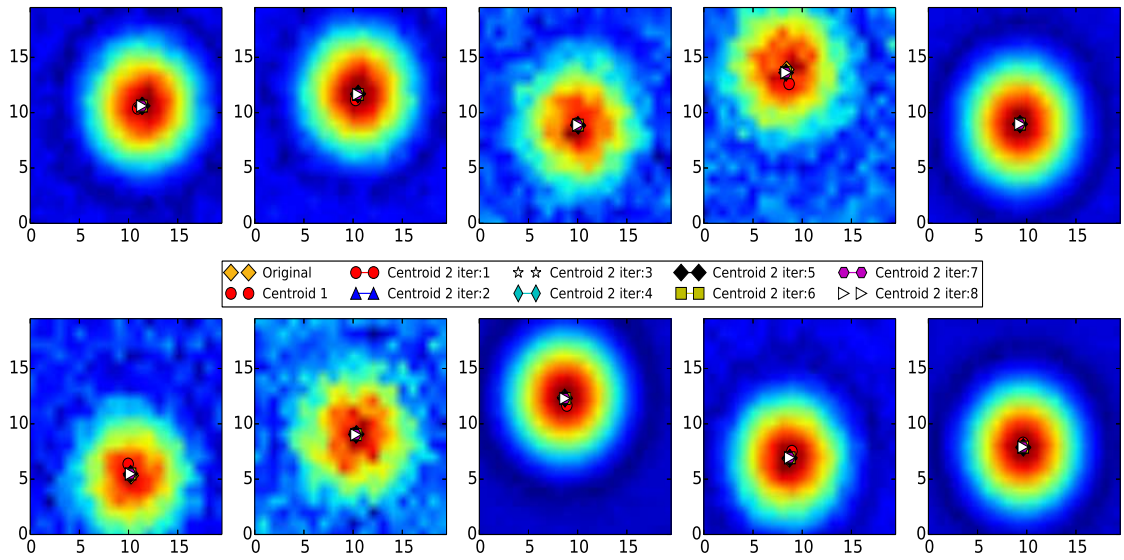


Figure 2.8: Different spots with different SNR values. Over each spot, the CoG (centroid 1) coordinate values and the Gaussian values were calculated. The Gaussian process was repeated 8 times in order to test the method convergence. The initial guess used to generate the Gaussian masks were the coordinates obtained with the CoG. After the first iteration, the values calculated by the Gaussian method were employed to generate the subsequent masks.

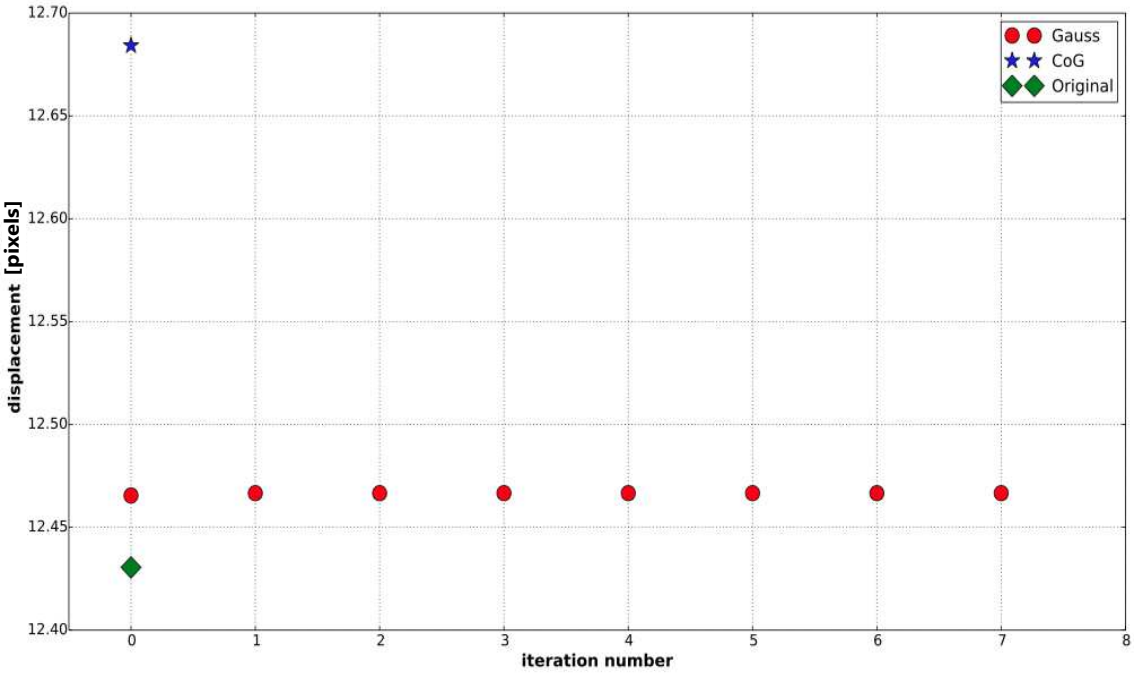


Figure 2.9: Spot coordinate values versus the number of iteration carried out are presented for a SNR approximated of 4.

number of iteration increases, no large changes in the values obtained can be seen, meaning that the method has converged. Thus, the spot coordinate values can be obtained within only one or two iterations. Then, the method requires only a few iterations to achieve convergence, showing its efficiency. Small variations in the values obtained for the spot centroid coordinates can be due to variations in the initial guess parameters. As mentioned above, the first iteration was always performed using the CoG values as an initial guess. Thus, if these values are somehow improved (CoG values), we could expect that the number of iterations required to reach the optimal centroid value will be reduced.

We also tested the method under more realistic conditions, this was done by recording different images of the Shack-Hartmann spots. These images were obtained at different exposure times and different laser intensities using different samples (biological and non-biological). In Figure 2.10, some exemplar SH spots are presented. In this case, spots located at different parts of the system pupil were used and the spot position were calculated using both methods, CoG and Gaussian masks. By using real data, some differences arise given that we work now with a large image that contains many spots, rather than one

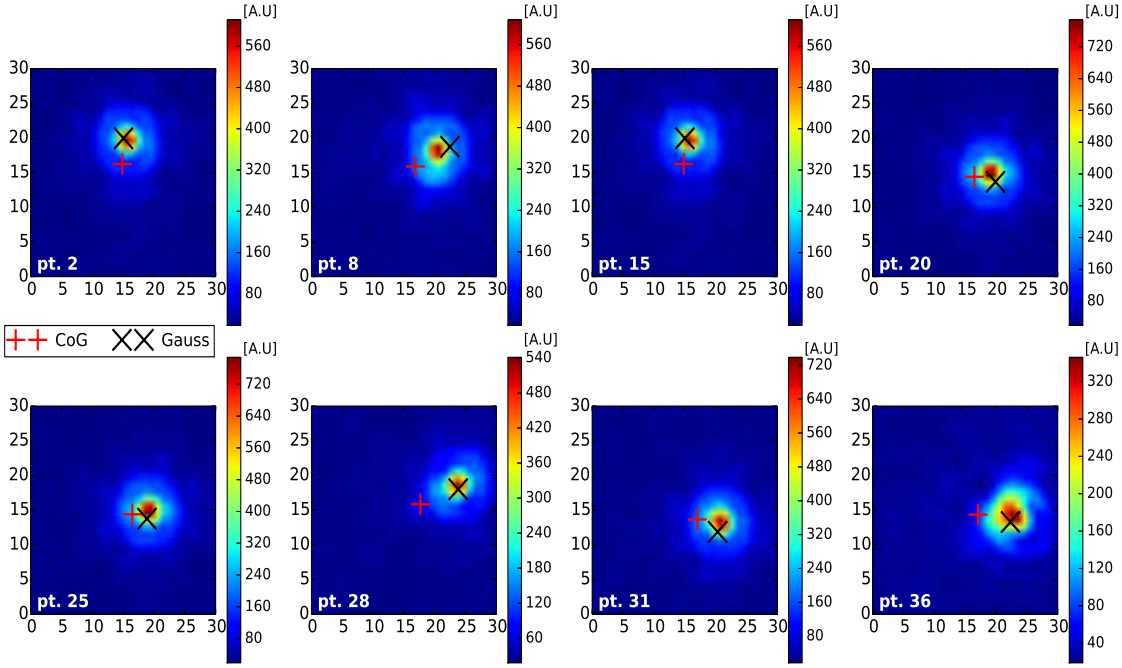


Figure 2.10: Results obtained when real data obtained with the SHWFS. Spot coordinates obtained using the CoG method and the Gaussian method are plotted.

image with one spot. Then, some changes were made to our method (Figure 2.4) to allow its implementation in our system, these changes are schematically represented in Figure 2.11. In this case we did not take as initial guess the values obtained from CoG. Now, we generated only one set of fixed masks that were used for every single spot. These general masks were built by setting the spot coordinates at (0.0, 0.0) and a fixed value for A and σ. The reason to use only one set of fix masks is based in that the spots centroid positions should not change in a big amount from frame to frame as we work in a closed-loop configuration. It also reduces significantly the computational time as a mask generated just once is employed over the whole image, compared to the use of a new mask for every single spot.

The time required to perform the centroid calculation using one iteration was faster compared with the fitting function methods found in Python. Fitting functions had times ranging between 500µs to 1s for one spot, meanwhile the Gaussian method registered times up to 150µs or less for the whole Shack-Hartmann image. Results from operation in a closed-loop configuration using the centroid algorithm presented here are shown in Chapter 4.

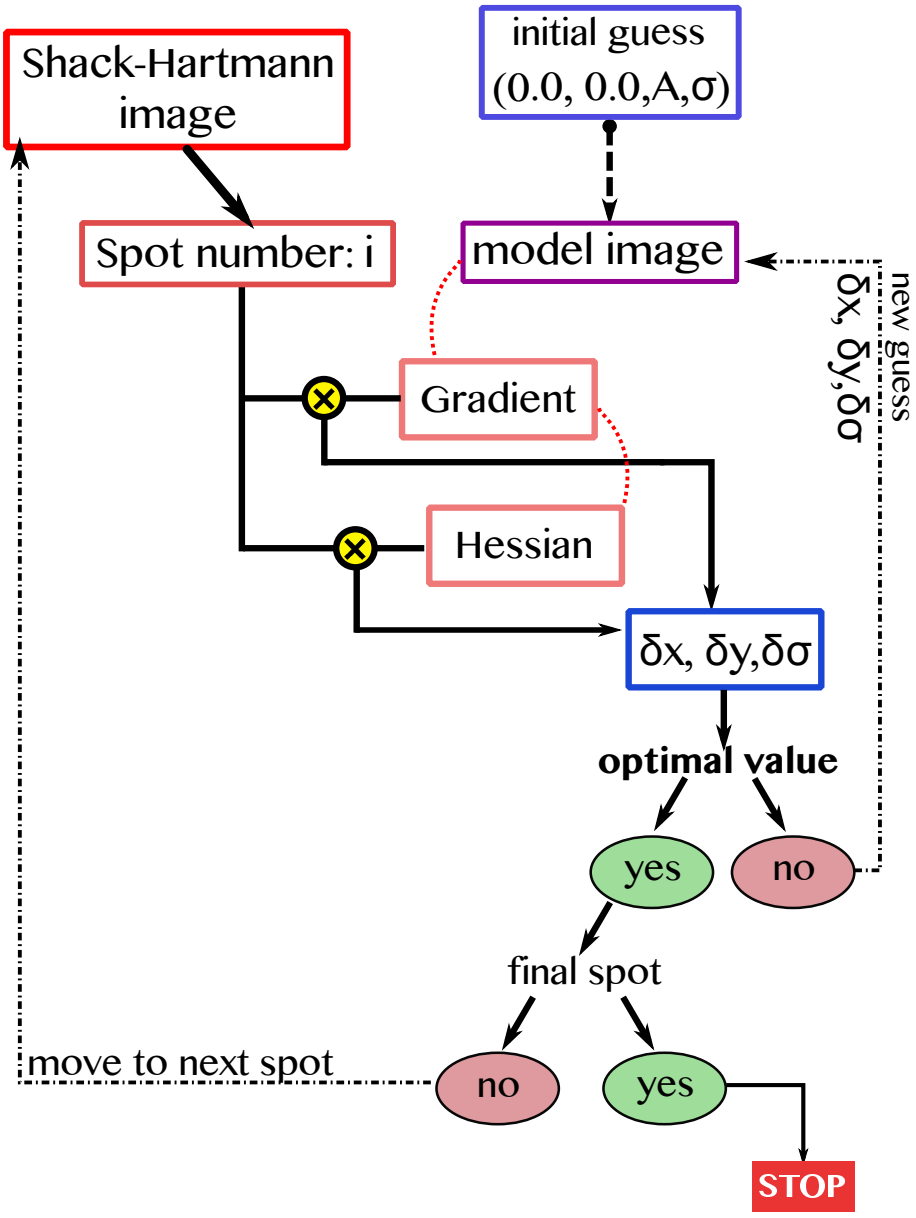


Figure 2.11: Graphical representation of how the centroid algorithm that we present is carried out when using images obtained from the SHWFS. The masks to be employed are generated only one time, with initial values $(0.0, 0.0, \sigma)$ and are applied to every single spot.

2.3 Conclusions

The method that we proposed was based on a hybrid between a matched filter and a quasi-Newtonian optimization algorithm. The product between a reference image or model (Gaussian mask) and the actual data was used as the cost function to be optimised. Optimisation was achieved by following the quasi-Newtonian method that involves a Taylor expansion of this cost function around an initial value close to the optimal value. As the expanded cost function does not correspond to a quadratic function, an iterative solution is required. The use of the first and second derivatives of this expansion play the main role in calculating the next iteration value. From the results presented in this chapter, it can be seen that our method achieves better values than the CoG for both simulated and real scenarios. In order to achieve convergence and arrive at an optimal value, an initial guess need to be supplied. When data was simulated, simple centre of gravity results were employed as the initial guesses. Even though sometimes the values obtained with CoG were not the best values to be introduced as initial guesses, as they were biased toward the image geometrical centre, good results were obtained. This can be seen on the results presented before in Figure 2.7. To overcome the problem associated with possible convergence errors due to unreasonable initial parameters, a second algorithm implementation was devised (Figure 2.11). This second implementation avoided the use of the values obtained from the CoG approach, which could lead to erroneous values due to bias. This was implemented when real data obtained from the Shack-Hartmann sensor was employed. Good results were obtained in this case, particularly considering that symmetric spots were assumed all the time.

The method that we presented and implemented could be considered the simplest version of this approach, as we assumed symmetric spots. More parameters could be included,such as different values for the Gaussian width in each orthogonal direction ($\sigma_x \neq \sigma_y$) and rotation angle, and this might achieve better centroid values. However, this may increase the time required per calculation reducing the ability of this method to be implemented on live systems.

Chapter 3

Wavefront reconstruction

Together with the wavefront sensing stage, another important and critical function in most AO systems is the wavefront reconstruction process. This involves a large amount of data processing that must be carried out in real time. Here, we present the problems associated with wavefront reconstruction using data obtained from a SHWFS. A brief summary of the techniques already implemented and the problems associated with them is also presented.

The performance of adaptive optics systems is often limited by the accuracy of the wavefront measurement. This accuracy is limited by photon (and sometimes electronic) noise, the finite sampling of the wavefront, the sensor and any assumptions of prior information employed in the wavefront reconstruction. In astronomical adaptive optics, there are good models for these prior statistics, such as the Kolmogorov turbulence model (Roggemann et al. (1996)), that can be used in the wavefront reconstruction. However, in microscopy for example, good prior statistical models are not always known. In this chapter, we investigate the effect of using different prior information models in an optimal reconstructor for cases where the assumed model differs from the actual wavefront statistics.

3.1 The principle of wavefront reconstruction

The reconstruction process is a necessary step to obtain the phase profile estimates from certain types of sensors, such as a shearing interferometer or a Shack-Hartmann sensor. The reconstruction problem was first addressed by (Rimmer (1974)) to evaluate lateral shearing interferograms obtained from wavefronts of arbitrary shape. The general problem is the determination of the wavefront phase from a set of discrete phase slope measurements. It

involves the calculation of a surface by an integration-like algorithm.

Different approaches have been proposed to accomplish this phase reconstruction stage. Each estimation approach studied may be classified as being either zonal or modal (Tyson (2010)). In the zonal methods, the phase is determined on a discrete set of points that are distributed over the sensor aperture. For the modal method, the phase is represented by the coefficients of an expansion in a set of basis functions, generally called modes. In both cases, least-square estimation can be employed to perform the phase reconstruction.

The difference between methods to reconstruct the phase is generally based on the different models that can be used to fit the local slope measurements. To select a particular model, different variables need to be considered such as, compatibility, complexity and error propagation. Compatibility is associated with the sensor geometry of the slopes measurements, complexity is related to numerical convergence, storage and computational speed. Finally, error propagation is related to the effect that noise in the slope measurements has over the reconstructed phase.

In the literature, a phase difference slope model for the case of zonal reconstruction is commonly employed (Hardy (1998)). This can be applicable to a shearing interferometer or to a Shack-Hartmann wavefront sensor, all based on whether the x-slope measurements coincide with the y-slope measurements. Three grid configurations are presented in Figure 3.1, which illustrate the positions for the x and y slopes measurements together with the points where the phase is reconstructed (Southwell (1980)). It is important to highlight that the reconstruction problem mainly depends on the geometry employed, which depends on where the actual slope measurements are being sensed.

The grid pattern presented by (Fried (1977)) is shown on the left-hand side of Figure 3.1. In this case we have coincident x-y slopes, but with a displaced phase grid represented by the blue spots. The pattern presented in the middle of the figure corresponds to the geometry studied by (Hudgin (1977)), where a square array of phase points can be connected by the values obtained by x or y-slope differences. The final pattern shown in Figure 3.1, corresponds to the geometry presented by (Southwell (1980)), where the slope measurements are coincident with the phase points. For each grid pattern, different expressions that relate the slope measurements with the phase points are obtained. These are summarized in Table 3.1, where s_{ij}^x and s_{ij}^y represent the slopes along x and y directions for a subperture (i, j) of

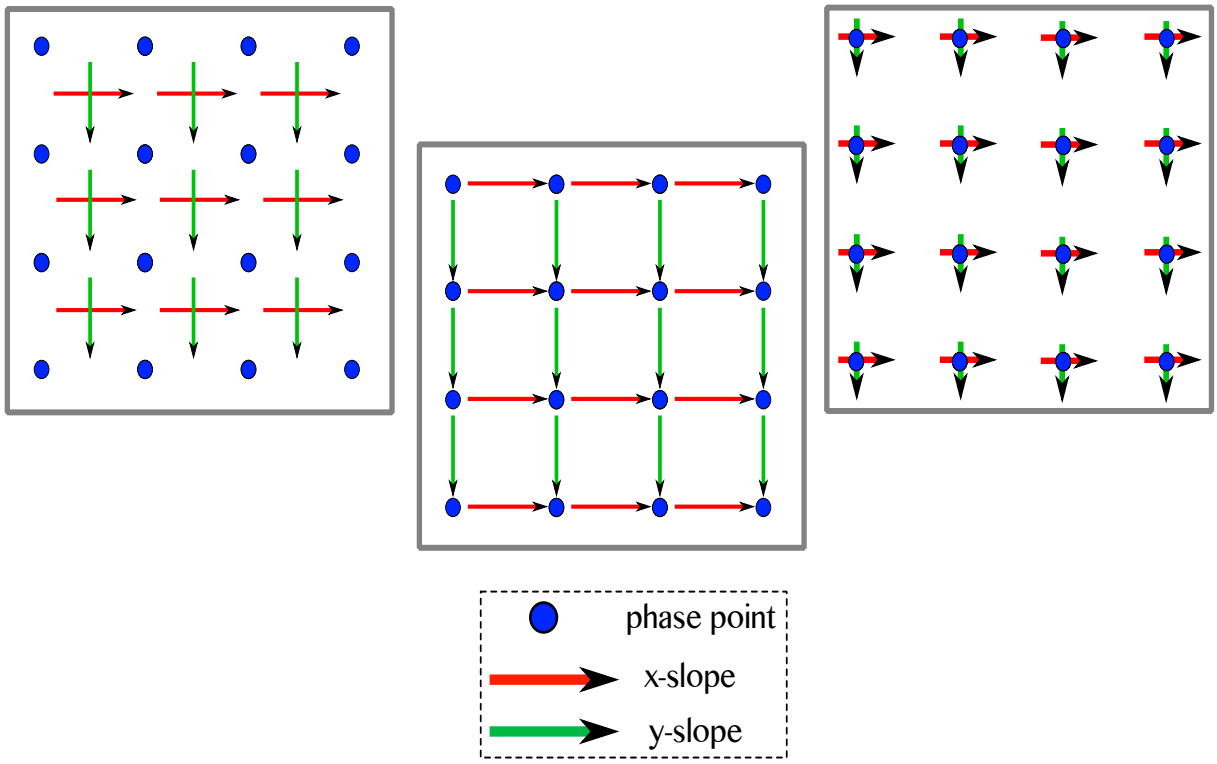


Figure 3.1: Three different slope measurement sampling geometries and phase points employed in zonal reconstruction. **Left-hand side:** configuration presented by Fried. **Centre:** configuration presented by Hudgin. Right-hand side: configuration presented by Southwell.

side d. The reconstructed phase for subaperture (i, j) is represented by ϕ_{ij}. The derivations of the expressions presented in Table 3.1 are not addressed here, but they are described in detail in the literature (Fried (1977); Hudgin (1977); Southwell (1980)).

The reconstruction problem can be expressed in a matrix framework (Hunt (1979)), which is based on the expressions presented in Table 3.1. In this case, the unknowns are contained in a vector $\boldsymbol{\phi}$ of N phase values distributed over the grid. These values are calculated from the data, a vector containing the slope measurements $\mathbf{s}$ of M elements in both directions. It is possible to write the following linear relation:

$$\mathbf{s} = \mathbf{A}\boldsymbol{\phi} \tag{3.1}$$

where $\mathbf{A}$ corresponds to a matrix of $N \times M$ elements.

Geometry and slope-phase conversion		
Fried	$s^x_{ij} = \frac{[(\phi_{i+1,j}+\phi_{i+1,j+1})/2-(\phi_{i,j}+\phi_{i,j+1})/2]}{d}$	$s^y_{ij} = \frac{[(\phi_{i,j+1}+\phi_{i+1,j+1})/2-(\phi_{i,j}+\phi_{i+1,j})/2]}{d}$
Hudgin	$\frac{s^x_{i+1,j}+S^x_{ij}}{2} = \frac{(\phi_{i+1,j}-\phi_{ij})}{d}$ with $i = 1, N-1$ and $j = 1, N$	$\frac{s^x_{i+1,j}+S^y_{ij}}{2} = \frac{(\phi_{i+1,j}-\phi_{ij})}{d}$ with $i = 1, N$ and $j = 1, N-1$
Southwell	$s^x_{ij} = \frac{(\phi_{i+1,j}-\phi_{ij})}{d}$ with $i = 1, N-1$ and $j = 1, N$	$s^y_{ij} = \frac{(\phi_{i,j+1}-\phi_{ij})}{d}$ with $i = 1, N$ and $j = 1, N-1$

Table 3.1: Expressions that relate the slope measurements s^x_{ij} and s^y_{ij} for a subperture (i, j) of side d with the phase points for: Fried, Hudgin and Southwell grid patterns.

To derive the matrix $\mathbf{A}$, and based on the fact that there are more slope measurement points (s^x_{ij},s^y_{ij}) than points at which the phase (ϕ_{ij}) needs to be estimated, a least-square error estimation procedure is generally employed.

The least-squares approach is a technique that consists of the minimization of the error ϵ_s of the measurements. This error is given by

$$\epsilon_s = \|\mathbf{s} - \mathbf{A}\boldsymbol{\phi}\|^2 \tag{3.2}$$

where $\|\|$ corresponds to the norm of a vector. The phase $\boldsymbol{\phi}$ is obtained so that it will minimise the error ϵ_s. Then the least-square solution is given by

$$(\mathbf{A}^{\mathrm{t}}\mathbf{A})\boldsymbol{\phi} = \mathbf{A}^{\mathrm{t}}\mathbf{s} \tag{3.3}$$

where $\mathbf{A}^{\mathrm{t}}$ is the transpose of $\mathbf{A}$. The standard singular value decomposition (SVD) solution cannot be employed in this case as generally the matrix $\mathbf{A}^{\mathrm{t}}\mathbf{A}$ is singular. To solve this problem, different iterative methods have been proposed and studied (Fried (1977); Hudgin (1977); Southwell (1980)). A good method to solve this problem was proposed by (Herrmann (1980)), this corresponds to a minimum norm with a zero mean solution. This zero mean solution results in non-singular matrices.

In the modal method, we assume that the wavefront phase at the sensor pupil can be

represented by an infinite sum expansion of orthogonal functions. Considering that we have the same set of slope measurements shown in Figure 3.1, we use these measurements now to fit the coefficients in a phase expansion

$$\boldsymbol{\phi} = \sum_{k=0}^{M} a_k F_k(x, y) \tag{3.4}$$

where a_k are the coefficients to be determined and F_k corresponds to two-dimensional functions that are orthogonal over the discrete sampled aperture where we want to determine the phase. In this case, we assumed that the functions are normalized. Different set of basis can be selected, such as Zernike polynomials, Karhunen-Loève (Roddier (1999); Wang & Markey (1978); Roddier (1990)) or Legendre polynomials (Cubalchini (1979)). If we work with Zernike polynomials to expand the phase, then the slope model is obtained using the expressions:

$$s^x = \sum_{k=1}^{M} a_k \frac{\partial F_k}{\partial x} \tag{3.5}$$

$$s^y = \sum_{k=1}^{M} a_k \frac{\partial F_k}{\partial y} \tag{3.6}$$

where we discarded the piston term ($k = 0$) from the basis expansion. As all the other terms in the expansion have zero mean, then so will $\boldsymbol{\phi}$. This assures that the obtained solution will be the minimum norm. Also, in modal reconstruction, we are able to select the number of coefficients to be estimated (M), greatly reducing the numerical complexity of the estimation process. In our case, 100 coefficients were employed to describe the wavefront. The selection for the number of modes employed has to do with trying to avoid overfitting or underfitting the data. Both situations can lead to poor system performance (Lee et al. (2006)).

Writing expression 3.6 in a matrix form

$$\mathbf{s} = \mathbf{A}\mathbf{a} \tag{3.7}$$

where $\mathbf{A}$ corresponds to a rectangular matrix with M columns but with variable number of rows, depending on the grid pattern employed (Figure 3.1:Fried, Hudgin or Southwell).

At this point and in a similar fashion to zonal reconstruction, the solution can be found

using least-square estimation, given by

$$\mathbf{A}^{\mathrm{t}}\mathbf{A}\mathbf{a} = \mathbf{A}^{\mathrm{t}}\mathbf{s} \tag{3.8}$$

$$\mathbf{a} = (\mathbf{A}^{\mathrm{t}}\mathbf{A})^{-1}\mathbf{A}^{\mathrm{t}}\mathbf{s} \tag{3.9}$$

where $\mathbf{a}$ corresponds to the coefficients of the polynomial expansion that represents the phase over the sensor aperture.

It is important to note that there are two important sources of error in the reconstruction process, independent of whether we use the zonal or the modal approach. One of the sources of error corresponds to the algorithm accuracy, this means how well the least-square process is able to reconstruct the phase of an arbitrary shape. The answer to this question mainly depends on the shape of the wavefront being measured. For the case of zonal reconstruction, accurate reconstruction was achieved by (Southwell (1980)) when wavefronts having any combination of tip, tilt, defocus and some astigmatism were employed. However, for wavefronts with higher-order aberrations, the zonal model does not achieve perfect reconstruction, as a consequence of the finite grid sampling density. For the modal approach this does not represent a considerable source of error.

The second source of error in the reconstruction process is related to the noise in the slope measurements. Zonal and modal error noise propagation properties have been studied (Law & Lane (1996)), in order to determine the uncertainty resulting from errors in the slope measurements. Once again, this error will depend on the geometry employed and will be different for both cases (Fried (1977); Hudgin (1977); Southwell (1980); Hunt (1979); Cubalchini (1979); Herrmann (1980); Diaz-Santana et al. (2005)).

3.2 Optimal reconstructor and Prior knowledge

Wavefront reconstruction can be rigorously studied within the formalism of linear inverse problems. In this case the basic relationship between slope measurements $\mathbf{s}$ and the unknowns $\boldsymbol{\phi}$ can be expressed by

$$\mathbf{s} = \mathbf{A}\boldsymbol{\phi} + \mathbf{n} \tag{3.10}$$

where $\mathbf{n}$ is a vector with zero mean that represents the noise. Thus, the reconstruction problem can be understood as follows: given a set of slope measurements represented by $\mathbf{s}$, we need to estimate the unknown phase points $\boldsymbol{\phi}$.

When the reconstruction problem is considered an inverse problem, the noise can be assumed to be uncorrelated with the phase unknowns and to follow Gaussian statistics (as a combination between electric noise and background photon noise) (Hardy (1998); Noll (1976); Wang & Markey (1978)). For practical systems, the noise statistics can be quantified directly from the data. Also, the statistics of the phase vector $\boldsymbol{\phi}$, can be quantified theoretically or it could be determined experimentally, all of this based on the well-known turbulence model and its properties (Hickson (2014)).

In order to obtain the best phase estimation, it is possible to work out the inverse problem by solving it using for example the maximum likelihood technique and the maximum a posteriori technique (Sasiela & Mooney (1986); Bakut et al. (1994)) or Bayesian inference approach (Box & Tiao (1973)).

The maximum likelihood technique tries to determine the set of unknowns parameters, in our case $\boldsymbol{\phi}$, that will maximise the probability of producing the set of measurements $\mathbf{s}$. In order to follow this approach, a function called the likelihood function is represented by a probability function ($P(\mathbf{s}|\boldsymbol{\phi})$), which depends on the measurements $\mathbf{s}$ and the phase $\boldsymbol{\phi}$. On the other hand, the maximum a posteriori techniques consist in the determination of the unknowns $\boldsymbol{\phi}$ that will maximises the a posteriori probability of the unknowns ($P(\boldsymbol{\phi}|\mathbf{s})$). To evaluate this function we require the data and more importantly, some a priori knowledge about the unknowns.

Bayesian inference offers an alternative to Maximum Likelihood and allows us to determine the probability of the parameters given the data, something that is not possible to do with maximum likelihood. Bayesian inference assumes that the distribution parameters are random variables. Existing knowledge about these parameters is expressed in the form of a prior distribution; this existing knowledge is then combined with information from newly observed data to give a posterior distribution. In contrast, maximum likelihood estimation only gives the values of the parameter which fits the data best. However, having a prior distribution for the parameters in Bayesian inference implies there is some prior knowledge about the value of these parameters, which in many cases is not true.

Basic Idea behind Bayesian inference

Lets suppose we have a set of observations or measured data, $\boldsymbol{s}$, which are drawn from a probability density function with parameters $\boldsymbol{\phi} = (\phi_1, \phi_2, \ldots, \phi_k)$ whose exact values are not known, however its form or distribution is known. The Bayesian approach assumes that the prior knowledge of $\boldsymbol{\phi}$ can be described by a prior probability distribution, $P(\boldsymbol{\phi})$. Then considering the measured data, $\boldsymbol{s}$, the idea about the values that the parameters can take can be updated to give a posterior distribution, $P(\boldsymbol{\phi} \mid \boldsymbol{s})$. This posterior distribution can be obtained by using Bayes theorem:

$$P(\boldsymbol{\phi} \mid \boldsymbol{s}) = \frac{P(\boldsymbol{s} \mid \boldsymbol{\phi})P(\boldsymbol{\phi})}{P(\boldsymbol{s})}$$

This expression is called Bayes's Rule and corresponds to the most general form, where $\boldsymbol{s}$ and $\boldsymbol{\phi}$ represent the measured data and the parameters to be estimated. In this form, Bayes's Rule states that the probability of event $\boldsymbol{\phi}$ given the occurrence of event $\boldsymbol{s}$ is equal to the probability of event $\boldsymbol{s}$ given that event $\boldsymbol{\phi}$ has occurred times the probability of event $\boldsymbol{\phi}$ occurring, divided by the probability of events occurring.

The main difference between the use of the maximum likelihood method and the Bayesian inference is based on that the ML method will return an optimal value for the model parameters, while the Bayesian approach will fits a distribution to the parameters.

Prior Distributions

It is important to make an appropriate choice for the prior distribution. The prior must contain any idea about the problem that is being modelled. Particularly when some sources of uncertainties are introduced, affecting the values obtained for the parameters to be estimated. In this case, the prior selection should take this problem into account. Prior information or prior distributions measure the relative strength of possible ideas for the possible values of the parameters to be estimated. The prior information can be of two general forms:

- *Uninformative or flat priors*: In many cases, we have no idea or only a vague idea of the values that the parameters to be estimated might take, then is possible to represent prior ignorance with a uninformative prior distribution. The most typical diffuse prior corresponds to a rectangular (uniform or flat) probability distribution, which says that

each value of the parameter is equally likely. A flat prior can be considered a reference prior, a class of priors particularly designed to represent weak prior knowledge and allow the data to dominate the posterior distribution.

- *Informative priors*: The alternative is an informative prior; representing cases where we have a substantial idea of the possible values that the parameters to be estimated can take. Here we might specify, for example, a Gaussian distribution about our prior expectation for the parameter values. The selection of informative priors is generally based on choosing distributions that match or follow some observed data or previous research results, while rejecting those that are inconsistent with some previous measurements.

Finally, it is possible to wrap together what we can call classical estimation theory which incorporates the idea of prior knowledge about likely solutions without explicitly invoking Bayes's theorem, this receives the name of the Gauss-Markov estimator (Solomon & Breckon (2011)). In a similar fashion, a key assumption in this case is that we are working over a linear model, as the one presented in expression (3.10). By considering that the noise vector is a stochastic quantity, that has zero mean and by further assuming that the noise and signal are statistically uncorrelated. Then, it is possible to find an estimator for the input distribution which is given by some linear operator on the observed data and which will minimize the error covariance matrix of the input distribution $\boldsymbol{\phi_0}$.

From here, two forms of estimators can be easily obtained. First, if we assume that we have no prior knowledge of the input distribution, which is equivalent to treating it as deterministic quantity, the Gauss-Markov estimator can be reduced to its form known as the BLUE, best linear unbiased estimator. It is important to notice that the term "best" in this case, means the lowest variance of the estimate compared to other unbiased, linear estimators. In this particular case, the estimated coefficients are given by the ordinary least squares (OLS) estimator. The second case corresponds to the case where we assume that the noise on the pixels have an equal variance σ^2 and this is uncorrelated. In this case the Gauss-Markov estimator is reduced to a standard least-squares solution.

Wallner's Optimal Reconstructor

A different approach to solve the inverse problem associated to the reconstruction process was suggested by (Wallner (1983)). In his work, the wavefront reconstructor is generalised into an optimal estimator that takes into account the characteristics of the wavefront sensor and the wavefront corrector, as well as the spatial and temporal statistics of the turbulence. In this case, the reconstruction process is considered to be an intrinsic part of the overall control law.

The reconstructed wavefront $\boldsymbol{\phi_r}$ is obtained by the use of a linear model, $\boldsymbol{\phi_r} = \mathbf{Rs}$, where $\mathbf{s}$ is the resulting vector of wavefront sensor signals and $\mathbf{R}$ is the reconstructor. The optimal reconstructor $\mathbf{R}$ will be the one that minimises the difference between the reconstructed wavefront and the original wavefront. For this, different metrics can be employed to assess the performance of wavefront reconstruction. One of them is the mean square error $< \varepsilon^2 >$ (MSE),

$$< \varepsilon^2 >=< (\boldsymbol{\phi_0} - \boldsymbol{\phi_r})^2 >$$

where $\boldsymbol{\phi_0}$ and $\boldsymbol{\phi_r}$ are the vectors of the actual/original wavefront and reconstructed wavefront coefficients, respectively.

In general, there are multiple approaches to obtain the optimal wavefront reconstruction; this can be done by least-squares, minimum variance or maximum a posteriori approaches (Bakut et al. (1994); Fusco et al. (1999)). When assumptions in statistics are considered, the last approach is considered. In our case, we employed minimum variance. The optimal reconstructor will minimize the mean of the square error and is found by the usual method of differentiation ($\frac{\partial <\varepsilon^2>}{\partial R}$). The expressions that we employed to build and evaluate the performance of the optimal reconstructor for our system will be derived in the following paragraphs.

From the SHWFS, the measured data can be written as,

$$\mathbf{s} = \mathbf{S}\boldsymbol{\phi_0} + \mathbf{n} \tag{3.11}$$

where $\boldsymbol{\phi_0}$ represents the original/input wavefront, $\mathbf{n}$ corresponds to the wavefront sensor

noise, $\mathbf{S}$ is called the response matrix, which is a linear operator between the input/output of the wavefront and finally, $\mathbf{s}$ corresponds to the data from the sensor (x-y spot displacements). In our case we use a modal wavefront sensing approach, thus we express the aberration on a set of basis. In our case the selected basis correspond to Zernike polynomials. Then, we need to convert those x-y spot displacements into Zernike modes or coefficients. This is done by the response matrix, it relates spot displacements with Zernike mode coefficients based on a theoretical model, that follows Malacara indexing scheme (Malacara (2007)).

The linear operator in this case can be written as $\boldsymbol{\phi_r} = \mathbf{Rs}$, using the same variables presented before. Following a similar approach presented by Wallner (1983), with some variations in order to simplify the expressions that he presented (such as without considering the actuator command vector).

Then, we define the wavefront error as,

$$\boldsymbol{\phi_e} = \boldsymbol{\phi_0} - \boldsymbol{\phi_r} \tag{3.12}$$

with the norm of the wavefront error defined as

$$\varepsilon = \boldsymbol{\phi_e}^{\mathrm{t}} \boldsymbol{\phi_e} \tag{3.13}$$

Then, we write an expression for the mean-square error of the wavefront using $\boldsymbol{\phi_e}$

$$\begin{aligned} <\varepsilon^2> &= <\boldsymbol{\phi_e}^{\mathrm{t}} \boldsymbol{\phi_e}> \\ &= <(\boldsymbol{\phi_0} - \boldsymbol{\phi_r})^{\mathrm{t}} (\boldsymbol{\phi_0} - \boldsymbol{\phi_r})> \\ &= <(\boldsymbol{\phi_0} - \mathbf{Rs})^{\mathrm{t}} (\boldsymbol{\phi_0} - \mathbf{Rs})> \end{aligned}$$

rearranging we have

$$<\varepsilon^2> = <\mathbf{s}^{\mathrm{t}} \mathbf{R}^{\mathrm{t}} \mathbf{Rs}> - <\boldsymbol{\phi_0}^{\mathrm{t}} \mathbf{Rs}> - <\mathbf{s}^{\mathrm{t}} \mathbf{R}^{\mathrm{t}} \boldsymbol{\phi_0}^{\mathrm{t}}> + <\boldsymbol{\phi_0}^{\mathrm{t}} \boldsymbol{\phi}_0> \tag{3.14}$$

Using this expression for the mean-squared error of the wavefront, the optimal reconstructor is found by

$$\begin{aligned}\frac{\partial < \varepsilon^2 >}{\partial R_{ij}} &= 0, \quad \forall i,j \\ \frac{\partial < \varepsilon^2 >}{\partial R_{ij}} &= \frac{\partial}{\partial R_{ij}} \left[< \mathbf{s}^{\mathrm{t}}\mathbf{R}^{\mathrm{t}}\mathbf{R}\mathbf{s} > - < \boldsymbol{\phi_0}^{\mathrm{t}}\mathbf{R}\mathbf{s} > - < \mathbf{s}^{\mathrm{t}}\mathbf{R}^{\mathrm{t}}\boldsymbol{\phi_0}^{\mathrm{t}} > + < \boldsymbol{\phi_0}^{\mathrm{t}}\boldsymbol{\phi}_0 > \right]\end{aligned}$$

The expression can be re-written using the following identities

$$\begin{aligned}\frac{\partial}{\partial B_{ij}} \left[\mathbf{a}^{\mathrm{t}}\mathbf{B}\mathbf{c} \right] &= \left[\mathbf{a}\mathbf{c}^{\mathrm{t}} \right]_{ij} \quad (A) \\ \frac{\partial}{\partial B_{ij}} \left[\mathbf{a}^{\mathrm{t}}\mathbf{B}^{\mathrm{t}}\mathbf{c} \right] &= \left[\mathbf{c}\mathbf{a}^{\mathrm{t}} \right]_{ij} \quad (B)\end{aligned}$$

To finally obtain

$$\begin{aligned}\frac{\partial < \varepsilon^2 >}{\partial R_{ij}} &= 2 < \mathbf{R}\mathbf{s}\mathbf{s}^{\mathrm{t}} > -2 < \boldsymbol{\phi_0}\mathbf{s}^{\mathrm{t}} >= 0 \\ 2 < \mathbf{R}\mathbf{s}\mathbf{s}^{\mathrm{t}} > &= 2 < \boldsymbol{\phi_0}\mathbf{s}^{\mathrm{t}} > \\ \frac{\mathbf{R} < \mathbf{s}\mathbf{s}^{\mathrm{t}} >}{< \mathbf{s}\mathbf{s}^{\mathrm{t}} >} &= \frac{< \boldsymbol{\phi_0}\mathbf{s}^{\mathrm{t}} >}{< \mathbf{s}\mathbf{s}^{\mathrm{t}} >}\end{aligned}$$

With the optimal reconstructor represented by

$$\mathbf{R} = < \boldsymbol{\phi_0}\mathbf{s}^{\mathrm{t}} > \left[< \mathbf{s}\mathbf{s}^{\mathrm{t}} > \right]^{-1} \tag{3.15}$$

This expression can be re-written using expression 3.11,

$$\mathbf{R} = < \boldsymbol{\phi_0} \left(\mathbf{S}\boldsymbol{\phi_0} + \mathbf{n} \right)^{\mathrm{t}} > \left[< \left(\mathbf{S}\boldsymbol{\phi_0} + \mathbf{n} \right)\left(\mathbf{S}\boldsymbol{\phi_0} + \mathbf{n} \right)^{\mathrm{t}} > \right]^{-1}$$

From this expression, some terms can be eliminated considering that the noise is independent of the signal obtained for the wavefront. Based on this, the terms $< \boldsymbol{\phi_0}\mathbf{n}^{\mathrm{t}} >$ or $< \boldsymbol{\phi_0}^{\mathrm{t}}\mathbf{n} >$ can be made equal to zero. Then, reducing the expression for the optimal reconstructor based on the response matrix, sensor noise and the input wavefront, the reconstructor can be expressed as

$$\mathbf{R} =< \boldsymbol{\phi_0}\boldsymbol{\phi_0}^{\mathrm{t}} > \mathbf{S}^{\mathrm{t}} \left[\mathbf{S} < \boldsymbol{\phi_0}\boldsymbol{\phi_0}^{\mathrm{t}} > \mathbf{S}^{\mathrm{t}} + < \mathbf{n}\mathbf{n}^{\mathrm{t}} >\right]^{-1} \tag{3.16}$$

We want to study the wavefront reconstruction problem, particularly the question about how well the system performs under less-than ideal conditions. These less than ideal conditions result from the inability to build a perfect wavefront sensor, where the accuracy is limited by the photon noise and the finite number of sampling areas, but also, of the prior information employed in the wavefront reconstruction.

In this study, we employed the MSE $< \varepsilon^2 >$ (expression 3.14), that can be re-written using the expression for the optimal reconstructor (expression 3.16), obtaining

$$< \varepsilon^2 >= \mathrm{tr} < \boldsymbol{\phi_0}^{\mathrm{t}}\boldsymbol{\phi_0} > -\mathrm{tr}\left[< \mathbf{s}\boldsymbol{\phi_0}^{\mathrm{t}} >< \boldsymbol{\phi_0}\mathbf{s}^{\mathrm{t}} >< \mathbf{s}\mathbf{s}^{\mathrm{t}} >^{-1}\right] \tag{3.17}$$

This expression for the MSE gives a measure on the accuracy of the reconstruction. It includes the errors from non estimated modes (truncation), noise propagation and bias.

A more simple expression for equation (3.17) can be obtained by replacing the expression presented for the measured data (expression 3.11), obtaining

$$\begin{aligned} < \varepsilon^2 > \; &= \mathrm{tr}\left[\boldsymbol{S}^{\mathrm{t}}\boldsymbol{R}^{\mathrm{t}}\boldsymbol{R}\boldsymbol{S} < \boldsymbol{\phi_0}^{\mathrm{t}}\boldsymbol{\phi_0} >\right] - \mathrm{tr}\left[\boldsymbol{S}\boldsymbol{R} < \boldsymbol{\phi_0}^{\mathrm{t}}\boldsymbol{\phi_0} >\right] - \mathrm{tr}\left[\boldsymbol{S}^{\mathrm{t}}\boldsymbol{R}^{\mathrm{t}} < \boldsymbol{\phi_0}^{\mathrm{t}}\boldsymbol{\phi_0} >\right] \\ &\quad + \mathrm{tr} < \boldsymbol{\phi_0}^{\mathrm{t}}\boldsymbol{\phi_0} > + \mathrm{tr}\left[< \boldsymbol{R}^{\mathrm{t}}\boldsymbol{R} >< \boldsymbol{n}^{\mathrm{t}}\boldsymbol{n} >\right] \end{aligned} \tag{3.18}$$

Expression 3.18 is easier to evaluate compared to expression (3.17), as the response matrix $\boldsymbol{S}$ can be obtained experimentally. Also, reconstructor matrix $\boldsymbol{R}$, the covariance matrix $< \boldsymbol{\phi_0}\boldsymbol{\phi_0}^{\mathrm{t}} >$ and the noise $< \boldsymbol{n}\boldsymbol{n}^{\mathrm{t}} >$ can be generated in a more efficient manner.

In this work we assess the reconstruction by the total error. The contribution of each error term to the total error can be found in the literature (Bará et al. (2012); Dai (1996); Shengyang et al. (2013)).

In astronomy, for light propagation through turbulence, Kolmogorov's theory has been widely used to describe atmospheric turbulence. Different experiments have confirmed that

the atmosphere behaves according to Kolmogorov's theory most of the time (Dayton et al. (1992); Hickson (2014)) even though in some instances non-Kolmogorov behavior has been noted (Rao et al. (1999); Nicholls et al. (1995); Boreman & Dainty (1996)). Then, prior knowledge in this case generally follows a phase structure based on Kolmogorov's model.

However, in microscopy the phase structure of the samples is unknown. A small number of articles can be found in the literature addressing the problem associated to the lack of a general model of the micro-optical properties of biological samples. As an example, (Schmitt & Kumar (1996)) using a phase-contrast microscope, were able to measure the spatial variations in the index of refraction on a variety of biological tissues. Fresh tissues samples of mouse ear, human skin, liver and intestine were employed for their research. Viewed over a range of scales, the measured spectrum of index variations for these samples exhibited a power law behaviour and their structure function fitted the Kolmogorov's model of turbulence. A similar behaviour was exhibited in human eyes (Cagigal et al. (2002)), where a Shack-Hartmann sensor was used to study light propagation though the eyes of 84 healthy subjects, whose ages ranged from 20 to 29 years. Different conclusions were reached by (Pailos & Bará (2014)) when they studied a smaller group (36 subjects, ages between 45 to 65 years old) of healthy human eyes. Their results showed that the statistics of the aberrations in their sample were not well described by the Kolmogorov or other power law models. All these observations are fundamental to understanding light propagation in tissues and provide some attempt at constraining the range of feasible models, in order to build the controller task in microscopy.

Expressions (3.16), (3.17) and (3.18)require the covariance matrix $< \boldsymbol{\phi_0}\boldsymbol{\phi_0}^{\mathrm{t}} >$ in order to be evaluated. This covariance matrix is derived using the expression found in Noll's paper (Noll (1976)) for the Wiener spectrum of the phase fluctuations in a Zernike representation, taking into account the minor corrections performed to this expression by Wang & Markey and Roddier (Wang & Markey (1978); Roddier (1990)). The elements of this matrix are given by

$$< a_j^* a_{j'} >= \int\int dk dk' Q_j^*(k) \Phi(k/R, k'/R) Q_{j'}(k') \tag{3.19}$$

where $Q_j(k)$ is the Fourier transform of the Zernike polynomial Z_j and Φ is the Wiener spectrum of the phase fluctuations, following the index order introduced by Malacara (Malacara

(2007)).

The prior knowledge in this formulation is introduced by means of the Wiener spectrum in (3.19). From here, variations in this function will lead to different wavefront reconstructors.

3.3 Prior knowledge testing

The effect of using different prior information models in an optimal reconstructor for cases where the assumed model differs from the actual wavefront statistics is the aim of this Chapter. This allowed us to quantify the performance of wavefront reconstruction for a range of different wavefront models and determine suitable choices for prior statistics for cases where the aberrations may not be well known.

Different statistics or priors were introduced into the system performance calculation by means of the covariance matrix. By changing the Wiener spectrum, we are able to introduce these different wavefront statistics. Thus, we can create wavefronts that do not merely follow Kolmogorov's statistics, and with these we are able to test how the system should perform under different scenarios. Also, a non-informative prior covariance matrix was employed. This matrix was built considering that all the Zernike coefficients were equally probable, then an identity matrix was employed in this case ($\mathbb{I}$). Using the mean-square error we can quantify how well our system will work when different input wavefronts are measured. This can be done using either the same or different wavefront statistics compared to the input wavefront. This can give us a range where the reconstructor will perform close to the optimum. This was also done using different values of signal-to-noise ratio (SNR).

When informative prior was employed, the values of these covariance matrices were obtained by varying the value of the exponent of the Wiener spectrum in expression (3.19). The Wiener spectrum is defined as

$$\Phi(k) \sim Ak^{-\alpha}$$

with A constant and if we use $\alpha = 3.67$, it represents the Kolmogorov statistics. In Noll's paper, in order to obtain the values for each covariance matrix element ($< a_j^* a_{j'} >$, expression (3.19)) requires the evaluation of the next integral

$$I_{nn'} = \int_0^\infty k^{-8/3} \frac{J_{n+1}(k) J_{n'+1}(k) dk}{k^2} \tag{3.20}$$

that is tabulated in most standard integral tables handbooks of Bessel function integrals. For this particular case, when using Kolmogorov's statistics, the analytical solution is given by

$$I_{nn'} = \frac{\Gamma(\frac{14}{3})\Gamma\left[(n+n'-14/3+3)/2\right]}{2^{14/3}\Gamma\left[(-n+n'+14/3+1)/2\right]\Gamma\left[(n-n'+14/3+1)/2\right]\Gamma\left[(n+n'+14/3+3)/2\right]} \tag{3.21}$$

However, as we want to study different statistics, not all α values can be employed to generate the elements of these covariance matrices. Then, we need to employ the more general form for the integral in expression (3.20)

$$I_{\mu\nu} = \int_0^\infty \frac{J_\mu(at) J_\nu(bt) dt}{t^\lambda} \tag{3.22}$$

and its analytical solution

$$I_{\mu\nu} = \frac{a^{\lambda-1}\Gamma(\lambda)\Gamma(\frac{\nu+\mu-\lambda+1}{2})}{2^\lambda \Gamma(\frac{-\nu+\mu+\lambda+1}{2})\Gamma(\frac{\nu+\mu+\lambda+1}{2})\Gamma(\frac{\nu-\mu+\lambda+1}{2})} \tag{3.23}$$

Expression (3.22) becomes (3.20), when $a = b = 1$, $\mu = n + 1$, $\nu = n' + 1$ and $\lambda = 14/3$.

The integral presented in expression (3.22) is well defined over a certain range of values and diverges for others (Abramowitz & Stegun (1964); Dixon & Ferrar (1930)), then limiting the values for α that can be employed in our numerical simulation. The range where the integral has a finite solution is: $1 \leqslant \alpha < 4$. Then, we employed different values between this range to define the Wiener spectrum that was used to generate the different covariance matrices.

Figure 3.2 shows the plots of the different covariance matrices that were generated, using informative and non-informative priors.

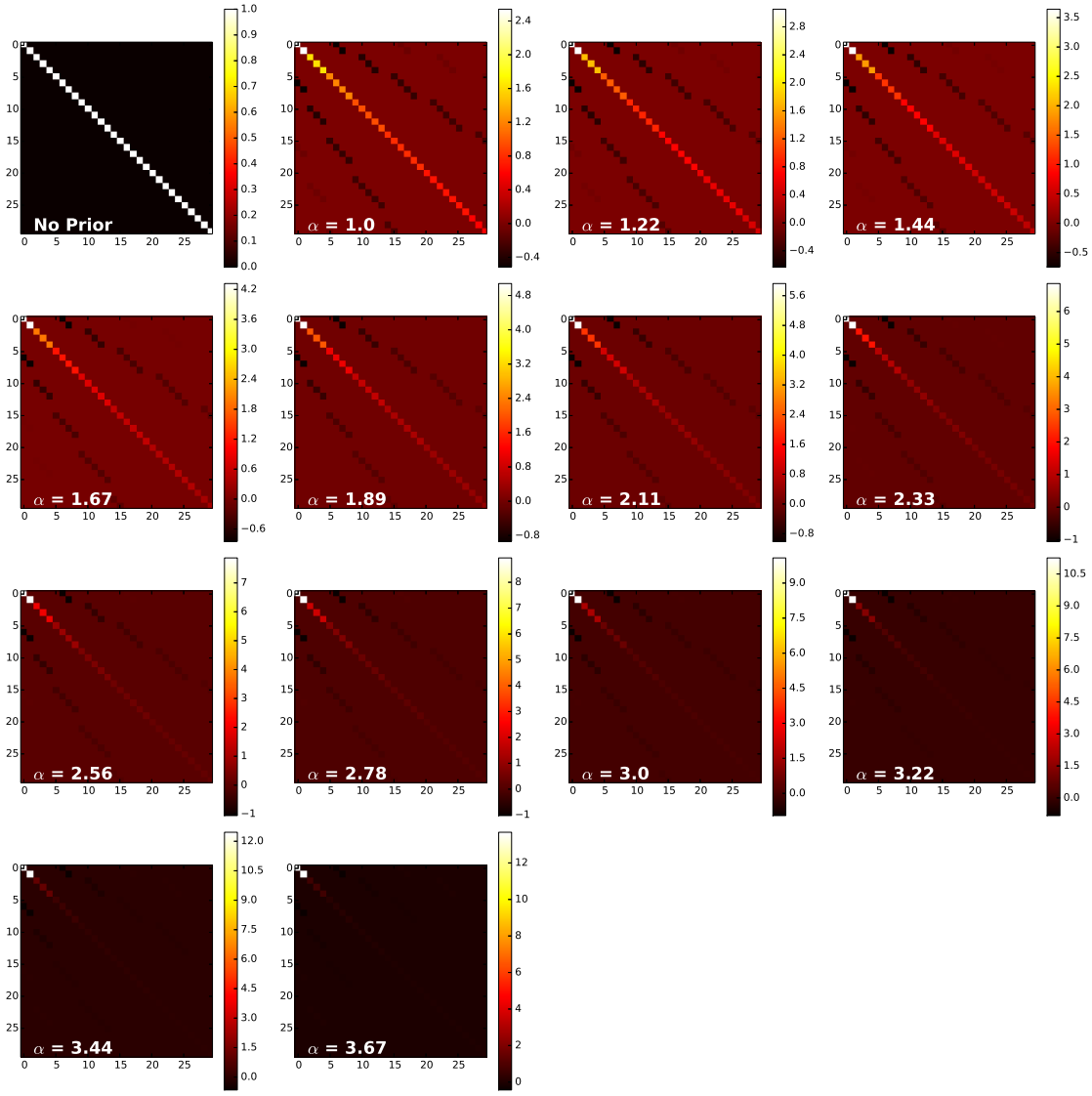


Figure 3.2: Covariance matrices of Zernike modes generated using different values for the Wiener spectrum. Each one represents different normalized wavefront statistics that will be employed to test the reconstruction performance. The first matrix, however, corresponds to the particular case where no prior is considered. In this case, all the Zernike coeficients are equally weighted.

To quantify the performance of the wavefront reconstruction process, we can assume a range of possible wavefront statistics for the input wavefront to be measured, the statistics are represented by α_0. Then, it is also possible to utilise the same or different statistics as prior knowledge to build the system reconstructor. The reconstructor can be built using

any value in the range presented before for the Wiener spectrum, where α_{R} represents the wavefront statistics used for the reconstructor.

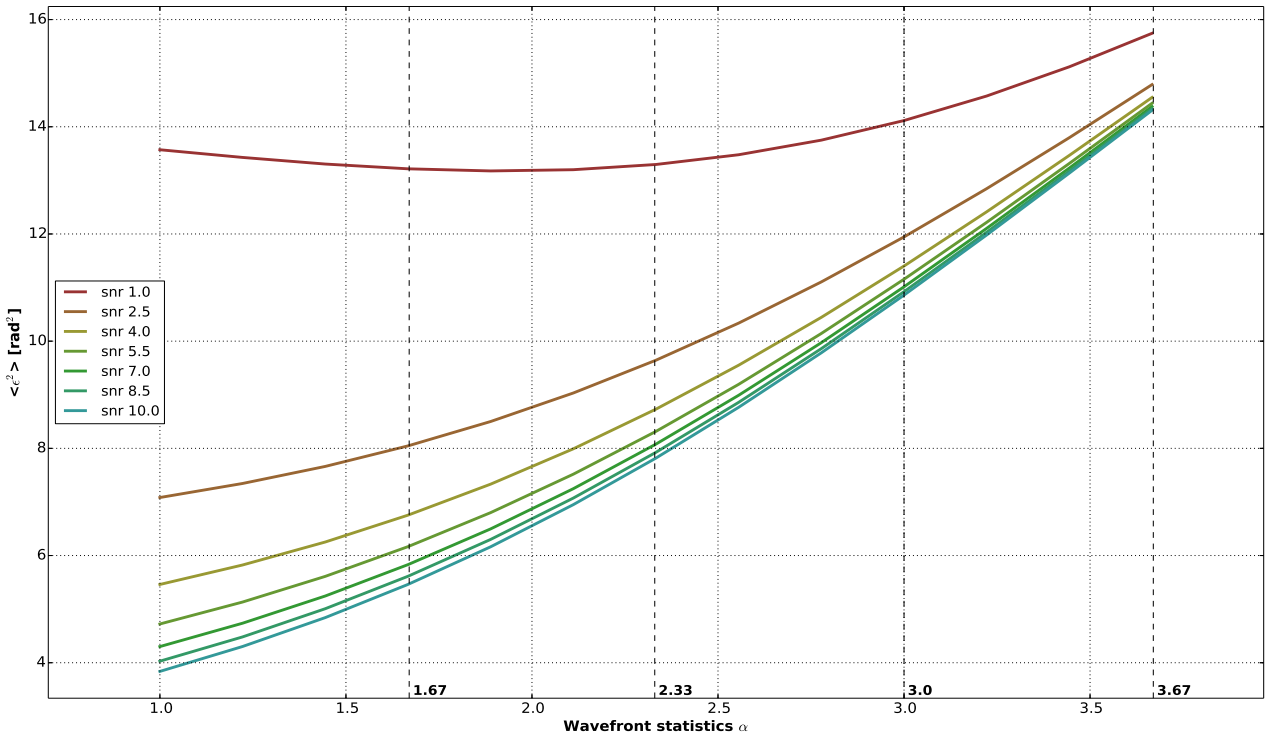


Figure 3.3: Error values obtained when reconstructing the wavefront with various Wiener spectrum exponents α_0, using a non-informative prior statistics ($\alpha_{\mathrm{R}} = \mathbb{I}$), at different SNR.

Then, it is possible to evaluate the error between the input wavefront and the reconstructed wavefront, if the prior does not match the input wavefront statistics ($\alpha_0 \neq \alpha_{\mathrm{R}}$). The goal is to avoid a choice of prior that could lead to a bad performance of the system.

To have a better understanding about the role of prior knowledge, Figure 3.3 shows the values obtained for the MSE when different input wavefront with different statistics α_0 are reconstructed using a non-informative prior as the statistics for the reconstructor (α_R). From this figure it is possible to infer that the use of prior seems to be relevant only at low SNR (defining low SNR as $\leq$10). From this figure, four different values for the input wavefront statistics (α_0 =1.67, 2.33, 3.0 and 3.67) have been selected to compare the values obtained for the MSE when the reconstructor employed matched the input wavefront ($\alpha_R = \alpha_0$) and

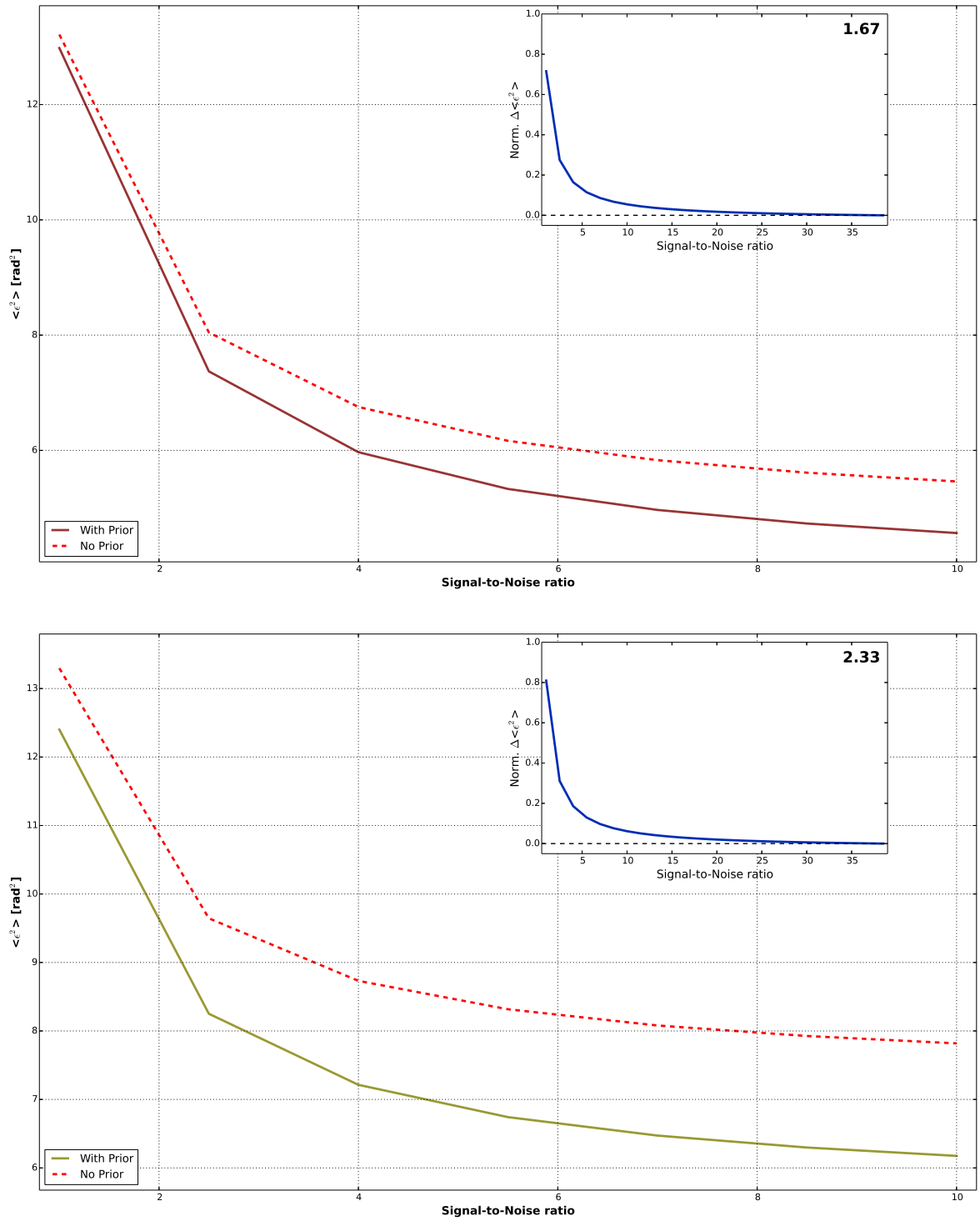


Figure 3.4: Error values obtained when an input wavefront with fix statistics is reconstructed with a matching informative prior $\alpha_R = \alpha_0$ and using a non-informative prior $\alpha_R = \nVdash$ for different SNR. **Top:** α_0=1.67, **Bottom:** α_0=2.33. In both panels the inset shows the normalised difference obtained for the MSE considering $\alpha_R = \alpha_0$ and $\alpha_R = \mathbb{I}$. The difference between MSE is bigger at lower values for SNR (≤ 20), while for high SNR, whether we use a prior or not does not make a big difference, as MSE reaches zero.

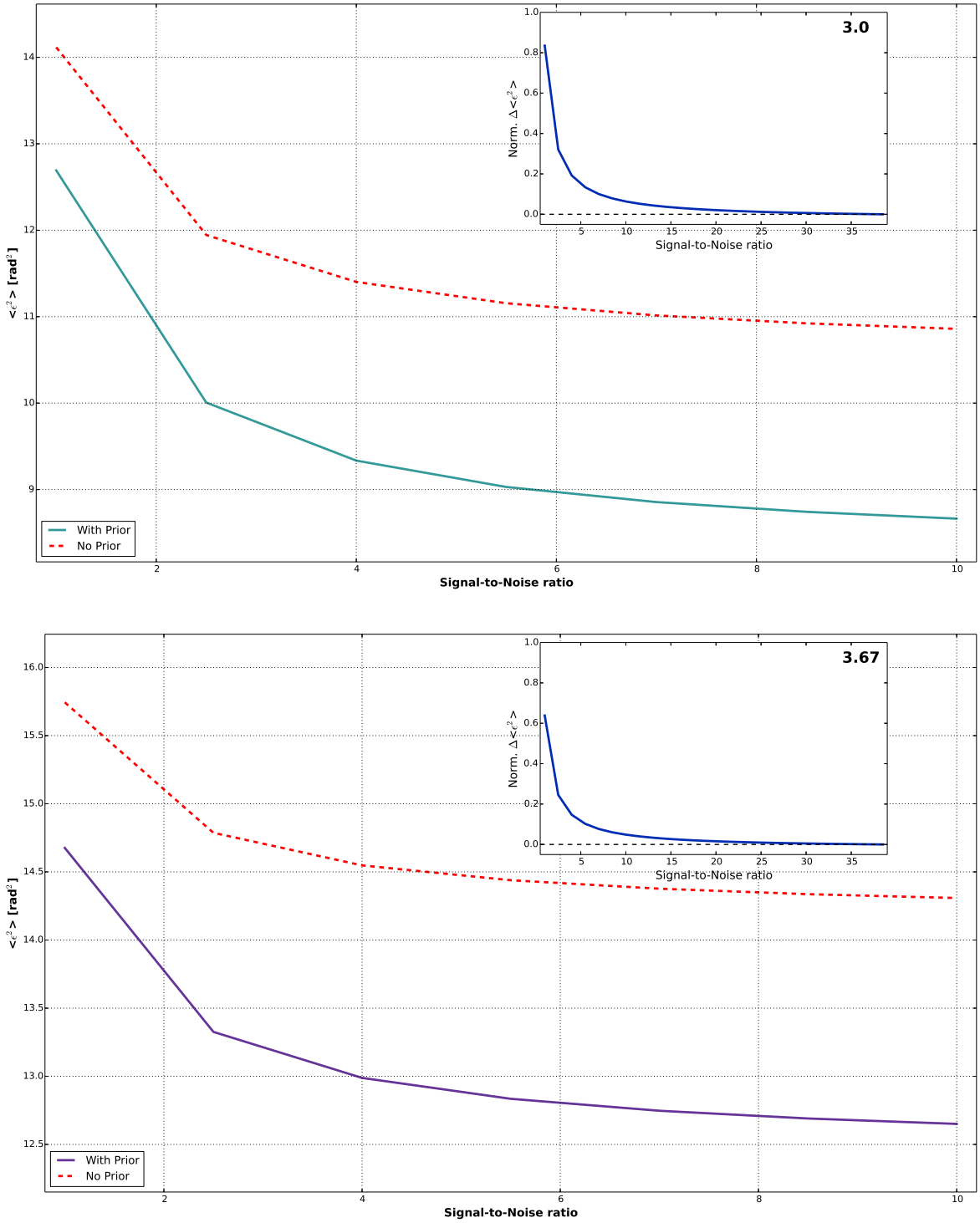


Figure 3.5: Error values obtained when an input wavefront with fix statistics is reconstructed with a matching informative prior $\alpha_R = \alpha_0$ and using a non-informative prior $\alpha_R = \nVdash$ for different SNR. **Top:** α_0=3.0, **Bottom:** α_0=3.67. In both panels the inset shows the normalised difference obtained for the MSE considering $\alpha_R = \alpha_0$ and $\alpha_R = \mathbb{I}$. The difference between MSE is bigger at lower values for SNR (≤ 20), while for high SNR, whether we use a prior or not does not make a big difference, as MSE reaches zero.

for the case when the reconstructor employed a non-informative prior ($\alpha_R = \mathbb{I}$).

The values obtained for the MSE are presented in Figure 3.4 and Figure 3.5. In these Figures we also show the normalised difference obtained for the MSE considering $\alpha_R = \alpha_0$ and $\alpha_R = \mathbb{I}$ for a larger range of SNR values. From the inset plots, we can see that the difference between MSE is bigger at lower values for SNR (≤ 20), while for high SNR, whether we use a prior or not does not make a big difference, as MSE reaches zero. Then, it is possible to infer that the use of informative prior is justificable only at low SNR, where the introduction really leads to a decrease in the value obtained for the MSE.

The next step was to investigate the effect of only using an informative prior. In our case we expect SNR lower than 15, then the use of non-informative prior will introduce more errors, reducing the performance of the system. Again, we calculate the MSE obtained at different SNR when the same input wavefront statistics was employed in the reconstructor ($\alpha_0 = \alpha_R$) and when these two were different.

In Figure 3.6, the reconstructor error is plotted against reconstructor prior (α_{R}) for wavefronts with different statistics (α_0). In this case, each curve represents a particular wavefront statistics (α_0).

From these results it is possible to see that there is a difference in the values obtained for the MSE, generally the minimum value will be obtained when the input wavefront statistics match the statistics used to built the reconstructor ($\alpha_0 = \alpha_{\mathrm{R}}$), this particular case can be considered as the optimal reconstructor. The optimal reconstructor will always lead to the minimum error attainable, even for low SNR values as 1. Also, from the results, the use of different statistics in the reconstructor, leads to a bigger MSE error value. It is important that when $\alpha_0 \neq \alpha_{\mathrm{R}}$, the value obtained for the error depends on which value was employed as the prior in the reconstructor. From the values obtained before, when $\alpha_R > \alpha_0$ the error value decreases, especially at high SNR value, but is not comparable to the values obtained when $\alpha_R < \alpha_0$

Then it is possible to infer that the wavefront reconstruction process should have a good performance (low error value) for α_R larger than 2.33.

As prior information of the wavefront statistics is not known, the aim is to try to avoid

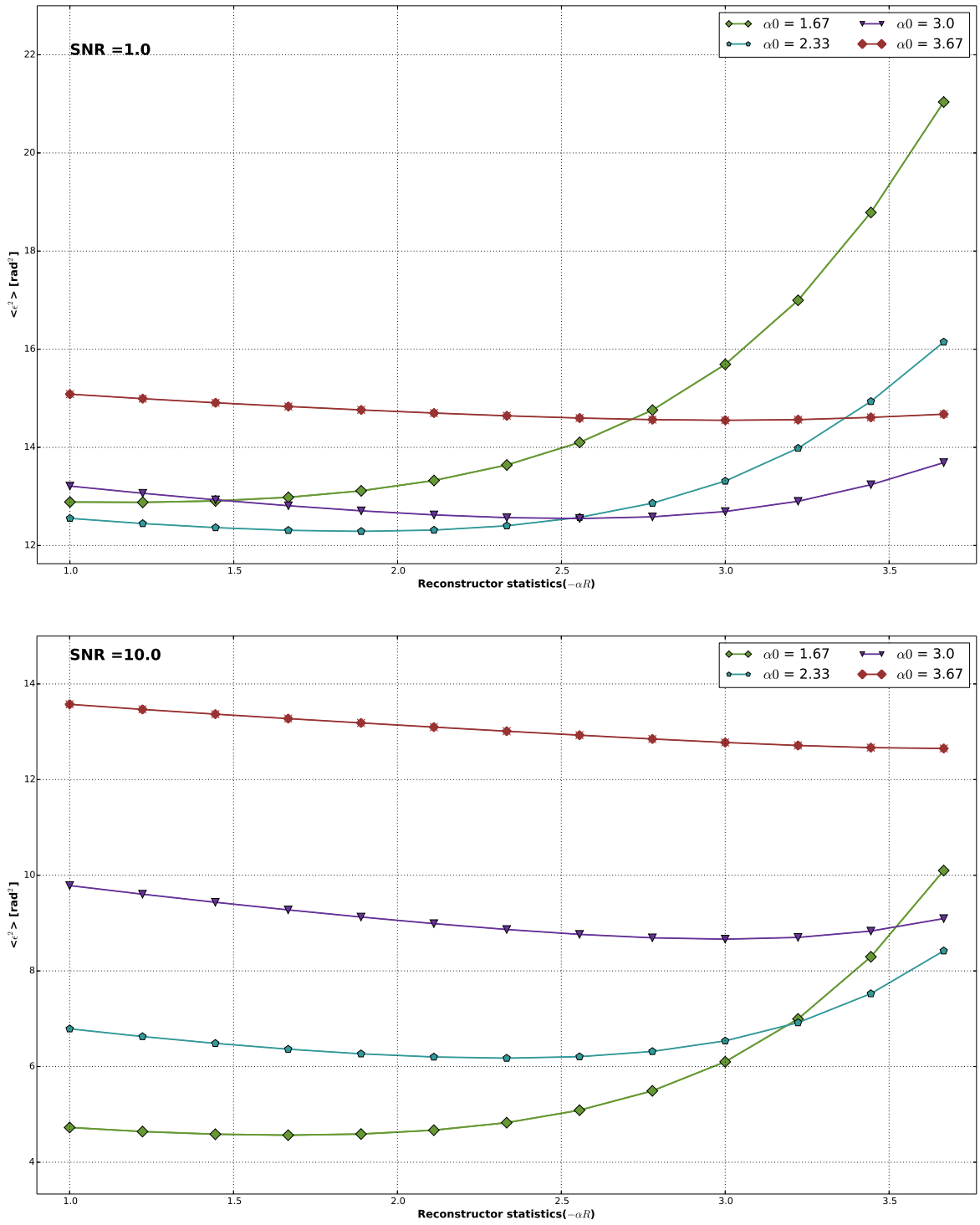


Figure 3.6: Error values obtained when reconstructing wavefronts with various Wiener spectrum exponents α_0 using different prior statistics (α_R). **Top:** SNR=1, **Bottom:** SNR=10.

those possible prior values that could lead to a reduction in the system's performance. Figure 3.7 shows reconstruction errors when various Wiener spectrum exponents α_0 are used. In this case, different prior statistics (α_R) were used at two different SNR values. By using a more finite range of values for the prior, betwen 2.33 and 3.67, we might obtain a better value for the prior that could lead to a better performance across the whole range of possible input wavefront options.

As presented by (Korff et al. (1975)), a translation-invariant region depends on the spatial frequency content of the data. The same transformation may not be translation-invariant to the same extent at different spatial frequencies, the size of the region or range will depend on the frequency content of the imaged data. Then, it will depend on the amount of detailed structure that the data contains, in our case, frequency content is directly related to the Wiener spectrum power that was employed to generate the covariance matrices and so, the input wavefront statistics.

Then, we can infer that the aberrations introduced by different samples in the microscope could be adequately reconstructed by using as prior any wavefront statistics in the range $2.33 \leqslant \alpha_R \leqslant 3.67$. This can done by defining a desired accuracy not bigger than $\sim$0.03 rad^2 (smaller than 10%), that corresponded in our case to the difference obtained when $\alpha_0 \neq \alpha_R$, for $\alpha_0 < \alpha_R$.

Finally, the error values are investigated for three different reconstructors at different SNR values. These results are presented in Figure 3.8 and Figure 3.9, using α_R =2.33, 3.0 and 3.67 and the whole range of possible input wavefront statistics. From these, it is possible to consider a reconstructor using α_R=3.0 as the optimal reconstructor, particularly when the SNR is higher than 4. The use of these values seems reasonable, particularly considering the results found in the literature, where the measured spectrum of index variations for different samples exhibited a power law behaviour that was fitted by Kolmogorov's model of turbulence (Schmitt & Kumar (1996); Cagigal et al. (2002)).

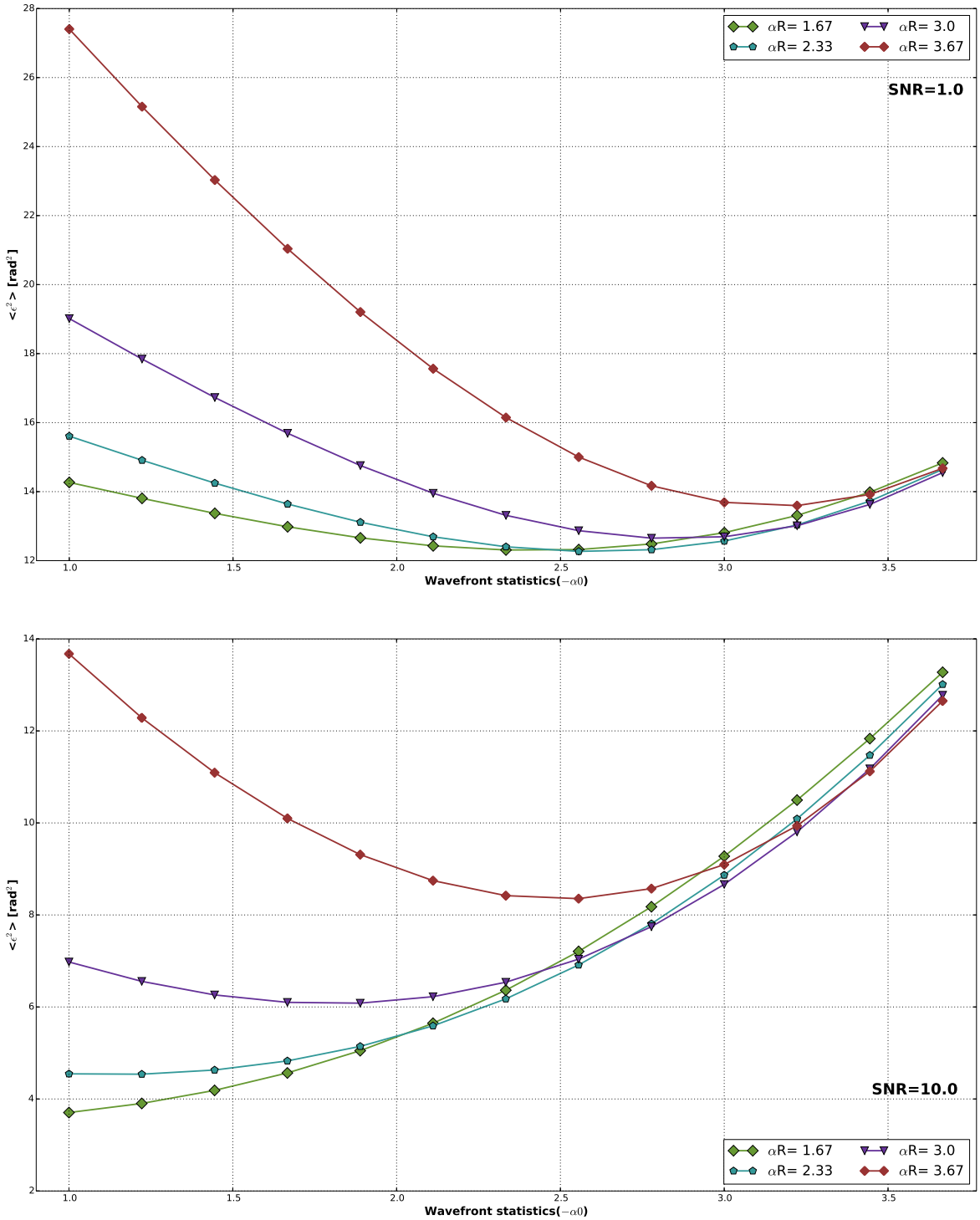


Figure 3.7: Different values of α_R were used to reconstruct different input wavefronts. From here a better understanding of the possible values that need to be avoided to build the reconstructor can be inferred. **Top:** SNR=1, **Bottom:** SNR=10.

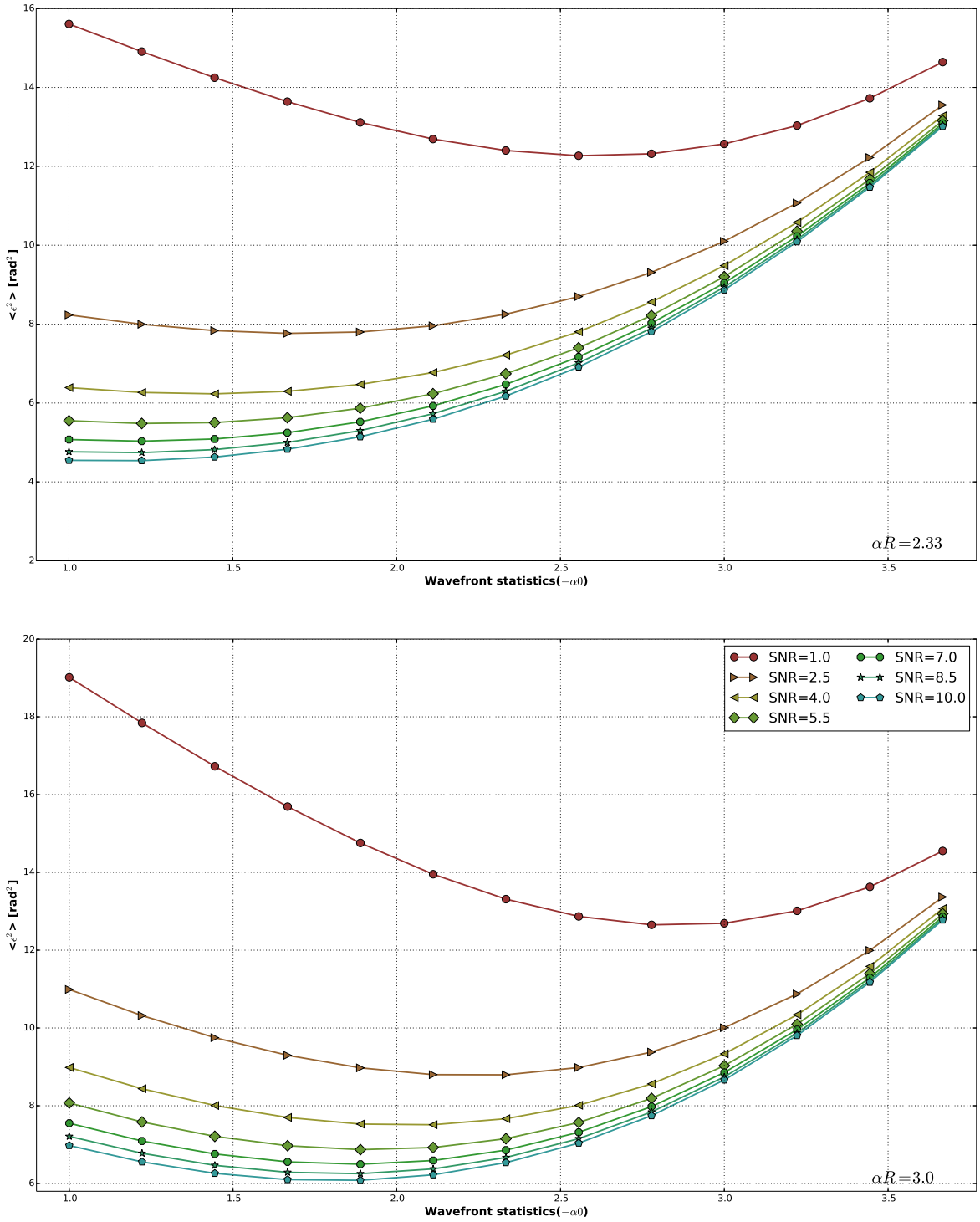


Figure 3.8: MSE values when different input wavefronts are reconstructed using $\alpha_{\mathrm{R}} = 2.33$ and 3.0, for different SNR values. **Top:** α_{R}=2.33, **Bottom:** α_{R}=3.0.

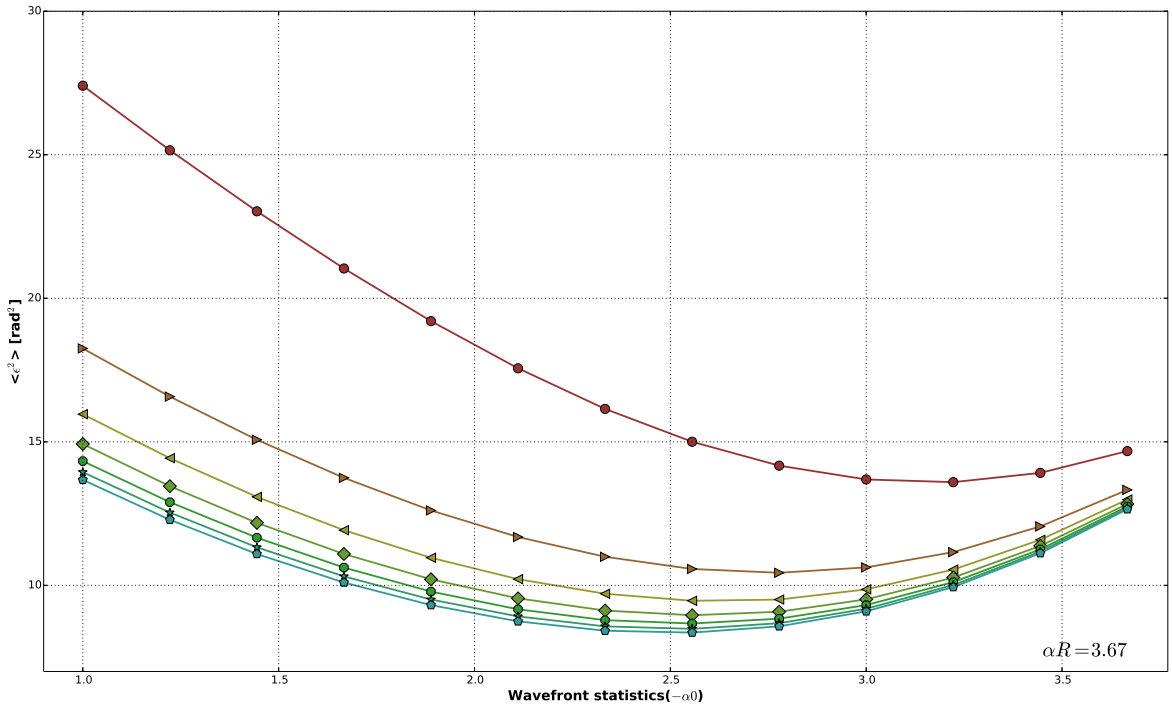


Figure 3.9: MSE values when different input wavefronts are reconstructed using $\alpha_{\mathrm{R}} = 3.67$, for different SNR values.

3.4 Conclusions

Wavefont reconstruction with different aberration statistics was performed by varying the Wiener spectrum. To assess the optimal reconstructor presented, the mean square error was formulated and numerically evaluated. To have a better understanding about the role of prior knowledge, values obtained for the MSE when different input wavefront with different statistics α_0 are reconstructed using a non-informative prior as the statistics for the reconstructor (α_R).From the results presented it is possible to infer that the use of prior seems to be relevant only at low SNR (defining low SNR as $\leq$10). Four different values for the input wavefront statistics (α_0 =1.67, 2.33, 3.0 and 3.67) were selected to compare the values obtained for the MSE when the reconstructor employed matched the input wavefront ($\alpha_R = \alpha_0$) and for the case when the reconstructor employed a non-informative prior ($\alpha_R = \mathbb{I}$). From these results, the difference between MSE was bigger at lower values for SNR (≤ 20), while for high SNR, the use of prior or not prior does not make a big difference, as MSE reaches zero. Then, it is possible to infer that the use of informative prior is justificable only at low SNR, where the introduction really leads to a decrease in the value obtained for the MSE.

It was found that the mean square error is smaller when the same statistics are employed in the wavefront to be reconstructed and in the reconstructor ($\alpha_0 = \alpha_{\mathrm{R}}$). For those cases where the reconstructor follows a different statistics, the mean square error value depends on the SNR and of the difference between α_0 and α_{R}.

Bigger error values were found when α_{R} was bigger than the value employed to describe the input wavefront statistics, particularly at high SNR. These results showed that even when the reconstructor is not the optimal one ($\alpha_0 = \alpha_{\mathrm{R}}$), wavefront reconstruction with a low error can be obtained. Then, it is possible to define a range of values that will lead to small MSE values, independent of the input wavefront statistics. This range was found to be $2.33 \leqslant \alpha_{\mathrm{R}} \leqslant 3.67$, for SNR$\geqslant$10. A reconstructor using $\alpha_{\mathrm{R}} = 3.0$ seems to be the best option for SNR values higher than 4, as the error values obtained in this case were small for the whole range of possible input wavefront statistics. The use of this value also agrees with the results found in the literature, where different samples seems to exhibit a power law behaviour on the variation of their refractive indices that can be fitted by the Kolmogorov's model of turbulence

These results are important in microscopy, where we do not have precise prior information

about the aberration statistics being observed. Therefore, if some aberration statistics would be inherently more likely than others, there are some reasons to pick up one reconstructor over another, particularly at low SNR values. In this case the most suitable solution for the problem of wavefront reconstruction would seem to be a reconstructor that can perform efficiently over a wider range of different input wavefront statistics.

Chapter 4

Adaptive Optics system using backscattered light

4.1 Experimental setup

An inverted microscope frame (IX71, Olympus) was employed for the construction of a scanning laser confocal microscope with direct wavefront sensing. This type of microscope has two side ports near bench level, together with one back port and one lower port, all to facilitate the integration of optical components with the microscope. In our case, the back port was employed based on the number of components required to incorporate the adaptive optics system. The back port can provide access to the objective without needing to go through a tube lens, so a parallel pencil of rays can easily be obtained or introduced. In order to get a primary image, it is necessary to add a lens that will act as a tube lens. The manufacturer's specifications recommend a lens of focal distance equal to 180 mm, in order to minimize the effect of spherical aberrations and maintain magnification. However, due to limited space to mount extra components, a focal lens equal to 300 mm was employed to get a primary image near the back port exit.

Image projection to the optical ports is usually achieved by redirecting the light from the objective with an internal prism. In our setup, this was not necessary as the illumination path is also the imaging path. The main problem associated with the use of the back port is related to the optical component mounted in the system filter cube cassette. The design allows mounting of up to 6 filter cubes, each allowing the use of a beam splitter, mirrors or other optics as long as their dimensions do not exceed 26 mm×38 mm (L×W), or a thickness

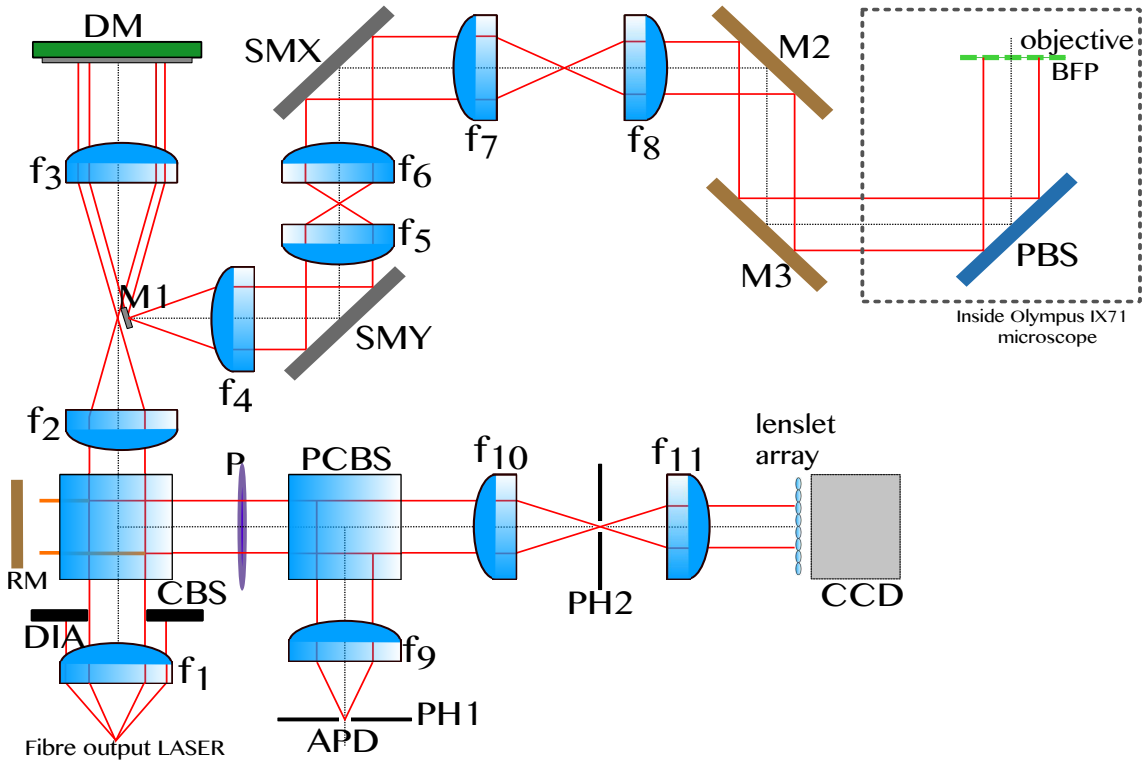


Figure 4.1: Experimental setup. All of the lenses are achromatic doublets, Linos: f_1=50 mm, f_2=100 mm, f_3=200 mm, f_4=60 mm, f_5=50 mm, f_6=50 mm, f_7=140 mm, f_8=300 mm, f_9=140 mm, f_{10}=100 mm, f_{11}=80 mm, PH1=50 µm, PH2 = 150 µm, RM: reference mirror, DIA: diaphragm, CBS: cube beam splitter, PCBS: polariser cube beam splitter, P:polariser, DM: deformable mirror, SMX-SMY: scanning mirror X-Y,M2-M3: mirrors, PBS: plate beam splitter

of 1±0.05 mm. Unfortunately, beam splitters or dichroic mirrors with that thickness value are generally both very flat, introducing big amounts of astigmatism, especially in a reflection configuration. To overcome this problem, we employed a beam splitter (90:10, R:T, QiOptiq), with dimensions of 22.4 mm×31.5 mm (L×W), thickness=3.5 mm, flatness first surface $\approx \lambda/10$. By utilizing 90% reflection and 10% transmission of the light, we were able to simultaneously observe the specimen via the eyepiece and had the option of recording bright field illumination images (Plate beam splitter:PBS, Figure 4.1). An off-axis displacement of the image was observed, due to beam splitter thickness, but this did not affect the image quality.

The ability to conduct an initial search to find an appropriate region of interest in the specimen in order to get successful observations was facilitated by a bright field illumination. This was obtained by viewing the specimen by conventional epi-illumination using the microscope's built-in halogen quartz Tungsten lamp. Once the area of interest was found and centered in the field, the illumination path was changed for the CLSM and the lamp turned off.

The light source in our system was a diode laser 680nm (Qphotonics QSDM-680-2, max. optical power 2 mW) coupled to a fibre optic (Qphotonics, HI1060, NA=0.14). A fibre coupling adapter (Linos, 3.5°, ϕ=30 mm) was mounted on an X-Y positioner stage. An achromatic doublet (Linos, ϕ=25 mm, f_1=50 mm) was employed to collimate the beam at the fibre output. In order to get a more uniform beam a diaphragm was used to block part of the beam, restricting its diameter to 5 mm (DIA, Figure 4.1).

Multiple optical relays were required to conjugate the back focal plane of the objective with the corrector, the wavefront sensor and the scanning mirrors. Conjugate planes play an important role in our system, as precise alignment is necessary to measure and correct the aberrations at the back focal plane. Misalignments between planes could introduce defocus or other aberrations. A total of five optical relays were used for the whole system. The focal lengths of their components were chosen to match the required magnification at the different alignment stages.

The illumination beam was directed towards the DM slightly off axis. The angle formed between the optical axis and a vector normal to the mirror surface was smaller than 5°. The light reflected from the DM then was redirected towards the scanning apparatus by using a small mirror (COMAR, VIS, ϕ = 10 mm), located close to the focal spot of a lens situated

slightly off-axis in front of the DM. A small incidence angle between the beam and the DM mirror surface was important to minimize off-axis aberrations.

The scanning of the laser beam across the specimen was achieved with two scanning mirrors mounted at right angles. For alignment purposes, each mirror had its own mount, independent positioning of each mirror before being clamped in place. The horizontal scan was generated by a mirror mounted on a resonant scanner that oscillates at a fixed frequency of about 8 KHz. This mirror rotates through an angle of approximately 26°, with an angular velocity that reflects a cosine function. The vertical scan is generated by a second mirror mounted on a galvanometer that rotates in response to a sawtooth waveform at 50 Hz.

Direct wavefront sensing was achieved by using a Shack-Hartmann wavefront sensor. Light from the employed lenslet array (focal length 20 mm, pitch 500 μm) was focused on a CCD camera (Pixelfly, pixel size 9.9 μm ×9.9μm, image dimension 640×480, readout noise $\leq$16e$^-$, QE ∼40% at 500 nm). A pinhole (Thorlabs, P150S-$\phi 1''$ mounted, 150±6 μm diameter) mounted on a precision X-Y-Z translation stage located at the focal point of the optical relay, allowed rejection of out-of-focus light coming from the sample.

In order to record confocal images, light reflected by the sample was redirected towards the imaging path by a polarised cube beam splitter. Light was focused through a pinhole (Thorlabs, P50S-$\phi 1''$ mounted, 50±3 μm diameter) mounted on a precision X-Y-Z translation stage. The detector used was an avalanche photodiode (m712A-4, Analog modules Inc., active area 0.5 mm, with a sensitivity peak at 830 nm, Si).

To control the amount of light required for wavefront sensing and confocal image recording, a linear polariser (Qioptiq, dichroic sheet, VIS, mount ϕ =25 mm), was located before the polarising beam splitter cube (Qioptiq, VIS, L=10 mm).

For image capture, storage, retrieval and data analysis two computers were employed. The main computer was in charge of the whole adaptive optics systems. It was controlled by home-written Python/Cython software. The software recorded the images obtained from the CCD camera, performed spot displacements analysis from these images, estimated the aberrations and calculated the signals to be sent to the DM. The deformable mirror signals were forwarded to a second computer that controls a digital-to-analogue board necessary to drive the mirror. The frame grabber used for the confocal image, requires two external

synchronization signals, which were obtained from the mirror driver unit.

Finally, to solve the problem related to the height of the microscope back port (port centre situated ∼20 cm above bench level), two mirrors were used to rise and direct the beam, from bench level to back port level. The use of these two mirrors also allowed a more accurate beam alignment inside the microscope. A target was employed at the objective position for beam alignment.

4.2 Principle of wavefront correction

The beam diameter at the deformable mirror plane was approximately 10mm, to make effective use of the influence functions of the mirror (Paterson et al. (2000)). Calibration was performed using a Hadamard matrix method (Marchetti et al. (2005)), from which the mirror-wavefront-sensor *response matrix* $\boldsymbol{M}$ was determined.

The shape of the DM was described in terms of the first 100 Zernike polynomials. The relationship between membrane deflection and voltage applied can be more extensively found in the literature (Fernandez & Artal (2003)) and is described by the Poisson equation. In order to allow DM deflections in both directions, all actuators are set initially to a constant bias voltage equal to $v_{\max}/\sqrt{2}$, with $v_{\max}$ depending of the manufacturer's value for each particular mirror. At this position, the mirror will acquire a concave shape, introducing a constant amount of defocus to the whole system. To get rid of this defocus, the lens situated right in front of the DM is moved along the optical axis to a position where it cancels the introduced defocus.

The deformable mirror has a limited range for its actuator control signals. To reduce the problems of clipping actuator control signal at their maximum range, a box-constrained iterative-least squares linear-solver is used to calculate the required actuator drive signals. Then, we implemented a linear least squares solver with constraints. Bounded non-linear problems are commonly solved by finding model parameters within bounds based on physical considerations: for a DM this corresponds to the maximum/minimum mirror deflection. In our case we used an algorithm based on Bounded Variable Least Squares (BVLS) already implemented in OpenOpt (http://openopt.org/LLSP). Then, mirror deflection signal given

a set of Zernike modes will be expressed as a bound constrained least squares problem:

$$min\|\mathbf{C}x - \phi\|_2^2, \quad \alpha \leq x \leq \beta, \tag{4.1}$$

where $\mathbf{C}$ is the system's control matrix, ϕ are the estimated Zernike polynomial coefficients and x are the signals necessaries to drive the mirror, these are the values required to correct the aberrations introduced by the sample. The control matrix is generated by using the response matrix obtained before when the system was calibrated, and its necessary to relate SHWFS spot displacement to the voltages applied to each mirror actuators. The constraint, $\alpha \leq x \leq \beta$ is related to the maximum/minimum values that the actuators can reach. These boundaries can be expressed in terms of voltages or "deflection units". For deflection units: mininum and maximum voltages ($v_{\max}$) are represented by -1 and $+1$ respectively, then bias position or $v_{\max}/\sqrt{2}$ has a value equal to zero.

4.3 Correction of Red-edged Dracaena and agarose samples

Dracaena Marginata or Madagascar Dragon Tree is just one of many houseplants belonging to the Dracaena Group. It is an excellent drought resistant plant, able to grow in partial to light shade. It corresponds to one of the several plants studied in 1989 by the National Aeronautic and Space Administration as an efficient, low cost solution to the *sick building syndrome* (Wolverton et al. (1989)), a condition related to indoor polluted environments. It has the ability to filter some harmful toxins and pollutants from the air, such as benzene and formaldehyde. These facts combined with its accessibility, price and no major safety issues made it a good first suitable sample to test our system.

The aim of this project is to correct aberrations introduced by the sample, particularly as we image deeper into it. Good images were obtained when a small portion of leaves were mounted directly over a coverglass. Thus, the use of the adaptive optics system on these samples was not necessary. This was because the amount of aberrations introduced by the samples was not strong enough. However, other samples are more complex in structure, such as skin or even bone (see Chapter 1). In those cases, thin slices of these samples are generally used. Nevertheless, this means that the sample integrity might be affected, destroying some structures in it.

To overcome the problem related to the small amount of aberration introduced by the

sample, three different approaches could be implemented: the use of an objective with a higher NA, more complex samples or to introduce aberrations in the sample by making minimum alterations to it. The selected approach was the latter, using fresh agarose as the mounting media for a small portion of leaves. This will allow us to perform wavefront corrections at deeper layers, without affecting the sample structure. The aim is to avoid the use of thin samples in order to preserve their integrity and work with samples in a more realistic scenario.

Fresh agarose ($C_{24}H_{38}O_{19}$, Sigma-Aldrich, A9539) solutions were prepared in distilled water at concentration by weight of 1% or 3%. To introduce variations in the agarose refractive index, a solution of D-(+)-Glucose ($C_6H_{12}O_6$, SigmaUltra, G7528) at concentration by weight of 4% was prepared and mixed with the agarose. Different samples were made using agarose and leaves or agarose, glucose and leaves mounted on a coverslip n°1.5. Small drops were pipetted over the coverslip and small pieces of leaves were introduced in the drops by using tweezers. Samples were kept in a refrigerator to help the agarose to gel. While imaging, a small drop of water was added on top of sample to keep it moist, delaying agarose dehydration. Once the imaging process was finished, samples were disposed of.

The idea behind this procedure was to create a thick layer of agarose between the coverslip surface and the leaf that will reduce the amount of light reaching the focal plane together with introducing aberrations. Light reflected from the sample was employed to measure and correct the aberrations. Approximately 90% of the reflected light was used to obtain the confocal images and the rest 10% was used by the SHWFS. Laser output current was set at its maximum obtaining a measured power of approximately 160±2 μW at the objective BFP.

Wavefront corrections were carried out in a first sample made of agarose at a concentration of 3% and a piece of leaf. The first imaging plane was located at a depth of 206±0.5 μm deep into the sample. In this case, chlorophyll located at the leaf surface was imaged. The light employed to sense the aberrations and to obtain the images corresponded to backscattered light from these structures. Chlorophyll autofluorescence was ruled out in our case as the laser wavelength is 680 nm, far away from the excitation wavelength necessary to generate this phenomenon (Chlorophyll: λ_{exc}: 488 nm, λ_{emi}: 685 nm) (Roshchina (2012)). The aberrations measured in this case are primarily due to planar-refractive index mismatch between the objective and coverslip and differences between refractive indices of sample constituents: agarose (n ∼1.33), chlorophyll cells (n ∼1.52), hydrated cell walls (n ∼1.47),

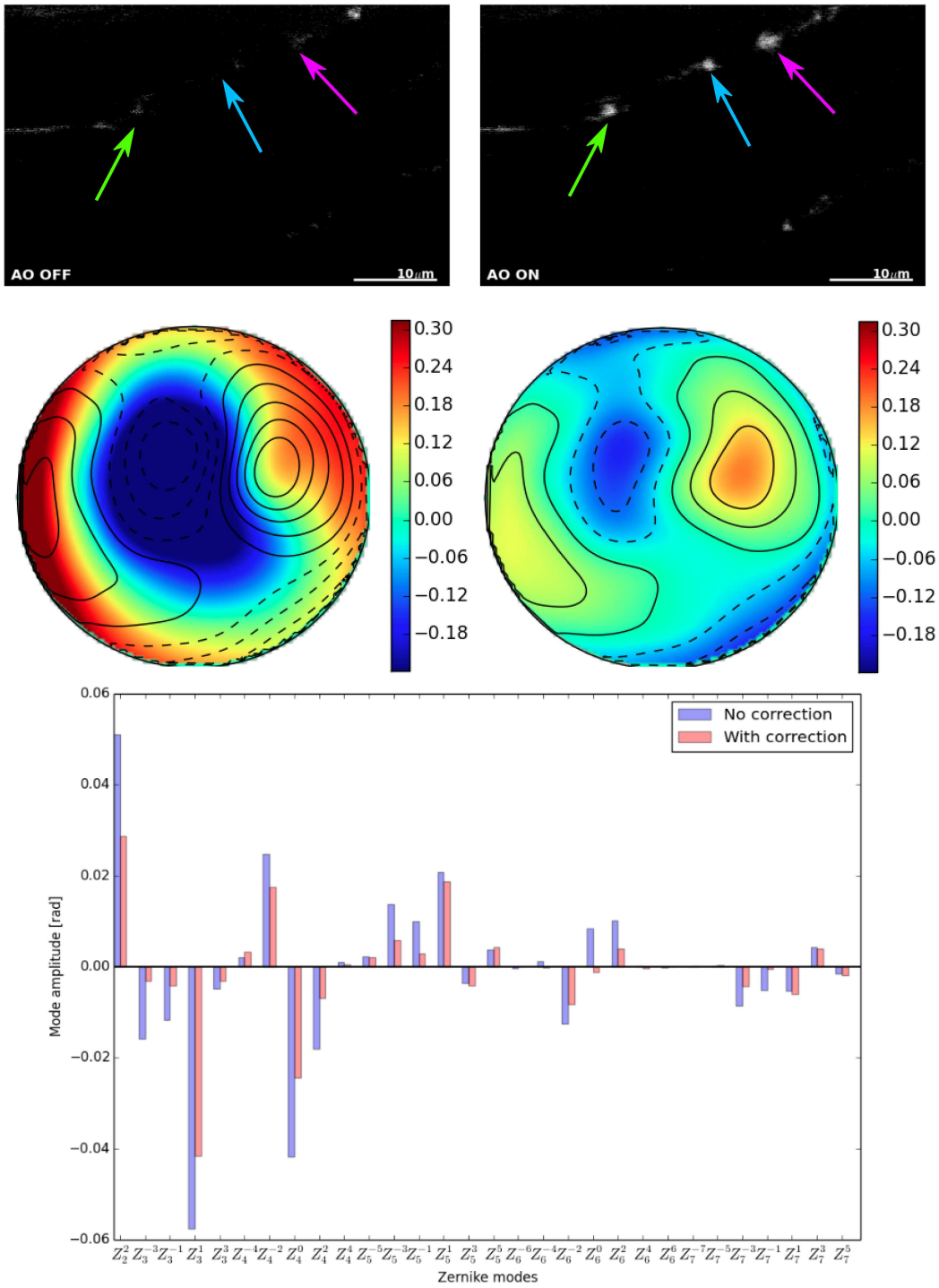


Figure 4.2: Sample made of agarose at 3% and a piece of leaf. **Top image:** confocal images without and with correction. The focal plane was at a depth of 206±0.5 μm. Light was reflected from chlorophyll cells that are found on the leaf surface. **Middle image:** image of reconstructed wavefronts surface (removed piston, tip, tilt and defocus terms). middle left-hand side: wavefront surface without correction. middle right-hand side: when the aberrations were corrected. **Bottom image:** Estimated Zernike coefficients amplitudes with and without correction, from term fifth up to 7^{th} order.

intercellular air (n ∼1.0) and others (Gausman & Allen (1973)).

Confocal images were obtained with and without corrections in this sample at four different planes (Δ_z ∼500 nm). For the first plane, the images are shown at the top of Figure 4.2. Chlorophyll can be easily identified on the corrected image (marked with arrows). The aberrations arising from the focal plane were sensed and the aberrated wavefront surface reconstructed (Figure 4.2, middle image, left-hand side). The reconstructed wavefront surface on the right-hand side corresponds to the residual aberrations after corrections. In both cases, the terms for piston, tip, tilt and defocus have been removed for the wavefront reconstruction. Zernike polynomials modes coefficients starting from vertical astigmatism (Z_2^2) up to the 7^{th} order are presented in the lower graph of Figure 4.2. The estimated coefficients amplitudes for orders higher than seven are almost negligible.

The wavefront RMS, visibility ($\frac{I_{\max}-I_{\min}}{I_{\max}+I_{\min}}$, if $I_{\min} = 0.0$ then $I_{\min} = 0.01$) and total image intensity for the corrected and non-corrected images were calculated. These values are presented in table 4.1, for the first plane only. When corrections are performed, an increase in the total image intensity together with better image contrast are attained. The corrected wavefront RMS is less than half of the original wavefront RMS.

The same correction coefficients were employed to record the confocal images for the other three planes (206.5 to 208 μm). Images of the SHWFS spots for the first plane are presented in Figure 4.3. Even though the spots for both images appear to be similar, there is an increase in the maximum intensity when the aberrations are corrected.

Although, other values obtained to correct the aberrations for the first plane were employed to correct the aberrations of the other planes as we moved deeper into the sample, good results were obtained for those planes. Variations in the values obtained for the wavefront RMS, spherical aberration (SA), visibility and total image intensity for the different planes can be observed in Figure 4.4. From the images small improvements in visibility and total image intensity for each plane can be considered, even though the same DM corrections were applied for each plane (those initially calculated for plane 0). For the RMS and SA values shown, it might be expected that an individual wavefront correction for every single focal plane inside the sample might produce a further reduction of their values. However, even without plane-by-plane correction, a small improvement in the resolution of the confocal images was achieved.

Sample: Agarose 3% and Red Edged Dracaena			
Parameter	**Without correction**	**With correction**	**Improvement**
RMS [rad]	0.1909	0.073	∼2.6×
Total Intensity [A.U]	43318	110699	∼2.6×
Visibility [A.U]	0.998	0.999	same

Table 4.1: Values obtained for wavefront root-mean square, visibility and total image intensity when confocal images were recorded with and without corrections at a depth of 206±0.5 µm,for samples made of agarose at 3% and Red-edged Dracaena leaf.

Three-dimensional images were generated using the confocal images obtained without and with corrections as we scanned deeper into the sample (Figure 4.5). Bigger differences in terms of image intensity can be noticed when aberrations are corrected.

For this particular sample, a relatively short exposure time for the SHWFS image (100 ms) was necessary in order to measure the aberrations. The total time required to measure, correct and notice changes in the confocal image was smaller than 2 min.

In order to introduce some refractive index variations in the sample in the interest of measuring stronger aberrations, a second specimen was prepared using agarose 1% and D-(+)-Glucose at 4% (3:1) and a piece of leaf of Red-edged Dracaena. In this sample, the first imaging plane was located at 63±0.5 µm deep into the sample. The light employed to sense the aberrations and to collect confocal images, was backscattered light from cell walls. A bright field image is presented in Figure 4.6. This image is presented to understand the origins of the backscattered light, even though the cellular wall is not well defined or clearly visible in the bright field image. The main component of the cell wall is cellulose, which has a refractive index n ∼1.466 (Gausman et al. (1974); Sultanova et al. (2013)).

Autofluorescence from structures in the sample was ruled out (cellulose: λ_{exc}: 320 nm, λ_{emi}: 420 nm, (Roshchina (2012); Olmstead & Gray (1993)). Once again, aberrations were mainly introduced in this case by planar-refractive index mismatch, structures within the leaf and the mix between agarose and D-(+)-Glucose.

The same procedure as previously described was carried out to measure, correct and collect images. Confocal images with and without correction as well as the wavefront surfaces are shown in Figure 4.7. When aberrations were corrected, the spot intensity for the SHWFS

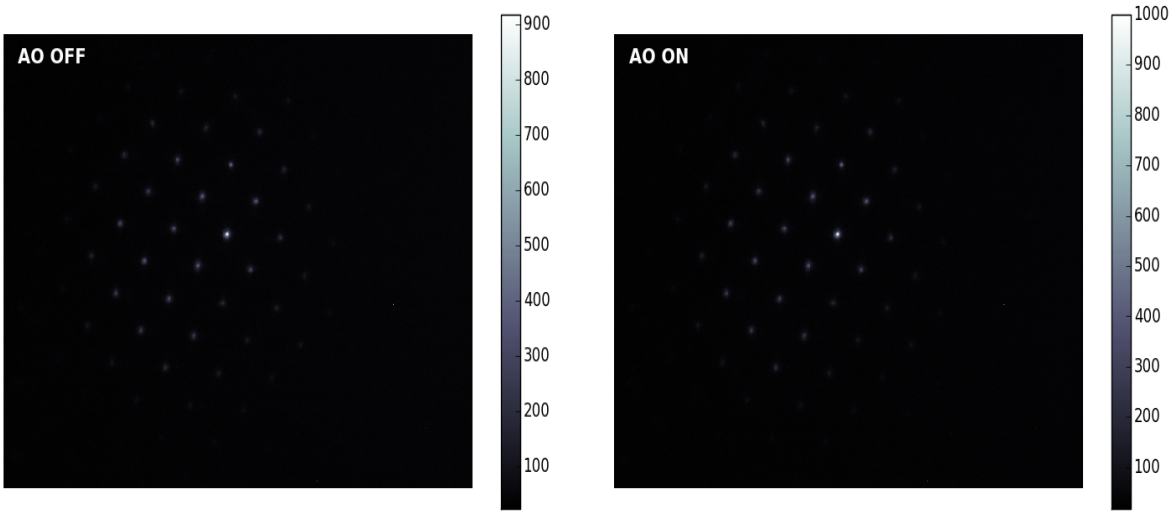


Figure 4.3: Shack-Hartmann spots when a sample of agarose 3% and a piece of Red-edged Dracaena was employed. The focal plane was situated 206±0.5 μm deep into the sample. When the system was correcting aberration, the intensity of the spots was higher for the corrected wavefront compared with the aberrated one. The distribution of the spots are similar, and only changes in the intensity of the spots are observed.

increased in value (Figure 4.8). Improvements on image total image intensity measured were attained (Figure 4.9). A similar behaviour was obtained for the RMS and spherical aberration coefficients values, hence, it is possible to infer that better results can be obtained if corrections are made for each plane individually. Comparisons for correction values obtained just for the first plane only are presented in table 4.2. An improvement in RMS and total image intensity of approximately ∼2.0× was achieved for this sample.

Differences in terms of total image intensity are visible when aberrations were corrected

Sample: Agarose 1%, Glucose 4% (3:1) and Red Edged Dracaena			
Parameter	**Without correction**	**With correction**	**Improvement**
RMS [rad]	0.1345	0.064	∼2.1×
Total Intensity [A.U]	131623	307891	∼2.3×
Visibility [A.U]	0.997	0.999	same

Table 4.2: Values obtained for wavefront root-mean square, visibility and total image intensity when confocal images were obtained with and without corrections at a depth of 63±0.5 μm, for a sample made of agarose at 1%, glucose 4% (3:1) and Red-edged Dracaena leaf.

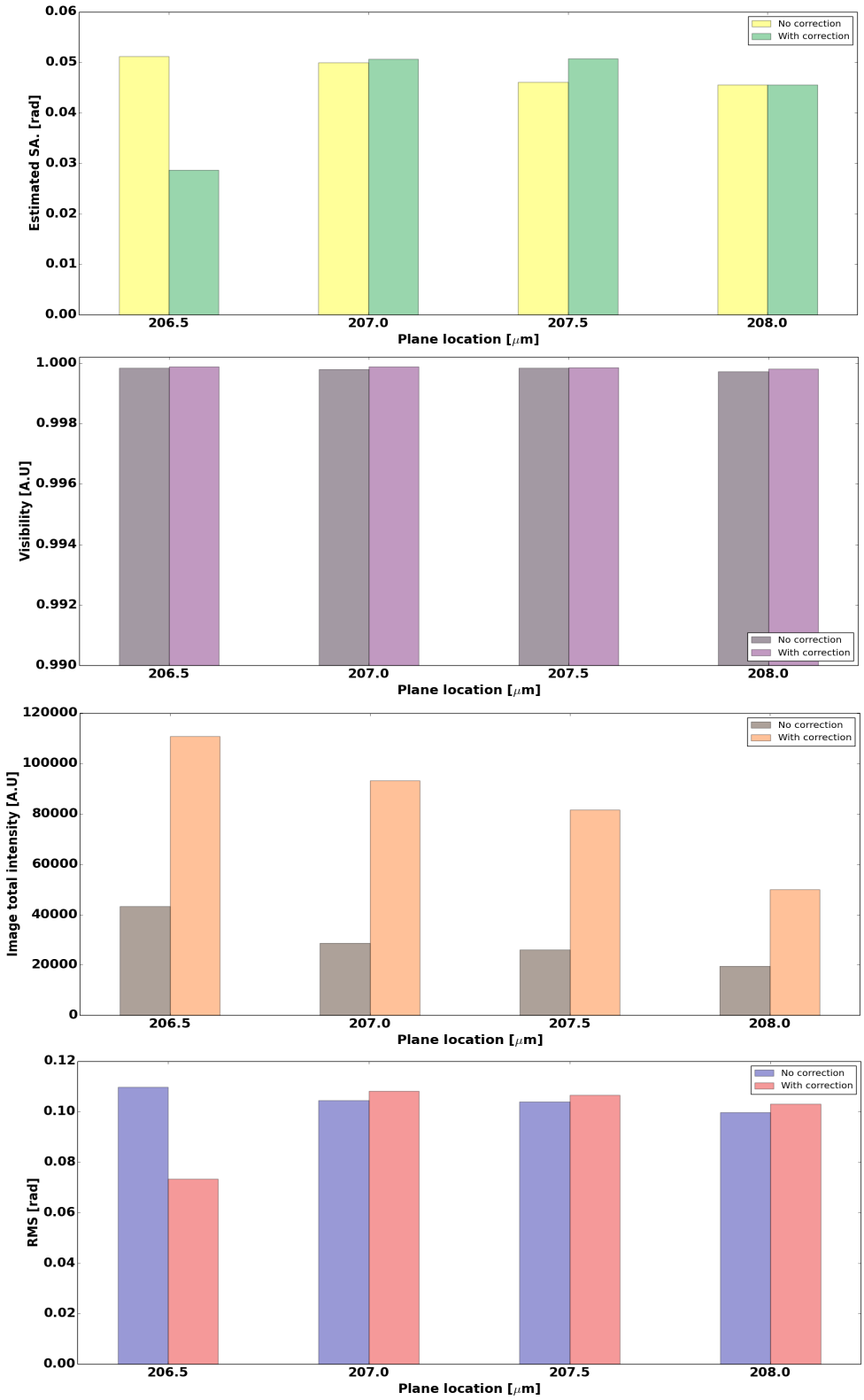


Figure 4.4: Values obtained for wavefront root-mean square, visibility and total image intensity when confocal images were obtained at four different focal planes in samples made of 3% agarose and a piece of leaf.

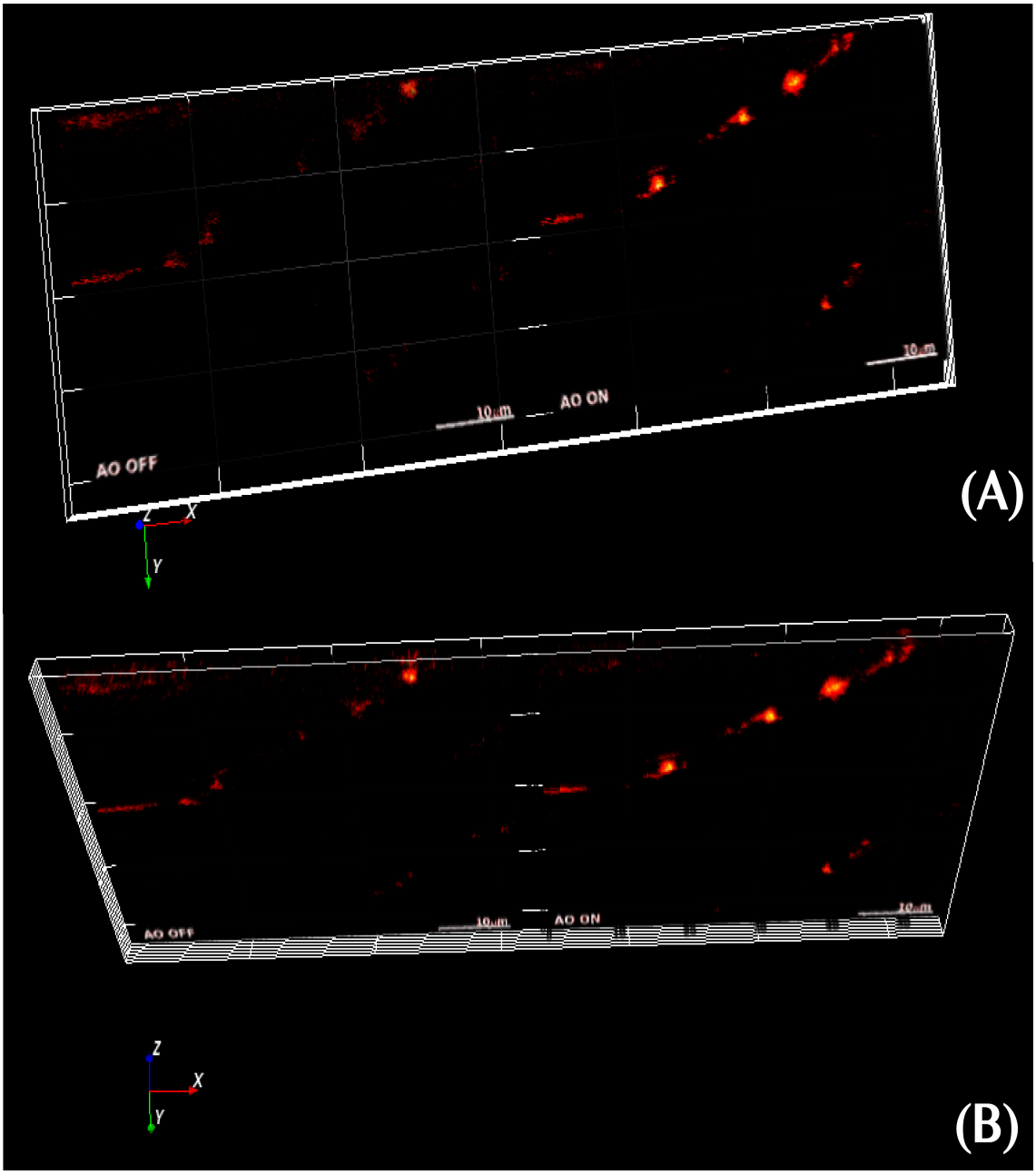


Figure 4.5: Three dimensional images for samples made of agarose at 3% and Red-edged Dracaena leaf. These images were generated using the software Icy.



Figure 4.6: Brightfield image of a sample made of agarose at 1% mixed with glucose at 4% (3:1)

in the three dimensional images obtained without and with corrections, this is shown in Figure 4.10.

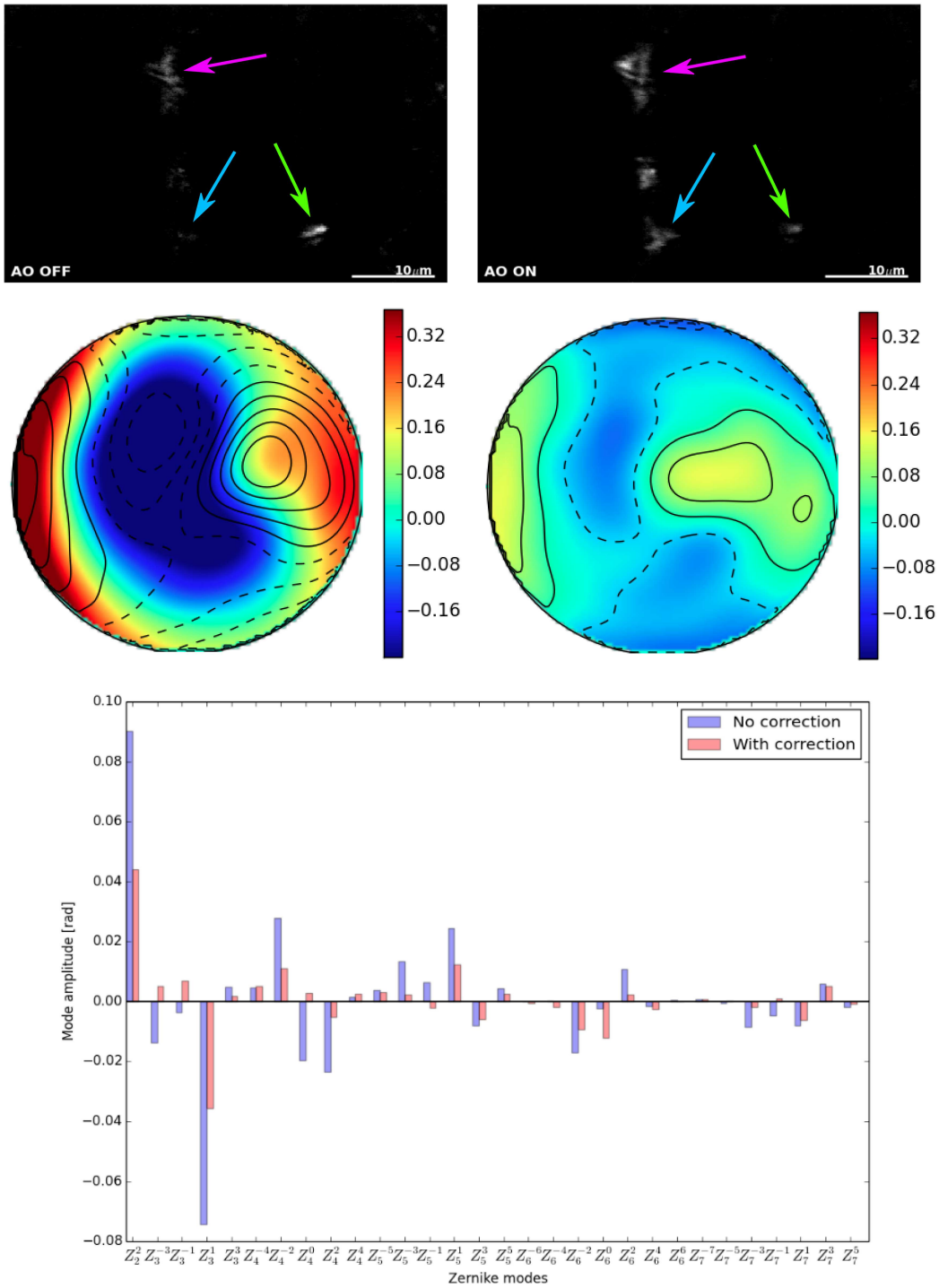


Figure 4.7: Sample made of agarose at 1% mixed with glucose at 4% (3:1). **Top image:** confocal images without and with correction. The focal plane was at a depth of 63±0.5 µm. Light was reflected by the cellular wall, which main component is cellulose. **Middle image:** image of reconstructed wavefront surfaces (removed piston, tip, tilt and defocus terms),left-hand side: without correction and on right-hand side when the aberrations were corrected. **Bottom image:** Estimated Zernike coefficients amplitudes with and without correction for high-order modes.

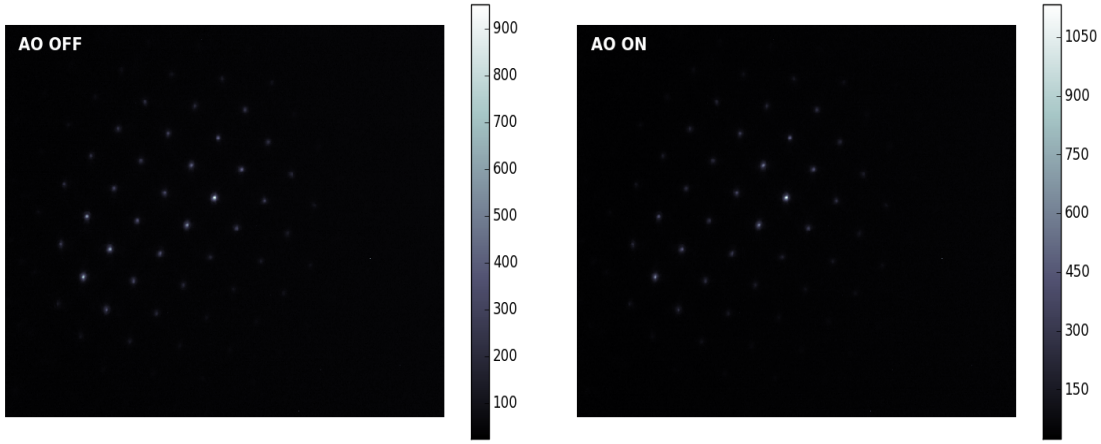


Figure 4.8: Shack-Hartmann sensor images obtained when a sample of agarose 1%, glucose 4% (3:1) and Red-edged Dracaena was employed. The distribution of the spots are similar, however, the maximum spot intensity is bigger when aberrations were corrected.

4.4 Correction of cell spheroid samples

The design and development of new drugs proceeds over many different trial stages. One such stage, preclinical testing, involves both *in-vitro* analysis in appropriate models, as well as *in-vivo* studies in relevant animal models. All these tests are carried out in order to determine the toxicity and other pharmacological characteristics fundamental in determining the basic safety and potential usefulness of a new drug. The number of pharmacological products that progress successfully throughout clinical development is quite low, around 10%. Due to the high cost of such trials, it is imperative that compounds that are potentially ineffective or have an unacceptable toxicity are dismissed as early as possible in the evaluation process. It is, therefore necessary to improve *in-vitro* based cell testing methods in order to sieve out poorly functioning drugs while prioritising promising candidates.

To achieve this, it is desirable to improve *in-vitro* assays to be more reliable in order to get relevant information. Thus, it is crucial that the samples used in these tests mimic as closely as possible the different parameters within the target tissue. 2D cell cultures are conventionally used in *in-vivo* drug candidates, however limitations of this type of culture suggest that an alternative method should be employed. One of the primary limitations encountered for 2D cultures is related to monolayer cultures and its lack of environmental realism. This is quite relevant with respect to studies relating to tumour biology, since solid tumours do not grow two-dimensionally, but rather in three dimensions. This is the reason

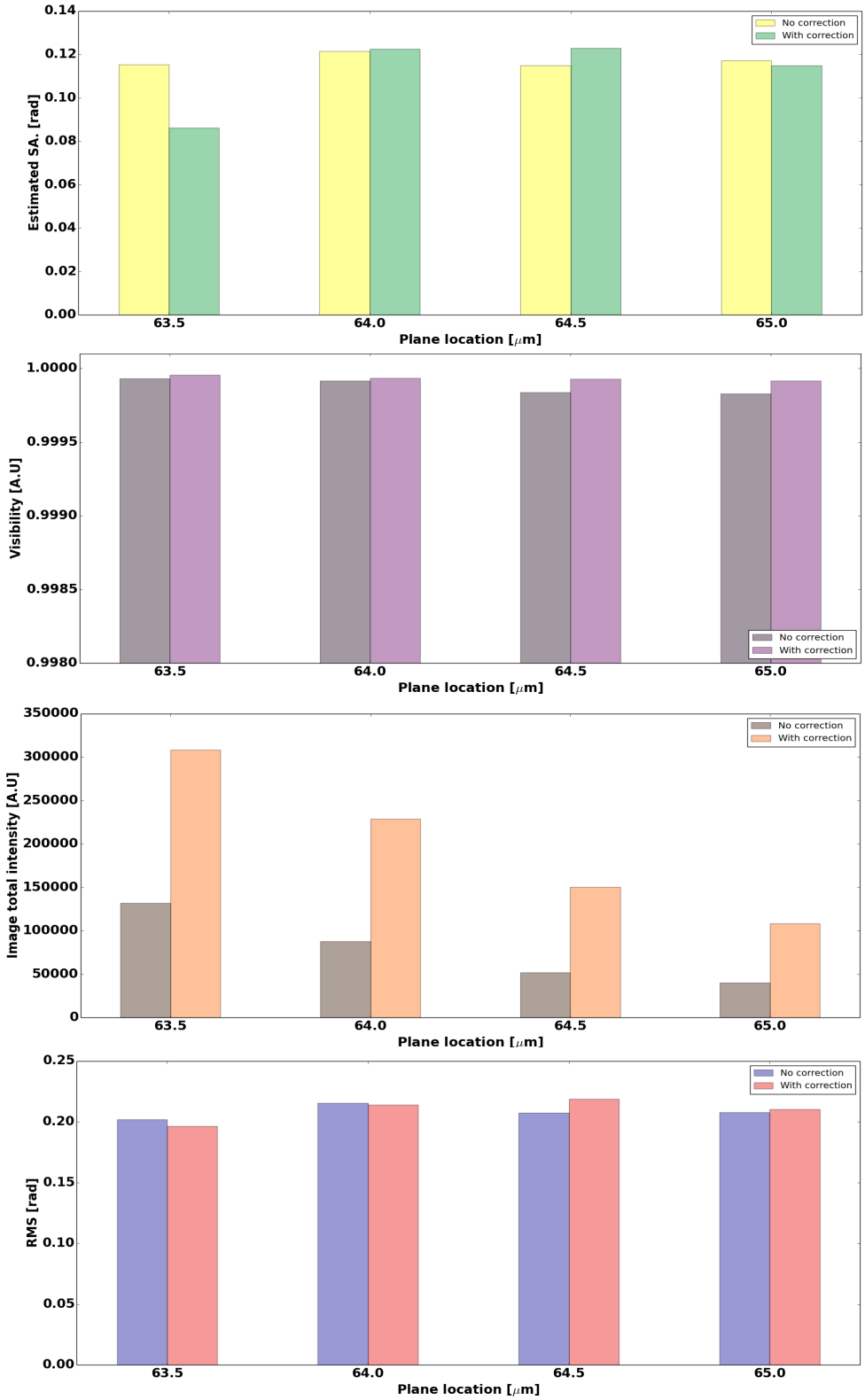


Figure 4.9: Values obtained for wavefront root-mean square, visibility and total image intensity when confocal images were obtained at four different focal planes in samples made of 1% agarose, 4% glucose (3:1) and a piece of leaf

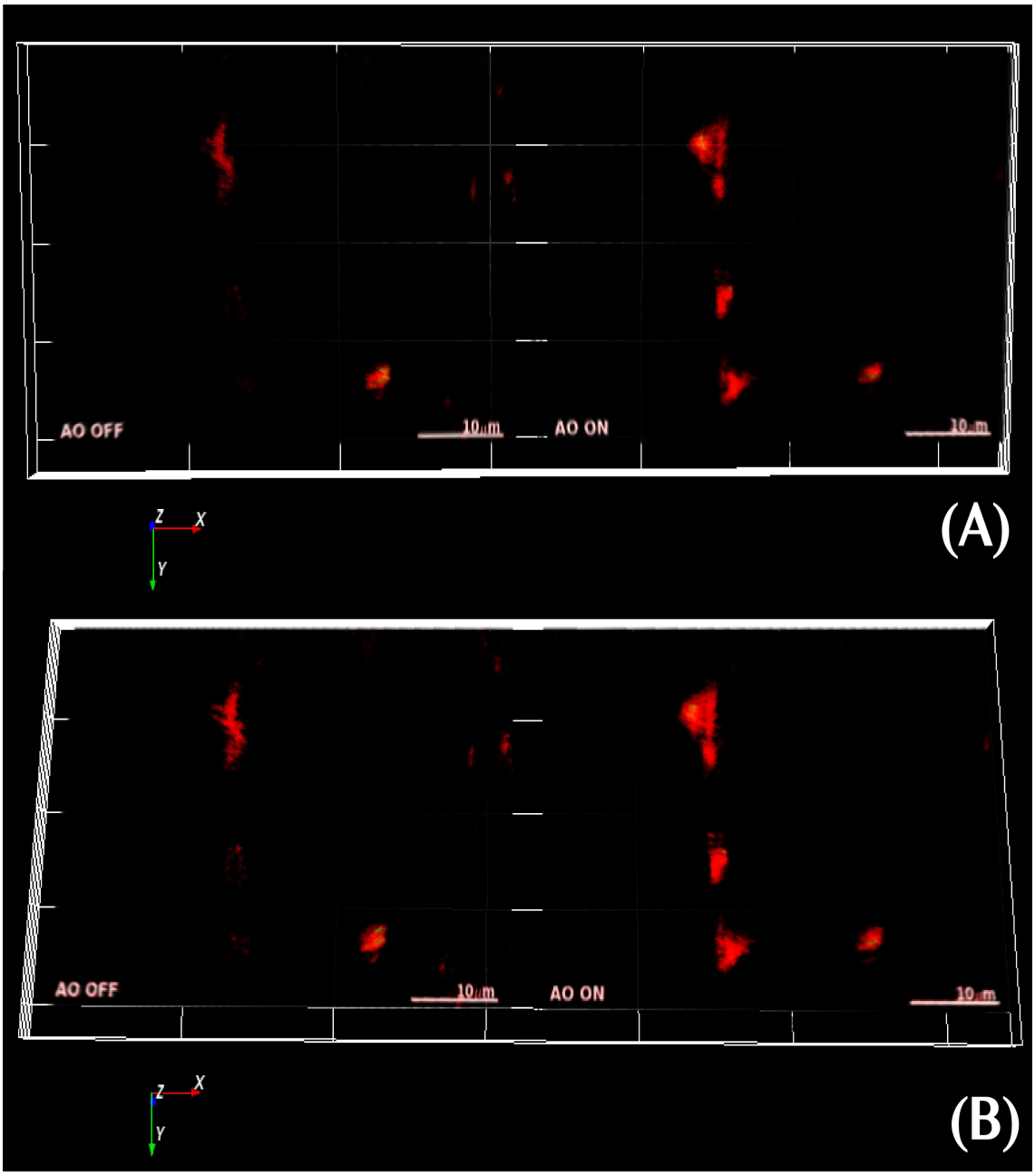


Figure 4.10: Three dimensional images for a sample made of agarose at 1%, glucose 4% (3:1) and Red-edged Dracaena leaf.

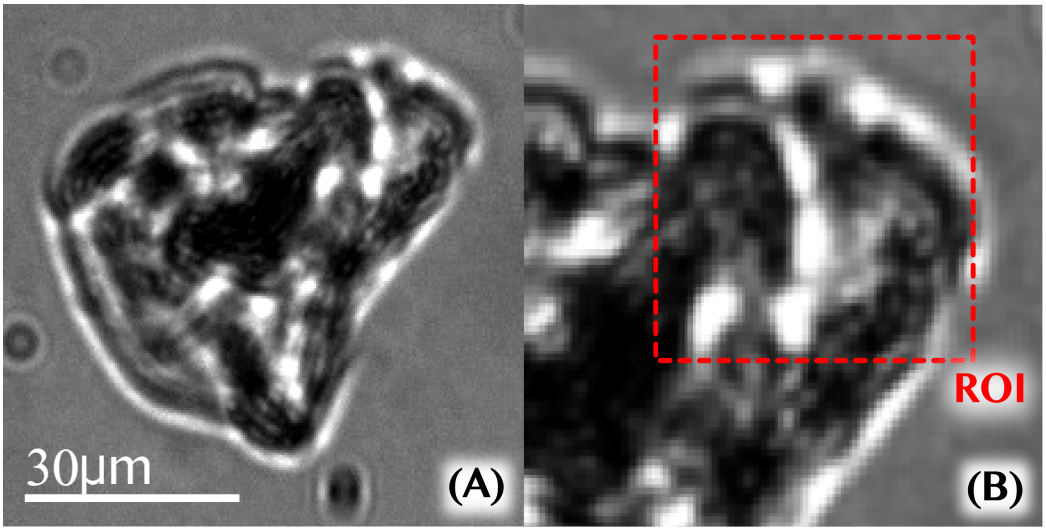


Figure 4.11: Brightfield images: (A) image of the whole spheroid. (B) Zoom to the area where we selected a region of interest to be imaged.

why strong efforts have been made in the development of various techniques (Hirschhaeusera & Menneb (2010); Breslin & ODriscoll (2013); Mehtaa et al. (2012); Santini et al. (2000)) for 3D cell culture. The use of this kind of samples to test our system, will allow us a better understanding of how the system will perform under more realistic conditions.

Cell spheroids were employed to test the system's ability to correct aberrations, these were made of HEKS293 cells. Although it may be impossible to achieve a generally-applicable procedure for spheroid culture, these samples were prepared following typical steps from cell-handling protocols to obtain highly reproducible spheroid cultures. The spheroids employed in our samples had diameters ranging between 50 to 200 µm. For imaging purposes and in order to avoid Brownian motion, the mounting medium employed was glycerol (n∼1.47). Samples were prepared using either a glass slide and n° 1.5 coverslip sealed with nail polish or with Petri dishes with a coverslip n° 1.5 in the base.

The first imaged sample was a spheroid made of HEKS293, human embryonic kidney cells. The bright field image of a spheroid is presented in Figure 4.11(A). A dashed red square was drawn to exhibit the region of interest (ROI) in a zoomed-in image of the spheroids (Figure 4.11(B)).

Wavefront corrections were implemented for the area presented in Figure 4.11(B). In this

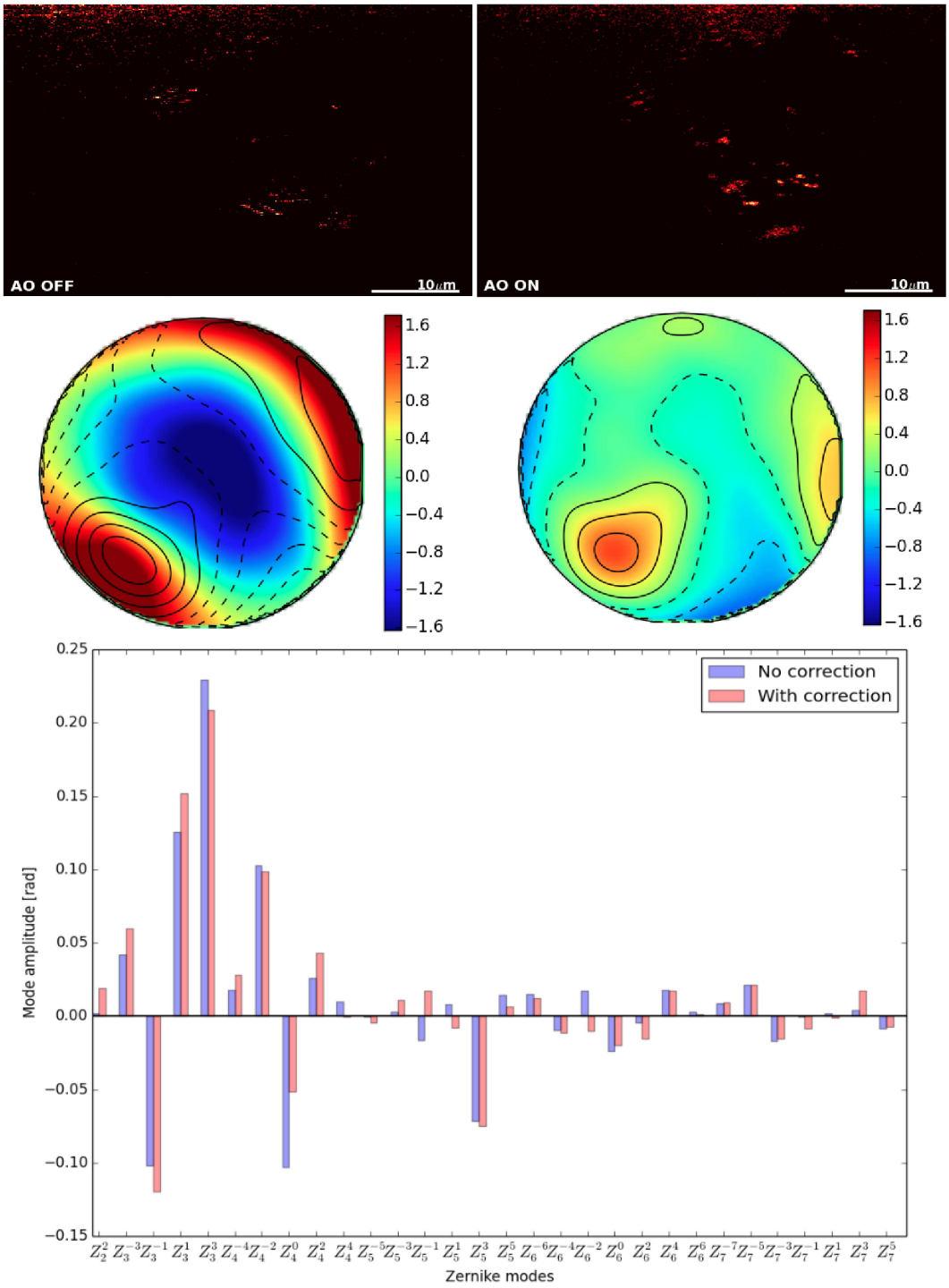


Figure 4.12: Spheroids made of human embrionic kidney cells. **Top image:** confocal images without and with correction. The focal plane was at a depth of 15±0.5 μm. **Middle image:** image of reconstructed wavefront surface (removed piston, tip, tilt and defocus terms), at right hand side when the aberrations were corrected. **Bottom image:** Estimated Zernike coefficients amplitudes with and without correction, from term fifth up to 7^{th} order.

Sample: HEKS #2 spheroid			
Parameter	**Without correction**	**With correction**	**Improvement**
RMS [rad]	0.5868	0.3761	∼1.6×
Total Intensity [A.U]	32986	62438	∼1.9×
Visibility [A.U]	0.996	0.998	same

Table 4.3: Values obtained for wavefront root-mean square, visibility and total image intensity when confocal images were obtained with and without corrections at a depth of 15±0.5 μm, for the HEKS spheroid.

sample measurements from only one focal plane were obtained. The light employed to sense the aberrations and to obtain the images corresponded to backscattered light from a layer made of cells located at a depth of 15±0.5 μm.

Confocal images were obtained without and with corrections; the obtained images are shown in Figure 4.12, (top images). On the corrected images, the light gathered corresponds to light reflected by the cell surfaces and other index-mismatch interfaces. The aberrated wavefront and the residual wavefront aberration surface after corrections are displayed in Figure 4.12 (middle image). Piston, tip, tilt and defocus have been removed from the wavefront surface reconstruction. Zernike polynomials coefficients starting from vertical astigmatism (Z_2^2) up to the 7^th order are presented in the lower graph of Figure 4.12. Coefficient amplitudes for order higher than seven are once again negligible. Aberrations in this type of sample arise primarily due to planar refractive index mismatch and sample structures, such as cell-cell and others (Santini et al. (2000))

In table 4.3, the values obtained for the RMS, visibility and total image intensity measured for the plane are presented. When aberrations were corrected an improvement slightly smaller than ∼2× in all these values were achieved.

Confocal images at deeper planes were not obtained with this sample due to the low light intensity collected and problems associated with image composition (related to the scanning process and image processing), as sometimes double images were obtained. The lack of structures in the sample, due to the low cell densities in the spheroids was the main cause of this problem. In order to image these kind of samples an improvement in the image processing technique is necessary. Especially a more robust process for low SNR samples would be required, however, this is not within the scope of this thesis. This problem can be appreciated in the confocal images presented above (Figure 4.12, top images) particularly

without correction. The presence of artefacts in the images are noticeable, such as the double image. In Figure 4.12, top left-hand side image, particularly on the lower right image quadrant, some double image might be notice. This has to do with image registration problems related to reverse interlacing. Further work is needed to avoid this problem in the future.

Morphological descriptions from these types of samples at this stage are to some extent imprecise. Bright areas in these images are mainly due to backscattered light from cell surfaces. On the other hand, for the case of dark areas it could be due to a lack of structures or even might be due to dead cells (Darzynkiewicz et al. (1997); Mulvey et al. (2009); Cheng et al. (2012)). To the best of our knowledge, this is the first time that images of spheroids have been obtained using only backscattered light. To better understand the morphology of these samples, more research is necessary.

In summary, wavefront correction using backscattered light from two different types of samples was achieved. The use of the correction obtained for the first plane imaged seems to be a reasonable approach when dealing with samples with long persistence times. Even though plane-by-plane correction was not implemented and small differences in the amount of wavefront RMS and spherical aberrations for planes deeper than the third plane were obtained, modest improvements were attained for visibility and total image intensity. Wavefront correction was achieved for the case of samples with low amount of structures, where the SNR was low.

So far the effect of the adaptive optics system was rather limited, it did yield an increase in the image signal intensity. However, any improvement in the resolution of the image was negligible.

Chapter 5

Summary

In this thesis, a new wavefront correction system based on direct wavefront sensing of backscattered light coming from the focal plane for a laser scanning confocal microscope was presented. Direct wavefront sensing was achieved with the use of a Shack-Hartman sensor. The Shack-Hartmann sensor is the most popular choice and it has been employed in other adaptive optics systems implemented in microscopy, mainly due to its simplicity. One of the problems addressed in this thesis, is related to the accuracy of this sensor. Any source of error in the determination of the centroid position will propagate to the wavefront reconstruction stage, reducing the performance of the system. We discussed the different algorithms generally employed for centroid estimation in a Shack-Hartmann sensor and compared one of these with the new algorithm that we implemented in this work.

The centroid algorithm that we presented in this thesis can be understood as a hybrid between a matched filter (Baker & Moallem (2007); Akondi & Vohnsen (2013); Leroux & Dainty (2010)) and a quasi-newtonian optimization algorithm (Press et al. (1992)). The product between a reference image or model (Gaussian mask) and the actual data was used as a cost function to be optimised. Optimisation was achieved by following the quasi-Newtonian method that involves a Taylor expansion of the cost function around an initial value close to the optimal value. As the expanded cost function does not correspond to a quadratic function, an iterative solution was required. The use of the first and second derivatives of this expansion play the main role in calculating the next iteration value. Computer generated data and real data obtained from a working AO system were used to compare the proposed algorithm performance versus a traditional centroid algorithm (CoG). Real data was acquired by recording different images of the Shack-Hartmann spots. These images

were obtained with different exposure times, laser intensities and using both biological and non-biological samples.

In the method that we presented, initial parameters are necessary to achieve convergence and to derive optimal values for the centroid positions. When data was simulated, the results obtained from applying the centre of gravity method were employed as the initial guesses. Even though sometimes the values obtained with CoG were not optimal values for initial parameters, as they were biased towards the image geometrical centre, good results were obtained.

From the results presented in this work, it can be seen that our method achieves better values than the CoG for both simulated and real scenarios. The approach yields good results considering that symmetric spots were assumed along the whole process. The method that we presented and implemented could be considered as the simplest version of this approach, as we assumed symmetric spots. More parameters could be included, such as different values for the Gaussian width in each orthogonal direction ($\sigma_x \neq \sigma_y$) and rotation angle, and this might achieve better centroid values. However, this may increase the time required per calculation reducing the ability of this method to be implemented on live systems.

Another problem that was addressed in this thesis was related to wavefront reconstruction, particularly how well a system will perform under less-than ideal conditions. These less than ideal conditions result from the inability to build a perfect wavefront sensor, where the accuracy is limited by the photon noise and the finite number of sampling areas, but also, the information employed as prior in the wavefront reconstruction. Prior information in astronomy has been widely studied and different experiments have confirmed that the atmosphere behaves according to Kolmogorov's theory (Dayton et al. (1992); Hickson (2014)) even though in some instances non-Kolmogorov behavior has been noted (Rao et al. (1999); Nicholls et al. (1995); Boreman & Dainty (1996)). However, in microscopy the phase structure of the samples is unknown. Addressing the problem associated to the lack of a general model for micro-optical properties of biological samples. (Schmitt & Kumar (1996)) used a phase-contrast microscope to measure the index variations spectrum of different samples. These exhibited a power law behaviour and their structure function was fitted with the Kolmogorov's model of turbulence. A similar behaviour was exhibited in human eyes (Cagigal et al. (2002)).

The problem associated with a lack of prior knowledge about the input wavefront was studied using an optimal reconstructor similar to the Wallner (1983) reconstructor. To assess the optimal reconstructor, the mean square error was evaluated. By generating different wavefont reconstructors with different aberration statistics the mean square error values were obtained.

From the results presented in this work, a difference in the values obtained for the MSE when the input wavefront statistics matched the prior ($\alpha_0 = \alpha_{\mathrm{R}}$) was observed. Generally in this particular case the minimum error value was registered, then, this can be considered as the optimal reconstructor. The optimal reconstructor will always lead to the minimum error attainable, even for low SNR values as 1. Also, from the results, the use of different priors in the reconstructor, led to bigger MSE error value as these values moved further from the optimal. For those cases when $\alpha_0 \neq \alpha_{\mathrm{R}}$, the value obtained for the error depended on which value was employed as the prior in the reconstructor. From the results, when $\alpha_R > \alpha_0$ the error value decreased, specially at high SNR value, but these were not comparable to the values obtained when $\alpha_R < \alpha_0$. From the results it was possible to infer that the wavefront reconstruction process should have a good performance (low error value) for α_R larger than 2.33.

As prior information of the wavefront statistics is not known the aim was to try to avoid possible prior values that could lead to a reduction in the system's performance. We found and defined a range of prior values between 2.33 and 3.67 where a better performance could be achieved for the whole range of possible input wavefront options.

From the results obtained, a reconstructor following a wavefront statistics equal to $\alpha_{\mathrm{R}} = 3.0$ seems to be the best option to be implemented, specially for SNR values higher than 4, as the error values observed in this case were small for the whole range of possible input wavefronts. The use of this value also agrees with different samples that exhibited a power law behaviour on the variation of their refractive indices. These results are important in microscopy, where we do not have real prior information about the aberration statistics being observed. Therefore, if some aberration statistics would be inherently more likely than others, there are some reason to pick up one reconstructor over another, particularly at low SNR values. In this case the most suitable solution for the problem of wavefront reconstruction would seem to be a reconstructor that can perform efficiently over a wider range of different input wavefront statistics.

Wavefront corrections were performed for different samples. Samples made of fresh agarose and leaves were employed, together with cell spheroids made of HEKS293 cells. In both cases, wavefront correction using backscattered light was achieved. Even though plane-by-plane correction was not implemented and small differences in the amount of wavefront RMS and spherical aberrations for planes deeper than third plane were obtained, modest improvements were attained for visibility and total image intensity. Wavefront correction was achieved for the case of samples with low amount of structures, where the SNR was low. So far the effect of the adaptive optics system was rather limited, it did yield an increase in the image signal intensity. However, any improvement in the resolution of the image was negligible.

Finally, further improvements to the system can be implemented, particularly the use of a source with a higher output for the illumination light, objectives with higher numerical apertures and a stronger method to avoid registration problems related to reverse interlacing for the confocal image.

Chapter 6

Conclusions

In this thesis, we studied adaptive optics corrections using direct wavefront sensing by means of a Shack-Hartmann sensor. This was done by using just backscattered light measured from different samples.

The use of backscattered light represents a challenge, as only a small part of the light that is backscattered carries the information from the imaging plane that we desire to image and correct. The approach that we present, requires a small variation in the setup to those systems that already have employed a Shack-Hartmann sensor and mainly use fluorescent probes. The use of an extra relay and a pinhole in the wavefront sensing path, allows us to reject out-of-focus light that affects the information gathered by the Shack-Hartmann sensor. Wavefront correction at different sample depths is achieved as the pinhole used at the wavefront sensing path is located at a conjugate plane to the focal spot. This setup allows fluorescent and non-fluorescent samples to be investigated.

In order for an adaptive optics system to work, different stages or processes need to work well in conjunction with each other. The wavefront sensing process, control stage and the corrector need to be developed to achieve the final goal. Throughout this work, improvements for each of these processes were made, by considering the nature of the system.

In the wavefront sensing process, the implementation of a pinhole of the right diameter to reject out-of-focus light, a problem that might not be encountered when fluorescent light is employed, was considered. Compared to other methods that relied on backscattered light to measure the aberrations, such as coherent gated wavefront sensing, our system is easier to

implement. Pinhole size selection plays an important role in the amount of light measured by the sensor. A small pinhole will reject out-of-focus light but will also lead to rejection of valuable information that is required to truly measure the aberrations. On the other hand, a pinhole which is too big will allow not only the valuable wavefront information to be measured, but it also allow out-of-focus light which will contaminate the signal. In this case, the wavefront aberration measured will not be fully meaningful. As pinhole selection size was not fully investigated in this work, our attention was turn to deal with this out-of-focus light, particularly at the centroid position estimation for the Shack-Hartmann sensor.

Out-of-focus light will be added to the light gathered by the Shack-Hartmann sensor and in our case it will be considered as background. These signals will lead to errors in the estimated centroid position, particularly by biasing the centroid to the geometrical image centre. This affected the system's performance as these errors will propagate throughout the rest of the system. To handle this background light we proposed a centroid algorithm that should efficiently reject this type of information. The method that we used to investigate this problem was based on the optimisation of the product between the data and a spot model. Computer generated data and also real data obtained from the system that we built was employed to test the centroid algorithm. Good centroid estimation values were obtained in both cases and these values were better than those obtained with one of the traditional methods employed with Shack-Hartmann sensors.

The next improvement was carried out at the control stage, with the meaningful spot centroid measurements, the next step was to obtain a phase profile as accurate as possible to the unknown wavefront sensed, following a modal method. In this case, we decided to avoid the least-square method that has already been implemented in other applications, including microscopy. Then, in order to get a better reconstructor, the use of prior knowledge was included. It is generally assumed that aberrations do not vary significantly across the field of view being imaged. Starting from this idea, that aberration in microscopy can be considered as translation invariant, we tackle one of the several problems that can be found in this situation. Different samples will have different structures with different shapes, sizes and refractive indices. The question that arises is which is the best model to describe the aberrations introduced by the samples. In contrast to astronomy, where aberrations introduced by the atmosphere can be measured and turbulence models to describe these are available, in microscopy this is not a easy problem to solve. Attempts to fit models to sample aberrations, particularly by using Kolmogorov's model of turbulence can be found. However, due to the

nature of the problem, this is not fully conclusive. If we want to implement a reconstructor that uses prior knowledge in our system, it is necessary to use a prior that will not affect the system's performance. This problem can be alleviated, by investigating possible models that could introduce more or less error in the reconstruction stage. The idea is to find those prior values that would lead to smaller error in the reconstructor stage along the whole range of possible wavefront statistics that can be encountered. This was done by generating different wavefront statistics as input wavefronts and these were reconstructed by using the same or different priors, at different signal-to-noise ratios. From this, it was possible to find a range of values where the error obtained was small and gave reasonable error values along the whole range of possible input wavefronts.

Having a good centroid estimation position and good wavefront reconstruction, the next system improvement was related to the corrector and the signals that drive this element. System performance can be increased slightly by restricting the values that drive this element, to the range of values that the corrector can accept. For this a linear least-square solver (LLSP) method was implemented. This allowed a better use of the mirror, avoiding actuator clipping or saturation, that will lead to errors in the correction loop, decreasing the system performance.

All the improvements done at the wavefront sensing stage, reconstructor and corrector were implemented in a home-written software. This software together with the system built around an inverted microscope that included a wavefront sensing path and a deformable mirror as a corrector element was used to test two different samples. Thick samples made of leaves in agarose, leaves in agarose and glucose and cell spheroids were imaged. Wavefront aberrations measurements were performed at different depths depending on the sample employed. Even though the effect of the adaptive optics system was rather limited, and any improvement in the resolution of the image was negligible, it did yield an increase in the confocal image signal intensity obtained. Smaller values for the wavefront Zernike coefficients and RMS were obtained, demonstrating that the system is able to perform wavefront corrections using just backscattered light.

The work presented on this thesis could be considered as an alternative to coherent-gated wavefront sensing techniques, especially if minimum changes wants to be done over a system, particularly in terms of the number of components employed in its implementation. It also presents the option to avoid the use of fluorescent probes to measure aberrations and

leave these probes to be employed 100% for their pure biological purpose, e.g. to imaging calcium in neurons. In this case if backscattered light is employed to measure aberrations and these signals are used to correct them we avoid the unnecessary photo-bleaching from the probes when imaging the neurons, improving the signal-to-noise ratio. Considering the area of osteoarthritis research, this method could help to study cells within connective tissue. These tissues are ideally suited for cell visualization, as cell density is relatively low and the cells are clearly visible against the extra-cellular matrix. Particularly, chondrocytes, that are cells that can only be found in healthy cartilage and correspond to approximately 5% of articular cartilage constituents. Little is known in situ about their physiology, either in healthy or degenerated cartilage, especially when they have to do with the initiation and progression of osteoarthritis. Even though these cells can be studied by isolating them, it is not the same. Then, the technique proposed by us will allow to image deeper into volumetric samples, removing possible artefacts obtained when cutting surfaces to make the samples.

This work represents the first attempt to develop a fully functional laser scanning confocal microscope with direct wavefront sensing using just backscattering. Then, different new problems can be addressed in the future, following the same research line. More research is necessary particularly in the problem associated with the pinhole size diameter employed in the wavefront sensing path. The pinhole diameter that we used, can be considered as a good value for an open-loop system, but this value can probably be improved further. This, as once close-loop is achieved, the point spread function for the lens that we are using to pass through the pinhole might be aberration free, then reducing its diameter to its diffraction-limited size. If this happens, out-of-focus light will pass through the pinhole, affecting once again the light gathered by the Shack-Hartmann wavefront sensor. Another area to be exploited is related to the use of objectives with high numerical apertures. Even when more light can be gathered by these objectives, a drawback associated to these is related to the longer distances that the light needs to travel inside the samples towards the focal spot, then, the amount of aberrations measured in these cases is expected to be higher. Changes to the corrector device or the Shack-Hartmann lenslet array may be required in this case, as the aberration may be too big to be corrected by the dynamic range of the corrector or more lenslets might be required to get a better measurement of the aberrations. Others techniques have already been studied in the field of astronomy, could also be considered for their implementation in this type of equipment, this technique is known as multi-conjugate adaptive optics (MCAO). The idea behind MCAO is to reduce the possible sample anisoplanatism (the absence of spatial invariance over an extended field-of-view), hence increasing the compensated field-of-view.

Bibliography

Abramowitz, M., & Stegun, I. A. 1964, Handbook of Mathematical Functions with Formulas, Graphs, and Mathematical Tables, ninth dover printing, tenth gpo printing edn. (New York: Dover)

Akondi, V., & Vohnsen, B. 2013, Opthalmic and Physiological Optics, 33, 434

Albert, O., Sherman, L., Mourou, G., Norris, T. B., & Vdovin, G. 2000, Optics Letters, 25, 52

Artal, P., Iglesias, I., López-Gil, N., & Green, D. G. 1995, Journal of the Optical Society of America A, 12, 2358

Baker, K. L., & Moallem, M. M. 2007, Optics Express, 15, 5147

Bakut, P. A., Kirakosyants, V. E., Loginov, V. A., Solomon, C. J., & Dainty, J. C. 1994, Optics Communications, 109, 10

Bará, S., Pailos, E., & Arines, J. 2012, Optics Letters, 37, 2427

Biwas, T. K., & Gupta, A. K. 2002, Indian Journal of Radiology and Imaging, 12, 169

Booth, M. 2006, Optics Express, 14, 1339

Booth, M., Neil, M., & Wilson, T. 1998, Journal of Microscopy, 192, 90

Booth, M., & Wilson, T. 2000, Journal of Microscopy, 200, 68

Booth, M. J. 2007a, Philosophical Transactions of the Royal Society of London A: Mathematical, Physical and Engineering Sciences, 365, 2829

—. 2007b, Optics Letters, 32, 5

Booth, M. J., Neil, M. A. A., Juskaitis, R., & Wilson, T. 2002, Proceedings of the National Academy of Sciences, 99, 5788

Boreman, G. D., & Dainty, C. 1996, Journal of the Optical Society of America A, 13, 517

Box, G., & Tiao, G. 1973, Bayesian inference in statistical analysis, Addison-Wesley series in behavioral science: quantitative methods (Addison-Wesley Pub. Co.)

Breslin, S., & ODriscoll, L. 2013, Drug Discovery Today, 18, 240

Brovko, L. 2010, Bioluminescence and fluorescence for in vivo imaging, Tutorial texts in optical engineering (Bellingham, Wash. SPIE Press)

Bueno, J. M., Gualda, E. J., & Artal, P. 2010, Journal of Biomedical Optics, 15, 066004

Bueno, J. M., Vohnsen, B., Roso, L., & Artal, P. 2009, Applied Optics, 48, 770

Cagigal, M. P., Canales, V. F., Castejón-Mochón, J. F., Prieto, P. M., López-Gil, N., & Artal, P. 2002, Optics Letters, 27, 37

Cha, J. W., Ballesta, J., & So, P. T. C. 2010, Journal of Biomedical Optics, 15, 046022

Cheng, N.-C., et al. 2012, Biomed. Opt. Express, 3, 2111

Chew, T. Y., Clare, R. M., & Lane, R. G. 2006, Optics Communications, 268, 189

Conn, M. P. 2010, Techniques in Confocal Microscopy, First Edition (Elsevier, Academic Press)

Cubalchini, R. 1979, Journal of the Optical Society of America (1917-1983), 69, 972

Dai, G.-M. 1996, Journal of the Optical Society of America A, 13, 1218

Darzynkiewicz, Z., Juan, G., Li, X., Gorczyca, W., Murakami, T., & Traganos, F. 1997, Cytometry, 27, 1

Dayton, D., Person, B., Spielbusch, B., & Gonglewski, J. 1992, Optics Letters, 17, 1737

Débarre, D., Botcherby, E. J., Watanabe, T., Srinivas, S., Booth, M. J., & Wilson, T. 2009, Optics Letters, 34, 2495

Diaz-Santana, L., Walker, G., & Bará, S. X. 2005, Optics Express, 13, 8801

Dixon, A. L., & Ferrar, W. L. 1930, Quart. J. Math., Oxford Ser., 1, 122145

Egger, M. D., & Davidovits, P. 1973, Nature, 244

Egner, A., & Hell, S. W. 1999, Journal of Microscopy, 193, 244

Facomprez, A., Beaurepaire, E., & Débarre, D. 2012, Optics Express, 20, 2598

Feierabend, M. 2004, PhD thesis, University of Heidelberg, Heidelberg, Germany

Feierabend, M., Rückel, M., & Denk, W. 2004, Optics Letters, 29, 2255

Fernandez, E. J., & Artal, P. 2003, Optics Express, 11, 1056

Freund, I., Rosenbluh, M., & Feng, S. 1988, Physical Review Letters, 61, 2328

Fried, D. L. 1977, Journal of the Optical Society of America (1917-1983), 67, 370

Fusco, T., Conan, J.-M., Michau, V., Mugnier, L. M., & Rousset, G. 1999, Opt. Lett., 24, 1472

Gausman, H. W., & Allen, W. A. 1973, Plant Physiology, 52, 57

Gausman, H. W., Allen, W. A., & Escobar, D. E. 1974, Applied Optics, 13, 109

Gualda, E. J., Bueno, J. M., & Artal, P. 2010, Journal of Biomedical Optics, 15, 026007

Hardy, J. 1998, Adaptive Optics for Astronomical Telescopes, Oxford series in optical and imaging sciences (Oxford University Press)

Hardy, J. W. 1978, IEEE Proceedings, 66, 651

Herriot, G., et al. 2000, in Adaptive Optical Systems Technology, ed. P. L. Wizinowich, Vol. 4007, 115–125

Herrmann, J. 1980, Journal of the Optical Society of America (1917-1983), 70, 28

Hickson, P. 2014, The Astronomy and Astrophysics Review, 22, 1

Hirschhaeusera, F., & Menneb, H. e. a. 2010, Journal of Biotechnology, 148, 3

Hudgin, R. H. 1977, Journal of the Optical Society of America (1917-1983), 67, 375

Hunt, B. R. 1979, Journal of the Optical Society of America (1917-1983), 69, 393

Irwan, R., & Lane, R. G. 1999, Applied Optics, 38, 6737

Ji, N., Milkie, D., & Betzig, E. 2010, Nature Methods, 7, 141

Kam, Z., Kner, P., Agard, D., & Sedat, J. W. 2006, Journal of Microscopy, 226, 33

Kong, L., & Cui, M. 2015, Optics Express, 23, 6145

Korff, D., Dryden, G., & Leavitt, R. P. 1975, Journal of the Optical Society of America (1917-1983), 65, 1321

Law, N. F., & Lane, R. G. 1996, Optics Communications, 126, 19

Lee, Y., Lee, S., Ivrissimtzis, I., & Seidel, H.-P. 2006, in Symposium on Geometry Processing, ed. A. Sheffer & K. Polthier (The Eurographics Association)

Leroux, C., & Dainty, C. 2010, Optics Express, 18, 1197

Li, J., Zhang, Z., Gao, J., Sun, J., & Chen, W. 2016, Optics Communications, 359, 254

Lombardo, M., Serrao, S., Devaney, N., Parravano, M. c., & Lombardo, G. 2013, Sensors, 13, 334

Malacara, D. 2007, Optical Shop Testing (Wiley Series in Pure and Applied Optics) (Wiley-Interscience)

Marchetti, E., et al. 2005, Comptes Rendus Physique, 6, 1118

Mehtaa, G., Hsiaoa, A., & Ingramc, M. 2012, Journal of Controlled Release, 164, 192

Minsky, M. 1961, Microscopy apparatus, uS Patent 3,013,467

Mulvey, C. S., Sherwood, C. A., & Bigio, I. J. 2009, Journal of Biomedical Optics, 14, 064013

Neil, M. A. A., Juškaitis, R., Booth, M. J., Wilson, T., Tanaka, T., & Kawata, S. 2000, Journal of Microscopy, 200, 105

Nicholls, T. W., Boreman, G. D., & Dainty, J. C. 1995, Optics Letters, 20, 2460

Nicolle, M., Fusco, T., Rousset, G., & Michau, V. 2004, Optics Letters, 29, 2743

Noll, R. J. 1976, Journal of the Optical Society of America (1917-1983), 66, 207

Olmstead, J. A., & Gray, D. G. 1993, Journal of Photochemistry and Photobiology A: Chemistry, 73, 59

Pailos, E., & Bará, S. 2014, Optics Letters, 39, 3197

Paterson, C., Munro, I., & Dainty, J. C. 2000, Optics Express, 6, 175

Pawley, J. B. 2006, Handbook of Biological Confocal Microscopy, 3rd edn. (University of Wisconsin, Madison: Springer)

Platt, B. C., & Shack, R. 2001, Journal of Refractive Surgery, 17

Poyneer, L. A. 2003, Correlation Wave-Front Sensing Algorithms for Shack-Hartmann-Based Adaptive Optics using a Point Source

Press, W. H., Teukolsky, S. A., Vetterling, W. T., & Flannery, B. P. 1992, Numerical Recipes in C (2Nd Ed.): The Art of Scientific Computing (New York, NY, USA: Cambridge University Press)

Prieto, P. M., Vargas-Martín, F., Goelz, S., & Artal, P. 2000, Journal of the Optical Society of America A, 17, 1388

Rahman, S. A., & Booth, M. J. 2012, in MEMS Adaptive Optics VI, Vol. 8253, 82530I

Rao, C., Jiang, W., & Ling, N. 1999, in Propagation and Imaging through the Atmosphere III, ed. M. C. Roggemann & L. R. Bissonnette, Vol. 3763, 84–91

Rimmer, M. P. 1974, Applied Optics, 13, 623

Roddier, F., ed. 1999, Adaptive Optics in Astronomy (Cambridge University Press), cambridge Books Online

Roddier, N. 1990, Optical Engineering, 29, 1174

Roggemann, M., Welsh, B., & Hunt, B. 1996, Imaging Through Turbulence, Laser & Optical Science & Technology (Taylor & Francis)

Roopashree, M. B., Akondi, V., & Raghavendra, B. P. 2011a, International Journal of Latest Trends in Engineering and Technology, 6, 52

Roopashree, M. B., Vyas, A., & Prasad, B. R. 2011b, in American Institute of Physics Conference Series, Vol. 1391, American Institute of Physics Conference Series, ed. P. Predeep, M. Thakur, & M. K. R. Varma, 312–314

Roshchina, V. 2012, International Journal of Spectroscopy, 2012, 14

Rueckel, M., & Denk, W. 2006, in APS Meeting Abstracts, 29005

Rueckel, M., & Denk, W. 2007, Journal of the Optical Society of America A, 24, 3517

Sallberg, S. A., Welsh, B. M., & Roggemann, M. C. 1997, Journal of the Optical Society of America A, 14, 1347

Santini, M. T., Rainaldi, G., & Indovina, L. P. 2000, Critical reviews in Oncology/Hematology, 36, 75

Sasiela, R. J., & Mooney, J. G. . 1986, in Society of Photo-Optical Instrumentation Engineers (SPIE) Conference Series, Vol. 551, 170–176

Sauvage, J.-F., Fusco, T., Rousset, G., & Petit, C. 2007, Journal of the Optical Society of America A, 24, 2334

Schmitt, J. M., & Kumar, G. 1996, Optics Letters, 21, 1310

Schwertner, M., Booth, M. J., & Wilson, T. 2004, Journal of Microscopy, 217, 184

Shaw, M., O'Holleran, K., & Paterson, C. 2013, Optics Express, 21, 19353

Shengyang, H., Yu, N., Fengjie, X., & Zongfu, J. 2013, Optics Communications, 288, 7

Sheppard, C. J. R., & Gu, M. 1991, Applied Optics, 30, 3563

Sherman, L., Ye, J. Y., Albert, O., & Norris, T. B. 2002, Journal of Microscopy, 206, 65

Solomon, C., & Breckon, T. 2011, Fundamentals of digital image processing : a practical approach with examples in Matlab (Chichester, West Sussex, UK: Wiley-Blackwell)

Southwell, W. H. 1980, Journal of the Optical Society of America (1917-1983), 70, 998

Sultanova, N. G., Kasarova, S. N., & Nikolov, I. D. 2013, Optical and Quantum Electronics, 45, 221

Tanabe, A., Hibi, T., Ipponjima, S., Matsumoto, K., Yokoyama, M., Kurihara, M., Hashimoto, N., & Nemoto, T. 2015, Journal of Biomedical Optics, 20, 101204

Tao, X., Azucena, O., Fu, M., Zuo, Y., Chen, D. C., & Kubby, J. 2011a, Optics Letters, 36, 3389

Tao, X., Fernandez, B., Azucena, O., Fu, M., Garcia, D., Zuo, Y., Chen, D. C., & Kubby, J. 2011b, Optics Letters, 36, 1062

Thayil, A., & Booth, M. J. 2011, Journal of the European optical society, 6

Thomas, S. 2004, in Advancements in Adaptive Optics, ed. D. Bonaccini Calia, B. L. Ellerbroek, & R. Ragazzoni, Vol. 5490, 1238–1246

Thomas, S., Fusco, T., Tokovinin, A., Nicolle, M., Michau, V., & Rousset, G. 2006, MNRAS, 371, 323

Tyson, R. 2000, Introduction to Adaptive Optics: Robert K. Tyson, SPIE tutorial texts (SPIE Press)

Tyson, R. K. 2010, Principles of Adaptive Optics, 3rd edn. (University of North Carolina, Charlotte: CRC Press)

Ustione, A., & Piston, D. 2011, Journal of Microscopy, 243, 221

van Dam, M. A., & Lane, R. G. 2000, Journal of the Optical Society of America A, 17, 1319

Véran, J.-P., & Herriot, G. 2000, Journal of the Optical Society of America A, 17, 1430

Verinaud, C. 2004, Optics Communications, 233, 27

Vyas, A., Roopashree, M. B., & Raghavendra Prasad, B. 2009, in International Conference on Advances in Recent Technologies in Communication and Computing, 2009. ARTCom '09, p. 366-369, 366–369

Wallner, E. P. 1983, Journal of the Optical Society of America (1917-1983), 73, 1771

Wang, J. Y., & Markey, J. K. 1978, Journal of the Optical Society of America (1917-1983), 68, 78

Wilson, T. 2011a, Journal of Microscopy, 242, 111

—. 2011b, Journal of Microscopy, 244, 113

Wolverton, B. C., Johnson, A., & Bounds, K. 1989, Interior landscape plants for indoor air pollution abatement, Tech. rep., National Aeronautics and Space Administration

Wright, A. J., Burns, D., Patterson, B. A., Poland, S. P., Valentine, G. J., & Girkin, J. M. 2005, Microscopy Research and Technique, 67, 36

Yusufu, S. N., & Dubra, A. 2014, Biomedical optics express, 5, 30593073

Zhu, D., Larin, K. L., Luo, Q., & Tuchin, V. V. 2013, Laser Photon Review, 5, 732

Appendix A

Appendix: Pinhole size diameter for wavefront sensing

As presented before in this thesis, one method that uses backscattered illumination light along with coherence gating to ensure that light scattered from the focal region is employed to measure sample aberrations, corresponds to coherent-gated wavefront sensing (CGWS). This approach is only possible with low coherence illumination and requires an interferometric arrangement. Alternatively, a pinhole can be used to exclude out-of-focus light, in a similar way to the pinhole used in a confocal microscope. This is the approach followed in this thesis.

In the system built in this work, a confocal pinhole was used in the wavefront sensing path. This pinhole was located at a plane conjugated to the objective focus plane. This pinhole has the additional advantage of smoothing the light field that reaches the Shack-Hartmman wavefront sensor pupil. The size of this pinhole must be carefully chosen to provide a compromise between spatial selectivity and the degree of smoothing. Some papers can be found in the literature addressing the problem of pinhole size selection (Rahman & Booth (2012); Shaw et al. (2013)).

In this case, it is necessary to use a pinhole sufficiently big that allows the passing of an adequate amount of information about the distorted wavefront contained in the spatial frequencies. However, as this pinhole is conjugated to the focal plane, it also has to be sufficiently small to be able to reject out-of-focus light from planes above and below the focal plane.

In the system, there are three components that we might need to consider when selecting the right pinhole. The first component corresponds to the corrector device that we employ. In our case, the membrane deformable mirror, will only be able to correct only a certain range of frequencies, dictated by the separation between its actuators. The second component corresponds to the lenslet array that conform the SHWFS. In a similar way to the corrector, the lenslet array will limit the range of frequencies that we will be able to measure. The range of frequencies in this case is dictated by the diameter of each lenslet. The third and final component that needs to be considered is the lens that is located in front of the pinhole.

Even though the deformable mirror plays an important part in the correction of the aberration, in this case the it is the Shack-Hartmann sensor the component that will define the range of possible wavefront to be measured. There is no reason to try to correct with the mirror those aberrations that the SHWFS cannot measure. Then, the minimum pinhole diameter that can be employed will be given by the lens located before the pinhole and the SHWFS.

It is possible to get two pinhole minimum diameters from these components. The first minimum diameter is given by passing the first minimum of the intensity pattern formed by the lens and the second is related to the frequencies that the SHWFS can measure. In this case, the lenslet array is considered as a sinusoidal grating to carry on with the calculations.

Then, minimum pinhole size, ϕ being its diameter, it is given by

$$\phi_{min} < \sum(\text{grating} + \text{Airy})$$

$$\phi_{min} < (1.22 + N)\,\frac{\lambda f}{d} \tag{A.1}$$

where N is the number of lenslets across the system pupil (N=7.5 in our case), λ is the illumination wavelength (λ=680 nm), f is the focal length of the lens located before the pinhole (f=100 mm) and d is the beam diameter (d=5 mm). From these values, the minimum pinhole size required to pass the first minimum will be

$$\phi_{min} < \left(1.22 + \frac{7.5}{2}\right)\frac{680 \times 10^{-9} 100 \times 10^{-3}\text{m}}{5 \times 10^{-3}\text{m}} \tag{A.2}$$

$$\boxed{\phi_{min} \sim 51\mu m}$$

The second minimum pinhole diameter size is related to the SHWFS range that can be measured. To be able to measure the whole frequency content and in order to have a reasonable sampling, by Nyquist theorem and expression (A.1), then

$$\phi_{info} \geq 2\phi_{min}$$

$$\phi_{info} = \left(2.44 + 7.5\right)\frac{680 \times 10^{-9} 100 \times 10^{-3}\text{m}}{5 \times 10^{-3}\text{m}} \tag{A.3}$$

$$\boxed{\phi_{info} \sim 135\mu m}$$

As we work with aberrated wavefronts, the minimum pinhole size diameter required is 135 µm, in order to be able all the information that a wavefront can carried. However, as these calculation does not consider the aberration strength it is necessary to use a pinhole slightly bigger. The first commercially available pinhole is 150µm. This was the selected diameter that we utilised in our system. The use of a smaller pinhole diameter will lead to rejection of part of the wavefront, lossing information that will affect the system's performance. A bigger pinhole size will allow all the information to be measured. However, out-of-focus light will reach the detector affecting the centroid calculations.